Thermo - Plasmonics:
Controlling and probing temperature on the nanometer scale

Jon S. Donner

March 10, 2014

Contents

Introduction

Nano-optics

When I started my thesis in 2009 the Nobel Prize in Physics was awarded for technological breakthroughs in the field of optics. Charles Kuen Kao received the award "*for groundbreaking achievements concerning the transmission of light in fibers for optical communication*", and Willard Sterling Boyle and George Elwood Smith were awarded for "*the invention of an imaging semiconductor circuit – the CCD sensor*". These applications and optics in general have profoundly impacted modern society. *Nano-optics*, which studies the behavior of light on the nanoscale, holds promise to do the same. Only recently has the experimental exploration of nano-optics been enabled thanks to the maturation of various technologies including lasers, nano fabrication, electron beam microscopy, near field optical microscopy and colloidal chemistry amongst others. By taking advantage of these technologies, nano-optics has provided a plethora of novel photonic structures including: quantum dots used as nano sources of light [1], nano diamonds which permit mapping of local magnetic fields and density of states [2], extremely high Q-factor resonators which can serve as ultra sensitive detectors [3], surface plasmon waveguides which could allow for ultra compact planar optical circuitry [4], nano antennas which are used to harvest and radiate light efficiently [5], gold nano particles which could allow for novel cancer treatment techniques [6], and many more.

When using traditional optical elements such as mirrors and lenses to control light propagation, there is a fundamental limit on the localization of the field set by the Abbe diffraction limit of about half the wavelength, which could *a priori* impinge on the ability to use optics on the nanometer scale. One way to confine electromagnetic waves to dimensions that are smaller than the free space vacuum wavelength is to couple light with materials that have high dielectric permittivity. Among these materials a particular interest has been devoted to

metallic nanostructures. In this case the coupling of the Electromagnetic (EM) wave and the conduction electrons of the metal results in a charge oscillation on the surface of the metal. For a specific wavelength and polarization the interaction is resonant and can lead to a collective coherent electron oscillation known as a *Surface Plasmon* (SP). The latter enables to strongly confine and enhance the electric field at the surface of the metal on a scale much shorter than the incoming wavelength [7, 8]. In the far field, such enhanced interaction results in both strong absorption and scattering of light [5, 9].

The frequency of the plasmon resonance can be readily altered by changing the particle size, shape or environment [10]. Significant advances in nanoparticle synthesis allow the fabrication of nano particles with a wide variety of shapes and sizes (spheres, triangles, prisms rods cubes and more [10]). For gold, the resonances occur at frequencies ranging from the visible to the infrared, depending on the size and shape of the nanoparticles [11, 12, 13]. For instance, spherical gold nanoparticles feature a resonance in the green region of the spectrum, while asymmetric gold nanoparticles like Nanorods (NRs) have a more complex dual peak spectra, with the prominent resonance in the near-infrared range. To assist the design of these nano structures, strategies can be based on well established antenna theory developed for the radio and microwave regions. This is not straight forward as metals are not perfect conductors at optical frequencies. To overcome this, a wavelength scaling law for applying antenna designs to optical frequencies was proposed by Novotny [14]. An example of scaling down of a classical antenna to the nanoscale was presented by Curto et al. [15], to achieve directed optical emission using a nanoscale Yagi Uda antenna.

An inherent effect in such systems is the unavoidable damping of the SP. This originates from internal Joule dissipation and results in heat generation. Before 2006 [16, 17], this heating effect was generally considered to be a parasitic nuisance [18] that should be minimized. During the next few years, and just before my PhD began, first experiments and simulations started to show the potential of generating heat at the nanoscale with SPs. Consequently, metal nanoparticles can be used not only as *nano-sources of light* but also as *nano-sources of heat*. Today, the latter approach offers many opportunities in both physical and biological applications [19, 20]. Controlling and exploiting plasmonic heating is the topic of my PhD.

Thesis outline

The work in this thesis is organized as follows:

- **Plasmonic heating: fundamentals and experimental tools**
  Chapter 1 deals with the physics of plasmonic heating. First the energy conversion from light to heat is explained. Subsequently, the heat transfer from the nano particles to the surrounding is discussed. Finally, we adopt an experimental approach and explain the main parameters that allow to tune the heating efficiency of plasmonic structures. In chapter 2 we present some techniques that enable to measure temperature at the nanoscale. Then the method used in this thesis, relying on fluorescent polarization anisotropy, is detailed. Finally, the main optical setup and software tools are shown.

- **Physical applications**
  In chapter 3 we demonstrate a fast tunable thermal lens based on plasmonic heating. First, we develop a model to predict the lens behavior. Next, experimental characterization of a fabricated thermal lens is performed. Finally, we show that such a system could be used for fast and accurate focal plane tunability as well as for adaptive optics applications. Chapter 4 deals with plasmonic heating in the context of microfluidic systems. We numerically demonstrate the fluid convection that is induced by plasmonic heating at the micro and nanoscale. We proceed to describe the fabrication and testing of a microfluidic pump based on plasmonic heating.

- **Thermal imaging in biology**
  In chapter 5 we present the use of Green Fluorescent Protein (GFP) as a thermal nanoprobe suited for *in vitro* cellular temperature mapping. We apply this method to monitor the temperature generated by photothermal heating of gold nanorods inside and outside of cells. In chapter 6 we extend the thermal imaging technique and perform *in vivo* intracellular thermal imaging which is demonstrated on GFP expressing neurons of a worm.

1

Basics of plasmonic heating

In this chapter we present the basic processes related to plasmonic heating. These physical phenomena are at the base of a subfield of plasmonics, named *thermo plasmonics*, which uses metal nanoparticles (NPs) as efficient nano-sources of heat remotely controllable by light. This provides an unprecedented way to control thermal-induced phenomena at the nanoscale [16]. We first motivate this field of research by presenting various applications. We then address the physics involved in plasmonic heating. Finally we adopt a practical approach and use a basic experiment to explore parameters that enable tuning of plasmonic heating efficiency.

1.1 Motivation

Heat is involved in many physical, chemical and biological mechanisms. As such, a myriad of applications has been proposed within the rapidly growing field of thermo plasmonics [19]. Some of these applications include thermal lithography [21], plasmon assisted chemical vapor deposition [22], optofluidics [23], photothermal imaging [24] and photoacoustic imaging [25]. A particular interest has been devoted to bio-applications. For example, one approach in hyperthermia cancer therapy is to specifically bind optical absorbing agents to cancerous tissues by means of selective chemistry [26]. Consequently, by applying a suitable illumination, only these tissues are damaged [26]. Gold Nano Particles (GNPs) are good candidates for this application as gold is considered to be non toxic [27][1]. Furthermore, the plasmon resonance peak of GNPs can

[1] The toxicity of GNPs is still somewhat of an ongoing researched matter.

be tuned to the biological tissue transparency window [6, 28], which is in the rage of 650-900 nm (mainly nanorods or nano cages are used). Another example of a biomedical application in thermo-plasmonics is targeted drug delivery for therapeutic purposes. The therapeutic agents are attached to gold NPs that act as nano-carriers through the human body. The active agents can be released at the desired location by remotely heating the NPs using laser illumination. Although the applications presented above are very different, the underlying physical mechanisms responsible for the plasmonic heating are similar and will be detailed in the following section.

1.2 Physics of plasmonic heating

A surface plasmon can be defined as a collective oscillation of the free electron gas in a metal [29, 30]. As metals are not ideal conductors at optical frequencies, there is a damping of this oscillation via different mechanisms (such as electron-phonon collisions [31]). The damping exerted on the free electron gas oscillating inside the particle results in heat generation by a Joule mechanism [32]. This heat generation increases the temperature inside the object and places the system out of equilibrium. The temperature of the environment is thus increased to reach a new equilibrium. To explore this process we consider a metal nanoparticle illuminated by a monochromatic light at the angular frequency $\omega = k_0\, c$. In the following, we specifically consider the case where the nanoparticle is surrounded by water (a common experimental case)[2]. Let $\mathbf{E}(\mathbf{r},t) = \mathrm{Re}\left\{\mathbf{E}(\mathbf{r})e^{-i\omega t}\right\}$ be the electric field and $\mathbf{E}(\mathbf{r})$ its complex amplitude. Let $\mathbf{j}(\mathbf{r})$ be the complex amplitude of the electronic current density inside the particle. The heat source density $\bar{q}(\mathbf{r}) \equiv < q(\mathbf{r},t) >_t$ inside the nanoparticle, arising from Joule effect, reads [32]

$$\begin{aligned} \bar{q}(\mathbf{r}) &= < \mathbf{j}(\mathbf{r},t)\cdot\mathbf{E}(\mathbf{r},t) >_t \\ \bar{q}(\mathbf{r}) &= \frac{1}{2}\mathrm{Re}[\,\mathbf{j}(\mathbf{r})^\star\cdot\mathbf{E}(\mathbf{r})] \end{aligned} \tag{1.1}$$

Using the relations $\mathbf{j}(\mathbf{r}) = -i\omega\mathbf{P}(\mathbf{r})$ and $\mathbf{P}(\mathbf{r}) = (\varepsilon_\mathrm{m} - \varepsilon_0)\,\mathbf{E}(\mathbf{r})$, equation (1.1) can be recast into:

$$\bar{q}(\mathbf{r}) = \frac{\omega}{2}\,\mathrm{Im}(\varepsilon_\mathrm{m})\,|\mathbf{E}(\mathbf{r})|^2 \tag{1.2}$$

[2]In the case that the GNP is on a glass substrate the physical orders of magnitude of the problem should not change significantly as the optical properties and thermal conductivities of glass and water are comparable.

where ε_{m} is the metal permittivity.

The heat source density $\bar{q}(\mathbf{r})$ is thus proportional to the square of the electric field inside the nanoparticle. Its distribution strongly depends on the nanoparticle size and shape and can be highly contrasted throughout the structure [11, 32].

The total heat power delivered by the metal nanoparticle is given by integrating over the heat source density[3].

$$Q \;=\; \frac{\omega}{2}\,\mathrm{Im}(\varepsilon_{\mathrm{m}}) \int_V |\mathbf{E}(\mathbf{r})|^2 d\mathbf{r} \tag{1.3}$$

where V represents the volume of the nanostructure. Many numerical simulation approaches rely on this formula to compute the heat generated by a plasmonic nanoparticle. Alternatively, the heat can be expressed as a function of the optical absorption cross section σ_{abs} of the nanoparticle

$$Q \;=\; \sigma_{\mathrm{abs}}\, I \tag{1.4}$$

where $I \;=\; n\, c\, \epsilon_0 \mathbf{E}_0^2/2$ is the irradiance of the incoming plane wave. This approach enables simple calculation when the σ_{abs} is analytical, which is the case for a sphere or an ellipsoid amongst others.

1.3 Thermodynamics at the nanoscale

Once the heating sources originating from the Joule effect are determined, we can introduce them into the general equations that govern heat diffusion in the surrounding environment. This two step analysis for temperature increase is justified because heat generation inside the NP is much faster (ps) [34] than its release into the environment (ns-µs) [35]. As such, the differential equation governing heat diffusion reads

$$\rho(\mathbf{r})\, c_{\mathrm{p}}(\mathbf{r})\, \partial_t T(\mathbf{r},t) \;-\; \nabla \cdot (\kappa(\mathbf{r}) \nabla T(\mathbf{r},t)) \;=\; q(\mathbf{r},t) \tag{1.5}$$

where κ is the thermal conductivity, ρ the density, c_{p} the heat capacity at constant pressure of the fluid and T the temperature.

Let us first address the implications of working at the nanoscale. The hydrodynamic equations remain valid as far as the mean free path of the particles

[3]To get equation 1.3 we assume that ε_{m} does not depend on $\mathbf{r}$, which is generally true for structures used in this work (dimensions of the structures typically larger than 10 nm) [33]

constituting the fluid medium is smaller than any characteristic length of the system, allowing to consider the medium to be continuous. At the nanoscale, such an approach is still valid when considering a liquid but may be incorrect for a gas. In general, temperature is defined as an average kinetic energy of entities and is always defined regardless of the size of the system. However when the system is composed of a small number of entities, the equations of thermodynamics are not well defined[4] because the temperature T will undergo large fluctuations. In other words, the question is not related to the existence of temperature, but to its usability. Within the context of this work, the systems of interest consist of a liquid surrounding sources of heat larger than tens of nm. This length scale is much bigger than the molecular mean free path of the fluid and therefore ensures that temperature is continuous and the hydrodynamic equations valid and well defined.

After this discussion of hydrodynamics at the nanoscale we continue and further analyze the heat diffusion equation. To do so, we consider that the thermal conductivity is constant within the medium. In this case equation 1.5 reads [36]

$$\rho\, c_{\mathrm{p}}\, \partial_t T(\mathbf{r},t) \;-\; \kappa\, \nabla^2 T(\mathbf{r},t) \;=\; q(\mathbf{r},t) \tag{1.6}$$

From this equation, the characteristic time scale expected relevant for nanoscale dimensions can be extracted. To do so, we consider the volume outside the particle where the heat sources are equal to zero ($q = 0$). In this case the previous equation reads

$$\partial_t T(\mathbf{r},t) \;-\; \alpha\, \nabla^2 T(\mathbf{r},t) \;= 0 \tag{1.7}$$

where $\alpha = \kappa/\rho\, c_{\mathrm{p}}$ is called the thermal diffusivity. For water, it equals 0.14 mm^2/s. From a dimensional analysis of this equation, we deduce that, if the length scale of the system is $\tilde{L}$, the time scale related to thermal processes $\tilde{t}_T$ will be

$$\tilde{t}_T = \tilde{L}^2/\alpha \tag{1.8}$$

Note that this time scale does not depend on any temperature or boundary conditions. To give some examples, in water, for $\tilde{L} = 100$ nm and 1 µm, we respectively obtain $\tilde{t} = 70$ ns and 7 µs. Thus, 10 ns – 10 µs is the range of

[4] Fluctuations are on the order of : $\sigma(\frac{1}{\sqrt{N}})$, N being the number of particles

characteristic time scales of thermal processes that occur the nanoscale, independently of the temperature increase[5].

After analyzing the typical time scale required to establish the temperature, we consider a steady state regime and qualitatively analyze the temperature spatial profile. In the steady state regime the heat diffusion equation becomes the Poisson equation

$$\kappa \nabla^2 T(\mathbf{r}) = -\bar{q}(\mathbf{r}) \tag{1.9}$$

The profile of the heat generation density $\bar{q}(\mathbf{r})$ can be highly non-uniform inside a plasmonic structure. However its internal temperature profile remains quasi-uniform due to the much higher thermal conductivity of metals compared with the surrounding media (air, water, glass, ...) [36].
Since the source of heat in the system is restricted to the plasmonic structure, the equation governing heat diffusion in the surroundings becomes a Laplace equation

$$\nabla^2 T(\mathbf{r}) = 0 \tag{1.10}$$

Solving this equation dictates that outside the structure, the temperature features a $1/r$ decrease [36]. Interestingly, equation (1.10) does not present any length related constant, like the wavelength in Maxwell's equations for instance. The direct consequence is that the *relative* temperature profile does not depend on the size of the structure: around a plasmonic nanoparticle of typical dimension $\tilde{L}$, the temperature expands over approximatively $\tilde{L}$, whatever the nanoparticle temperature increase[6]. This is illustrated in Figure 1.1 where we show that the visual temperature extension around a particle remains the same whatever the length scale, the temperature increase or the thermal conductivity of the medium.

Although the temperature profile is fixed, the absolute temperature increase can be controlled. To this end different parameters have to be considered [36]: i) the absorption cross section of the nanoparticle, ii) its morphology – the heat dissipation is be favored in elongated or small particles since the surface to volume ratio is increased, this leads to lower temperature –, iii) the environment

[5]The time scale doesn't depend on the final temperature in the first approximation. However, correction terms due to dependence of the thermal diffusivity on temperature could exist.

[6]Assuming we are in the linear diffusive regime. Also assuming CW illumination. In the case of pulsed illumination other behavior has been evidenced [37].

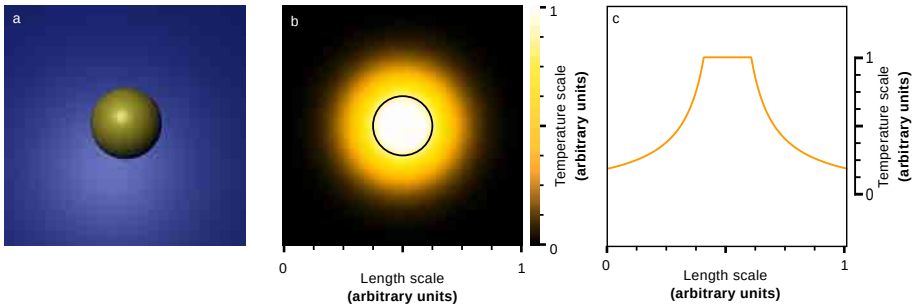

Figure 1.1: *Temperature profile around a metallic sphere. a) Image of a considered nanoparticle. b) Temperature distribution in a plane. c) A 1D temperature crosscut of b). Arbitrary units have been used on purpose to show that this profile remains valid whatever the temperature scale and the length scale considered. The thermal conductivity of the surrounding medium does not influence this relative temperature* ***profile*** *neither (although it does change the absolute temperature raise as seen in equation 1.11).*

– the higher its thermal conductivity, the lower the temperature – and iv) the laser power. For a spherical particle, the computation of the nanoparticle temperature increase ΔT_0 is straightforward and yields a useful analytical formula [36]

$$\Delta T_0 = \frac{\sigma_{\text{abs}} I}{4\pi \kappa R} \tag{1.11}$$

where I is the irradiance of the incoming light and R the radius of the sphere. As an example, to obtain a temperature increase of 1°C in a $R = 25$ nm spherical nanoparticle in water illuminated at the plasmonic resonance (530 nm), the required laser power is 3.8×10^3 W/cm^2, *i.e.* 3.8×10^{-2} mW/µm^2. For the more general case where the nanoparticle is not spherical, a correction factor to formula 1.11 exists [36]. Moreover, when numerous illuminated plasmonic particles are in close proximity, some cooperative thermal effects can occur and increase the expected average [38, 39].

1.4 Parameters of plasmonic heating

After describing the physics of plasmonic heating, we present the main parameters that can be used to practically control plasmonic heat generation. To illustrate the importance of both the experimental conditions, such as laser intensity or particle concentration, as well as the morphology of the plasmonic photothermal agents, we have performed experiments on a simple but general configuration consisting of colloidal Gold Nanorods (GNR) immersed in water. GNRs are particularly interesting to study due to their optimal photothermal efficiency conversion rates [40]. In the following, I describe this study, and independently analyse the role of the experimental conditions and the morphology of the considered heating objects. Once the parameters that govern plasmonic heating are known, they can be chosen to tune the heating efficiency, depending on the relevant plasmonic application.

Synthesis and optical characterization of colloidal GNRs

During the last twenty years, a wealth of literature has shown the possibility to tune the position of the Surface Plasmon Resonance (SPR) of nanostructured plasmonic materials [41, 42, 43, 44]. In particular, the role of the morphology (shape, size and aspect ratio for instance) and environment [29, 45] were thoroughly investigated. In this work, different colloidal gold nano-antennas have been chemically synthesized using the seed mediated procedure described elsewhere[7] [46]. Table 1.1 summarizes the dimensions of the GNRs together with the position of their SPR obtained with extinction measurements.

Figure 1.2 presents the SEM images and the corresponding extinction spectra recorded on the samples 1 to 4 (table 1.1). In this case, the location of the SPR strongly varies from the visible to the Near Infrared (NIR) range when changing the aspect ratio of the objects. For instance, an aspect ratio of 2.867 and 5.483 leads to resonances of 742 nm (visible) and 950 nm (NIR), respectively.

Time response and steady state temperature

After characterizing the SPR, we proceed to investigate the temperature of an illuminated GNR solution as a function of the experimental conditions. Figure 1.3b shows the time evolution of the temperature inside a homogeneous solution (solution 5 of table 1.1) illuminated with a 800 nm laser beam. This

[7]Synthesis of GNRs used in this section was performed by Dr. Ignacio de Miguel Clave, a research engineer in the PNO group.

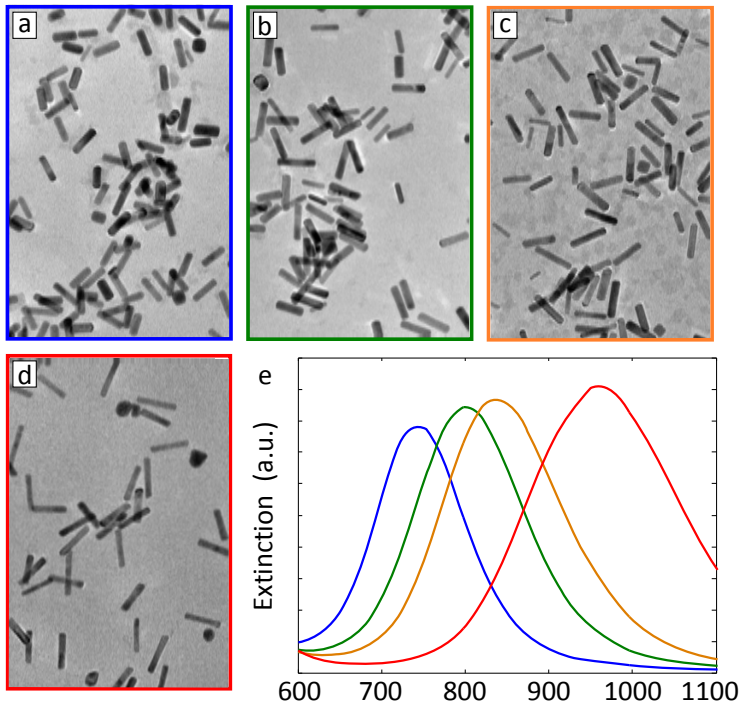

Figure 1.2: *Tuning the surface plasmon resonance of colloidal gold nano-rods by varying their aspect ratio (sample 1 to 4, table 1.1). Scanning electron microscopy images of different gold nanorods and their associated extinction spectra measured on 0.3 mL water solutions having a concentration of GNRs of 0.58 nM.*

Sample	D (nm)	L (nm)	A.R.	SPR (nm)
1	12.2	34.5	2.86	742
2	12.0	44.1	3.73	801
3	12.0	51.1	4.27	845
4	12.1	66.3	5.48	945
5	18.8	57.3	3.33	789
6	9.7	34.6	3.71	805
7	10.7	40.0	3.75	809
8	14.4	49.6	3.63	795

Table 1.1: *Synthesis of different gold nanorods used in this study. The average size (diameter D and length L) and shape (Aspect Ratio (A.R.)) of the objects were systematically measured on a hundred nanorods for each solution using Scanning Electron Microscope (SEM) images (see examples in Figure 1.2). The peak position of the surface plasmon resonance measured for each solution of nanorods dispersed in water has been extracted from extinction measurements using a commercial Perkin Elmer spectrometer (Lambda 950 UV/Vis).*

experiment has been performed on the same solution upon different illumination powers. Whatever the considered irradiance (for powers up to 340 mW, delivered in a collimated beam with a radius of about r=2mm), we find a characteristic time τ to reach the equilibrium temperature of slightly less than three minutes. This is consistent with the previous theoretical analysis that this time mainly depends on the size of the heating and the thermal diffusivity of the environment (equation 1.8). In our case, the thermal diffusivity of water is $\kappa = 1.43 \cdot 10^{-7}\,\mathrm{m^2 s^{-1}}$ which leads to a characteristic size of the heating system: $R = (\tau\kappa)^{1/2} = 5$ mm which is close to the size of the cuvette used during the experiment.

Moreover, the steady state temperature value varies when changing the power of the incoming laser beam. Figure 1.3c shows an expected linear growth of the temperature when increasing the heating laser power. This relationship is not absolute and depends on the experimental conditions. For instance, Figure 1.3d shows that the temperature growth for the same illumination condition increases with the concentration of the solution according to a Beer-Lambert law.

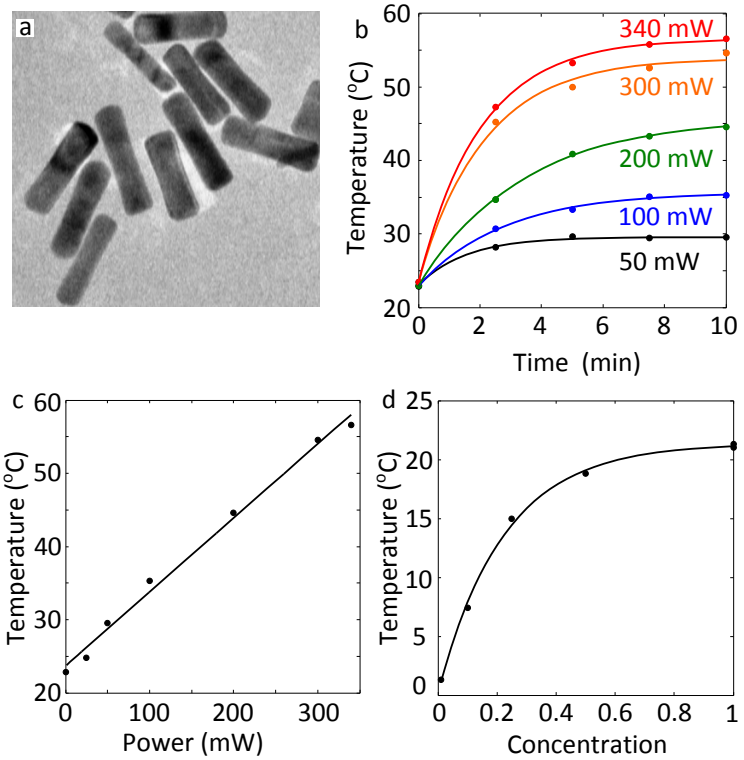

Figure 1.3: *Temperature increase induced by optical heating of gold nanorods in dependence of time, incoming laser irradiance and concentration of the solution. a) SEM image of GNRs from sample 5 in table 1.1. b) Time dependence of the temperature increase of a 0.3 mL solution having a 0.58 nM GNR concentration for different laser powers. The temperature is measured using a Peltier probe (agilent u1241A + agilent thermocouple). An increase of the temperature is observed for the different irradiance powers before reaching saturation. The characteristic time to get to the steady state temperature is close to 3 min for the different powers. c) Evolution of the temperature of the solution as a function of the heating laser power. The temperature was measured after 10 min in each case in order to reach the saturation shown in b). d) Impact of the GNR concentration on the temperature increase. When increasing the concentration of GNRs in the solution of 0.3 mL, we observe an increase of the steady state temperature at small concentrations, before reaching saturation.*

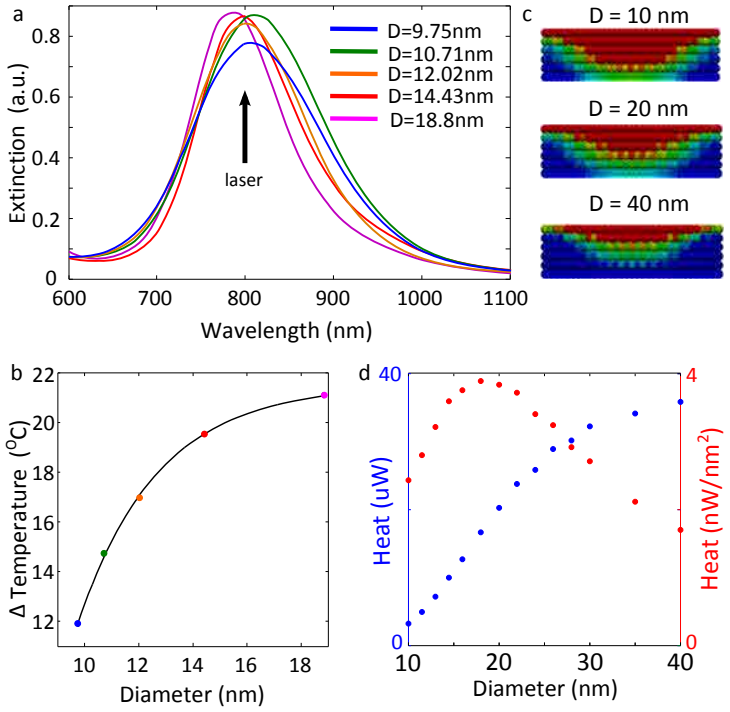

Figure 1.4: *a) Spectra of GNRs with different width, but all having similar SPR at 800 nm. b) Evolution of the temperature growth as a function of the diameter of the objects (sample 2 and 5 to 8, table 1.1) having the same concentration of GNRs and illuminated with the same power (P= 200 mW at 800 nm). The aspect ratio of the GNRs was fixed to 3.7 in order to excite the different objects at their SPR with the same laser. c) Map of the electric field intensity in a cross-cut of the GNRs using the same color scale. d) Heat produced by different GNRs excited at their SPR λ = 800 nm in dependence of the diameter of the considered GNR.*

From heat efficiency to temperature: impact of morphology

In the following, we discuss the conditions required to improve the heat efficiency of our system and thus maximize the steady state temperature for a given concentration of nanorods and a fixed incoming laser power. This point

is crucial for many applications. For example in photothermal therapy it may allow to decrease or even avoid tissue damages due to light absorption [47].

Generally, when searching for the best nano heat source one is faced with a paradox. On the one hand we want a good metal that can absorb and store a lot of optical energy (hence a high quality factor resonance), on the other hand we want a system that efficiently converts this energy into heat via internal loses which would mean a damped system (*i.e.* a low quality factor resonance).

From a mathematical point of view, this duality is portrayed in the heating equation (as derived in equation 1.3 and presented here for convenience)

$$Q = \frac{\omega}{2} \operatorname{Im}(\varepsilon_{\mathrm{m}}) \int_V |\mathbf{E}(\mathbf{r})|^2 d\mathbf{r}$$

where $\operatorname{Im}(\varepsilon_{\mathrm{m}})$ is the imaginary part of the dielectric permittivity of the gold particle of volume V at the considered optical frequency ω and $\mathbf{E}$ is the electric field inside the object at the position $\mathbf{r}$. Increased heating would dictate two contradicting requirements. On the one hand the electric field $\mathbf{E}$ should penetrate into all the volume of the NP, which would happen in a non perfect metal[8]. On the other hand the electric field $\mathbf{E}$ should be enhanced by a good charge oscillation, a condition met in a perfect metal.

As an illustration of this discussion, we have performed measurements on five nano-rod batches with different diameters all having a surface plasmon resonance centered at the same frequency (around 800 nm), as shown in Figure 1.4a. This is achieved by having a similar aspect ratio close to 3.7 (sample 2 and 5 to 8, table 1.1). The steady state temperature increments measured on these different samples are reported in Figure 1.4b as a function of the diameter D of the GNRs. For a diameter of about 14 nm or below, the temperature increases strongly when increasing the size of the GNRs whereas a small growth is observed for values of 14 nm up to 19 nm. This behavior can be qualitatively understood as a combination of two factors. First, the surface plasmon mode is well defined for GNRs above a certain diameter. This has been previously explained in works about mode cut-off or leaking modes in guided optics [48, 18]. Experimentally, this point is evidenced by looking at the extinction spectra (Figure 1.4a). As the SPRs are centered at the same wavelength (800 nm), the Full Width Half Maximum (FWHM) is inversely proportional to the quality factor. We observed that the FWHM decreases with diameter and so

[8]In the case of gold, the skin depth δ is close to 20 nm at optical frequencies. Thus, the heat generation is produced by a 20 nm thick layer lying below the illuminated face of the object.

the Q factor increases. Second, the only part of the electric field that produces heat is the field located inside the object. When increasing the GNR diameter above the skin depth, the field does not penetrate inside the central part of the GNR and so this part does not contribute to the heating. This explains the slower increase of the temperature measured for the highest diameter in Figure 1.4b.

To support this analysis, numerical simulations using the Green dyadic technique [30] have been performed on a single GNR immersed in a water environment with increasing diameters (fixed aspect ratio AR=3.7)[9]. Figure 1.4c presents a cross-cut of the electric field intensity inside GNRs excited at their SPR ($\lambda = 800$ nm). The maximum value of the intensity was saturated in order to highlight that the intensity cannot penetrate inside the whole object when the diameter is larger than typically 20 nm (skin depth). Next, we calculated the heat generated inside each GNR (blue curve, Figure 1.4d). First, a strong increase is observed for small diameters. This corresponds to the fact that any increase in diameter helps to better define the mode and so increases the total field and heat production in the particle. At larger diameters, the mode is already well defined. The heat production continues to rise (at a slower pace) and is simply attributed heating of a larger volume. To analyze the temperature measurement (as in Figure 1.4b), we must look at the heat generation per unit of surface. The reason is that the temperature growth of the environment originates from the energy transfer which has to pass through the surface of the particles. When considering GNRs that have an SPR at 800 nm, it appears that the best objects to increase the temperature of the environment have a diameter close to 18 nm.

Depending on the targeted application, the highest efficiency may not necessarily be the best choice as other considerations may take precedence. For instance, *in vivo* bio-applications may require small NPs since they better diffuse in the tissue to reach the targeted area and so their concentration will be higher which in turn may render the heating process more efficient. In this case, there is a trade-off between optimizing particle concentration and individual particle heating efficiency. For example, a 13 nm diameter NP might be a good compromise since it only requires to increase the power by 15% to get the same temperature as in the case of a 20 nm diameter GNR and has better diffusive properties.

[9]Simulations were performed by Dr. Renaud Marty, a post doc in the PNO group.

Effect of wavelength

After optimizing the diameter, we can still tune the position of the SPR by varying the length of the GNRs. First, we measured the temperature increment on the same solution illuminated with the same power (P=200 mW) but at different wavelengths (Figure 1.5a). For this experiment, we used solution 1 (see table 1.1) that presents an SPR at 742 nm (blue spectrum in Figure 1.2e). Figure 1.5a unambiguously shows that the largest temperature growth is observed when exciting the objects at their SPR and much less heating is obtained when the laser is out of resonance.

Subsequently, we excited different solutions of GNRs (samples 1 to 3, table 1.1) with the same power, each at their respective SPR (Figure 1.5b). We probed the conversion efficiency from 740 nm up to 850 nm but we did not observe a strong modification of the heating. As the conversion efficiency is given by the imaginary part of the dielectric permittivity (see heat source equation 1.2), its efficiency depends only weakly on the wavelength since the imaginary part of gold dielectric permittivity almost does not depend on the illumination wavelength in the considered frequency range (red curve in Figure 1.5c). Thus, to optically heat gold the choice of wavelength in the NIR domain (from 600 nm up to 1000 nm) is not extremely important as long as the illumination wavelength matches the SPR. Nevertheless, even if the heat conversion efficiency is relatively constant, the choice of the wavelength is still intricate and is guided by the specific application and optical properties of the environment.

Summary

To study the influence of experimental conditions and morphology of plasmonic heating we synthesized GNRs with different geometrical and optical properties. We evidenced a linear dependence between the temperature raise and the incoming laser power. We then showed that the temperature depends on the GNR concentration according to a Beer-Lambert law. We went on to present an example of the characteristic heating time and showed how it depends on the size of the heating volume and not on the absolute temperature raise. By measuring temperature as a function of GNR diameter we saw that for efficient heating the GNR needs to be above a certain diameter, which allows the surface plasmon mode to be well defined. We finally studied the influence of illumination wavelength and concluded that in the case of gold nano particles, as long as the heating is resonant the efficiency does not depend on the wavelength. In

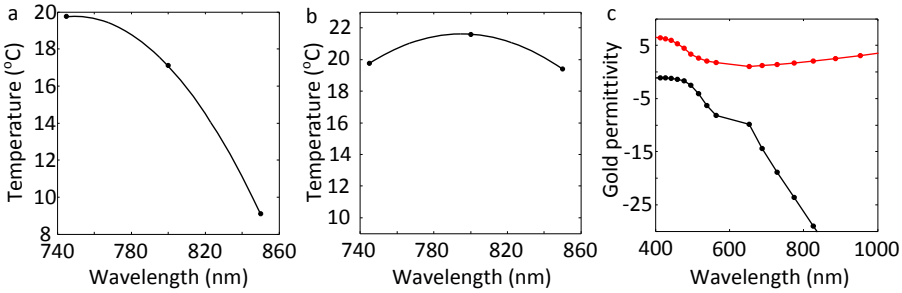

Figure 1.5: *a) Evolution of the temperature increase of GNRs (solution 1, table 1.1) excited at different wavelengths with the same power set to 200 mW. We observe a strong decrease of the temperature growth when the GNRs are excited out of resonance (see spectrum in Figure 1.2, blue curve). b) Temperature increase in dependence of excitation wavelength for resonant GNRs with a diameter fixed at 12 nm (solution 1 to 3, table 1.1 and Figure 1.2). In the considered regions of wavelength in the near IR, we observe a weak dependence of the temperature increment whatever the resonance of the GNRs. C) Dispersion of the imaginary part of the dielectric permittivity of gold (red) explaining the weak difference observed in b). Real part of the permittivity in black (taken from reference [49]).*

conclusion, plasmonic heating strongly depends on the parameters of the heated object (size, shape, material) and experimental conditions (concentration, laser power, environment). In any application the combination of these must be considered because there is often a trade-off between the two and the optimization of one might affect the other.

2

Experimental methods

In the previous chapter a macro scale thermometer was used to measure the temperature of a large ensemble of nano heaters suspended in a solution. However, in some cases a macro-scale average temperature may mask important information. Indeed, temperature of a singe nano- or micro-scale structure is sometimes needed. In this context, we first present a short overview of *nanothermometry* methods, followed by the description of a thermal microscopy tool developed in our lab and used during the thesis.

2.1 Nanothermometry

Motivation

Advances in micro and nanotechnology applications call for the ability to perform thermometry with high spatial resolution. For this reason much effort has been invested in nanothermometry as reported in various recent review articles [19, 50, 51, 52]. Indeed many different fields would benefit from accurate and precise temperature measurements. In electronics one factor that limits high performance microprocessors is local raise of temperature [53]. The size of these hotspots can be sub-micronic as the most common constituent, the transistor, is currently as small as 22 nm (Intel "*22nm technology*"). The ability to map temperature with nanometer resolution could help to investigate this phenomena and then improve microprocessor deign and performance. In the field of integrated photonic devices, temperature can be used to change the refractive index of wave guides, resulting in extremely fast and miniaturized optical switches [54]. In biology, temperature governs many vital cellular processes

such as metabolism, division and gene expression [55, 56, 57]. Proteins are often involved in these processes and are typically of nm dimensions. Accurate high resolution monitoring of temperature could help to understand cellular behavior, and also to optimize externally induced procedures. Examples of such procedures include hyperthermia therapy [58], photothermal therapy [59, 60], thermo selective drug delivery [61, 62, 63], thermal induced gene expression [55, 64].

The examples above have very different requirements concerning the thermal sensor. For example, in biological applications the issue of toxicity is critical, whereas in the field of micro electronics, this criteria is irrelevant. The field defines the desired characteristics of the thermal probe such as: temperature range, sensitivity, stability, etc. Among the multitude of proposed nanothermometry methods I will mention a few relevant examples. To this end we divide thermal probes into three main families consisting of electrical, mechanical and optical based probes. This partition is extracted from the more complete picture described by Jaque and Vetrone [50].

Electrical thermal probes

The principles that govern electrical based probes are similar to a large scale thermocouple, where an electrical property (voltage, current, resistance, capacitance...) changes with the temperature. A recent example was reported by W. Lee et al. [65], where they fabricated a probe with a nanoscale thermocouple which is integrated on a scanning tunneling probe. With this approach they were able to investigate the heat dissipated in single molecule junctions. In a different work a sub-micrometric thermocouple was inserted into a live cell achieving temperature resolutions of up to 0.1 °C [66].

Mechanical thermal probes

Another class of thermal probes rely on the change of mechanical properties due to temperature. One early work in this field was done by Nakabeppu et al. [67] where they used an Atomic Force Microscope (AFM) to scan a cantilever probe made of a bi-material probe. Any change in the surrounding temperature causes the cantilever to bend due to the differential thermal expansion of the two probe materials. In this fashion they were able to achieve a temperature resolution of 0.14°C. Another example is given by Gao et al. [68], who built a nano scale equivalent of a conventional mercury thermometer. In this case,

liquid gallium expands inside carbon nanotubes, and its height depends linearly on the temperature in the range between 50-500 °C.

Optical thermal probes

Optical thermal microscopy is based on the change of optical properties of materials due to temperature. Thanks to the noninvasive nature of light these probes hold much promise and therefore are extensively researched, resulting in many different proposed probes. Also, these techniques benefit from the ability to combine them with well developed and ubiquitous optical microscopy. For example, combining an optical probe with confocal microscopy would allow for 3D thermal imaging (which is usually not possible with an electrical or mechanical probe).

Raman spectroscopy can be used for thermal imaging as different spectral characteristics depend on temperature. An example was presented by Ioffe et al. [69] where Raman thermometry was implemented for measuring the absolute temperature, using the anti-Stokes/Stokes ratio measured in molecular junctions. The ratio of these intensities is related to the availability of phonon states which is governed by the Boltsman distribution and is a function of temperature [69].

Another approach was recently presented by Baffou et al. [70, 71] where both the temperature and also the heat power density are obtained by measuring the thermal-induced refractive index variation of the medium surrounding the heat source. This technique requires no thermal probe and can be implemented by adding a grating to any normal CCD. It was applied to obtain 3D thermal imaging above a micro heated wire [72], as well as measuring temperature of plasmonic arrays [73].

An alternative method is called thermoreflectance, where there is a change in reflectance of a surface due to its temperature. In a recent publication by Renger et al. [74] this method was used to quantify the phonon contribution to thermal conductivity in crystalline and amorphous silicon.

A recent and interesting approach comes from the photoacoustic field where optical induced signals are acoustically monitored. In two recent publications [75, 76] photoacoustic thermometry was applied to living cells.

An entire class of optical thermal microscopy is fluorescence thermometry. Different fluorescent properties that can be measured for thermometry include: intensity, lifetime, spectral shift, spectral bandwidth, band shape, polarization and more. In this broad subclass, we address a few relevant examples and classify them according to the fluorescent thermal probe. Quantum dots (QD) have

been extensively used due to advantages such as: high quantum yield, tunable spectral range. QDs have been used to locally measure temperature of nano devices [77, 78] and also for measuring intracellular temperature [79, 80] using both one and two photon fluorescence with accuracies of about 1°C. The QDs fluorescence dependence on temperature stems from confinement induced changes of phonon coupling [81]. Interestingly, both intensity and spectral shift of the QDs have been used to monitor temperature. However, changes in absolute intensity can be influenced by photobleaching, variations of illumination intensity or fluorophore migration, and collecting spectral information from entire images may take a long time. Another solid state quantum system, a Nitrogen Vacancy (NV) center, was demonstrated to have an extremely high degree of accuracy in measuring temperature. This system was even used in a bio-environment where the intracellular temperature was measured [82]. In these systems the transition frequency between spin states [82] as well as the spin coherence time [83] has a temperature dependence due to thermally induced lattice strains. While NVs offer very accurate local measurements, obtaining a thermal map may be difficult. Also, their use among biologists in not yet widely accepted. Yet another biocompatable thermal probe was presented by Okabe et al. [84], who reported on a complex molecule who's fluorescence intensity and lifetime vary with temperature. They were able to reach sub degree accuracies, which was enough to detect striking phenomena such as an elevated temperature of the mitochondria inside the cell. Nevertheless, obtaining thermal images by measuring life times may be slow compared to intensity based techniques, and introducing such a complex molecule into a living organism may be challenging.

2.2 Temperature measurement using FPA

The thermometry method that was used in this thesis is based on the measurement of *Fluorescence Polarization Anisotropy* (FPA). This method was originally developed in the group of M. Orrit [85] and first applied to measure temperature of plasmonic nanostructures by Dr. G. Baffou during his post-doc in the our group [86]. During the work of this thesis we have extended this technique to bio-applications. In particular chapter 5 and 6 present thermal mapping in *in vitro* and *in vivo* systems.

The underlying physics relating temperature and molecular FPA is well established [87]. In general, a population of fluorophores illuminated by a linearly polarized light re-emits partially polarized fluorescence due to the random orientation of the molecular dipoles [87]. The polarization anisotropy r of the

fluorescence is defined as

$$r = \frac{I_{\parallel} - I_{\perp}}{I_{\parallel} + 2\, I_{\perp}} \tag{2.1}$$

where $I_{\parallel}$ and $I_{\perp}$ are the intensities of the fluorescence polarized parallel and perpendicular to the incident polarization. The measured value r is closely related to molecular rotation caused by Brownian dynamics according to Perrins equation

$$\frac{1}{r} = \frac{1}{r_0}(1 + \frac{\tau_F}{\tau_R}) \tag{2.2}$$

where τ_R and τ_F are rotational and fluorescence lifetimes respectively and r_0 a constant named limiting anisotropy (usually close to 0.4). When the temperature increases, the Brownian rotational motion of the fluorophores is accelerated. Hence, the molecules rotate more during their fluorescence lifetime. The more the molecules rotate during their fluorescence lifetime, the more the re-emitted photons lose the memory of the incident light polarization. Consequently, a temperature increase leads to a decrease of the degree of polarization of the fluorescence. Because FPA is a ratio of intensities it is not sensitive to factors related to absolute intensity variation. Using a suitable calibration, FPA leads to an absolute temperature measurement. This is one of the main advantages of this technique. The maximum temperature sensitivity is usually reached when τ_R is on the order of τ_F [87]. τ_R depends on the temperature T , the viscosity $\eta(T)$ and the hydrodynamic volume[1] V of the fluorophore according to the Debye-Stokes-Einstein equation

$$\tau_R = \frac{V\eta}{k_B T} \tag{2.3}$$

where k_B is the Boltzmann constant. Hence, V and η are the parameters one can adjust to optimize the sensitivity of the technique (i.e. to ensure that τ_R is on the order of τ_F). For instance, for common fluorescent molecules (approx. 1 nm in size) in aqueous media ($\eta = 10^{-3}$ m^2/s at $T = 25$ °C), $\tau_R \approx 10^{-10}$ s which is one order of magnitude smaller than a typical fluorescence lifetime ($\tau_F \approx 10^{-9}$ s). The rotational Brownian motion is too fast and the FPA is zero independently of the temperature. One way to solve this problem is to increase the viscosity η of the medium for instance by using a glycerol:water (4:1) mixture [86, 32, 85]. However, such an approach is prohibitive for any

[1] Hydrodynamic volume is the volume of a hard sphere that would diffuse at the same rate as the relevant probe.

application in biology due to toxicity. In general in biology the media viscosity is usually not a controllable parameter. For such systems the relevant adjustable parameter is the size of the fluorescent probe which would increase the τ_R, as is detailed in chapters 5 and 6.

2.3 Experimental tools

Optical setup

Implementation of the FPA temperature measurement as well as most other experimental data presented in this thesis were obtained on an in house built microscope[2]. Figure 2.1 shows a sketch of the system that enables FPA measurements as well as Two Photon Luminescence (TPL) measurements. The setup is composed of the following functional parts:

Fluorescence excitation: A blue diode laser of wavelength λ =473 nm is used to excite fluorescence. For FPA measurements, the laser is linearly polarized. A combination of a galvo mirror together with a $4f$ system is used to scan the beam across the sample. The beam is focused onto the sample with a an objective (either oil immersion or air objectives were used).

Optical heating beam: A red laser beam is delivered by a Titanium:Sapphire (Ti:Saph)[3]. It can be set to Constant Wave (CW) mode (usually for heating the sample) or pulsed mode (for excitation of TPL). The wave length of the laser is tunable, and was mainly used in the range of 720-850 nm. This beam can also be scanned using a separate galvo mirror and a $4f$ system. The beam can also be combined with the blue beam and can then be scanned together. The polarization state of the red beam is controllable via $\lambda\backslash 4$ and $\lambda\backslash 2$ wave plates.

Sample: The sample is placed on a piezo stage [4] which can be positioned or scanned in X, Y and Z with a 0.2 nm resolution. For a bio-sample, we used an incubating system that controls the temperature between room temperature up to 42°C, controls humidity and supplies an air flow with 5% CO_2[5].

Fluorescence collection: Fluorescence is collected on two Avalanche Photodiodes (APDs). The Fluorescence signal is split from the incoming blue beam

[2]The presented experimental tools were originally designed and built by Dr. G. Baffou. During this PhD many modifications and improvements were performed.

[3]Coherent, mira 900

[4]NanoCube P-611.3

[5]Live Cell Instrument, Chamlide IC.

with a dichroic mirror. It is then split by a polarization beam splitter into the orthogonal components, and focused onto two APDs. An optical band pass filter is placed in front of the APDs which blocks light coming from the blue or red laser. Digital compensation for the different collection efficiency of the APDs is done in the software by using a factor known as the g factor, which is commonly used in FPA measurements [87]. From the two APDs counts the FPA is calculated using equation 2.1.

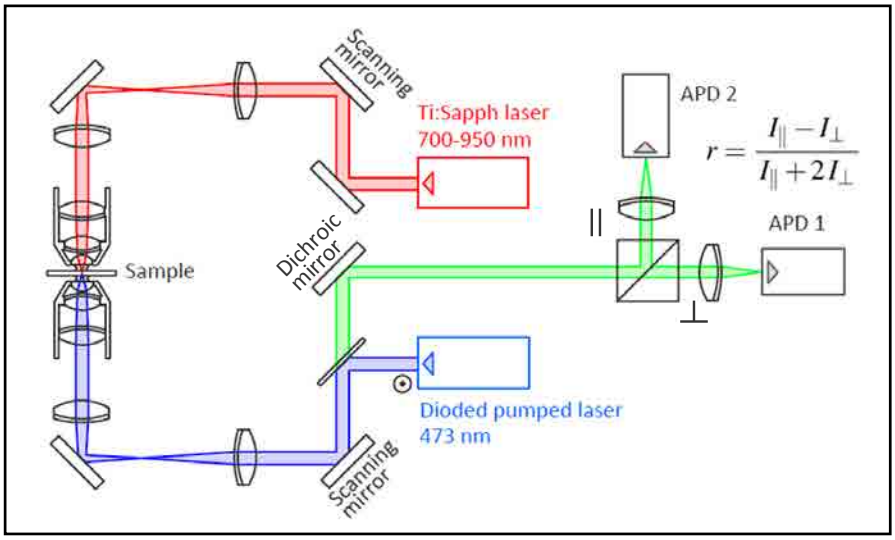

Figure 2.1: *Sketch of the FPA optical setup including: blue laser for excitation of fluorescence, red line for heating or TPL excitation, dichroic mirror for separation of fluorescence from blue light, polarization beam splitter to split the fluorescent signal onto two APDs.*

The experimental implementation of this system is presented in Figure 2.2. The setup is home built and is therefore very versatile. Indeed many temporary adjustments and modules were added and removed including an 808 nm diode laser which was used for heating, a pulsed blue laser together with a single photon counting system was used for lifetime measurements (as in 5, Figure 5.1), an optical chopper was placed in the red laser line for rise time measurements (chapter 3, Figure 3.10), a fluorimeter with a heating resistor

was built for FPA temperature calibration measurements (chapter 5, Figure 5.1).

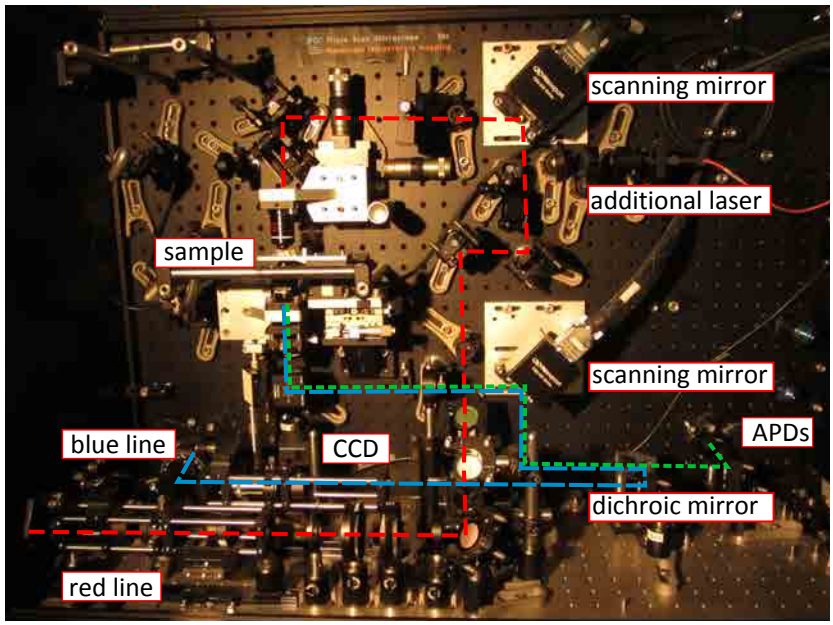

Figure 2.2: *Photograph of the setup described in Figure 2.1.*

Experimental software (LabView)

To run the setup a LabView program was written, and a Graphical User Interface (GUI) designed (see Figure 2.3). Two LabView cards are used: one to perform hardware counting of the APD counts and another to control the scanning of the two scanning mirrors and the piezo stage of the sample. The GUI interface allows for different fast and easy actions such as: setting scanning parameters (of sample blue beam red beam), moving the beams or sample, file management and viewing of live scans in real time.

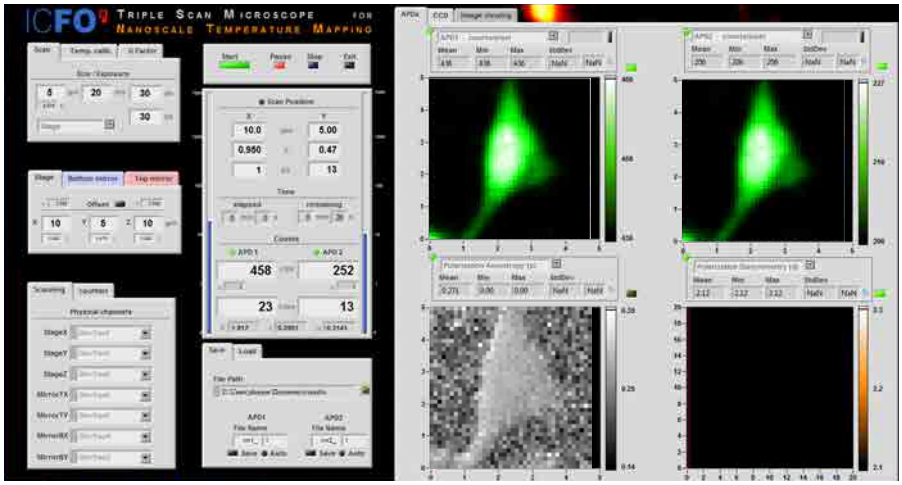

Figure 2.3: *LabView GUI during a fluorescent scan of a GFP transfected cell. On the right side there are three images, two of the orthoganal polarization intensities (green) and one of the calculated FPA (gray). These images are presented in real time during the scan. On the left side there are different buttons which control: parameters of the scan, file management, hardware inputs. There is also a panel to view the counts on each APD.*

Image analysis software (matlab)

Once the scans are saved using the LabView program, they are processed using a custom made matlab GUI that is presented in Figure 2.4. This GUI permits easy and quick performance of frequent operations. The main tasks that can be done are: importing the data, assigning a color map to the data, viewing and saving of the different scans, applying various custom filters (for example smoothing), converting FPA images into temperature images using the relevant calibration, calculating statistics on Figures or sub regions of interest.

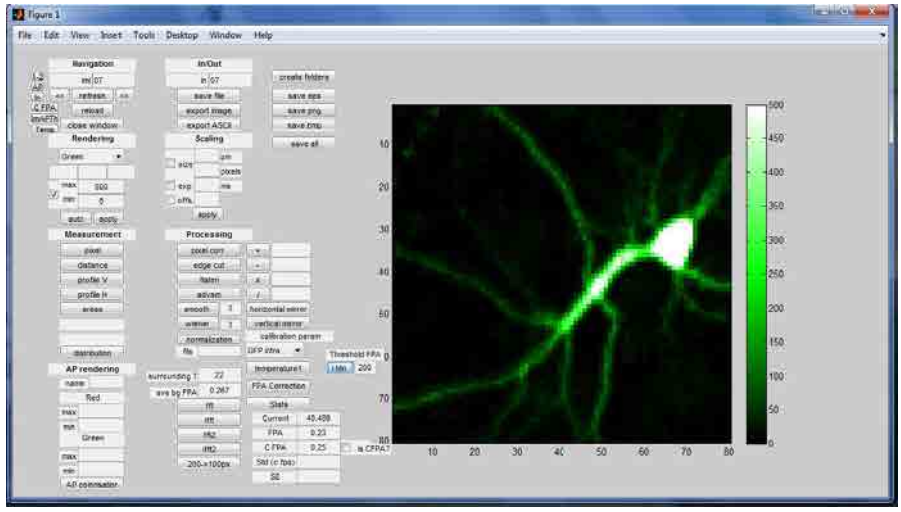

Figure 2.4: *Matlab based GUI for image analysis. On the right side the loaded data is color coded and presented (in this case an intensity scan of a GFP transfected neuron). On the left there are buttons that control different options related to data viewing saving and image processing.*

3

Adaptive photothermal lens

3.1 Introduction

Motivation

In the current general trend towards miniaturization, integrated micro-optical elements have played a central role in the development of high-density data storage and optical displays [88], and are becoming a crucial ingredient in the miniaturization of imaging systems [89, 90]. In all these applications, fine alignment and focus adjustment is usually performed mechanically; thus limiting the accuracy, size and operation speed of devices. To overcome these limitations, much effort has been put into developing adjustable micro lenses that eliminate the need for mechanical parts. Here, we propose a novel adjustable microlens that exploits the temperature dependence of the refractive index of matter. Through a proper micro-engineering of the temperature distribution at a surface patterned with plasmonic photo-heaters, we form a gradient of refractive index whose profile and contrast are controlled by the intensity profile of a heating laser. Such a level of control enables us to transform any conventional lens into an effective lens whose image focal plane can be finely shaped optically. We demonstrate tunability of tens of microns with sub-nanometer accuracy along with time-responses as fast as 200 μs. The applicability of this photothermal

lens is tested in the framework of optical microscopy and adaptive optics.

State of the art

Reconfigurable optical elements that enable dynamic control of optical paths are important components of the last generation of commercial optical devices. Among them, liquid lenses operate by shaping the surface of a liquid drop by electro-capillarity [91]. Although liquid shaping implies some constraints for integration into complex devices it has shown to be a powerful way to adjust focus with a few millisecond time response. Other approaches of reconfigurable optical lenses include refractive-index-adjustable liquid crystals [92], pH-tunable hydrogels [93], and pressure regulation of polymer surfaces [94]. Another widely used active element is the deformable mirror whose surface can be dynamically deformed using MEMS technology [95]. With a time response on the order of 100 μs, this technology has greatly contributed to the field of adaptive optics with applications especially in astronomy and microscopy.

In this chapter, we introduce a novel concept that enables us to transform any conventional (static) optical lens into an effective adaptive *Photo-Thermal Lens (PTL)* whose image focal plane can be dynamically shaped by a control optical signal. Our approach is based on the physical phenomena whereby the refractive index of a material n changes with temperature. A local increase of temperature induces a gradient of refractive index that affects the propagation of optical rays. In the early 2000's it was proposed to exploit this effect for the detection of single absorbing nano-object [24, 96]. In such two colour experiments, one laser is used to heat up the nano-object, while the second probes the associated local change of refractive index. This has enabled researchers to accurately locate and dynamically track single metallic nanoparticles [24], carbon nanotubes [97], as well as single molecules [96]. In parallel, recent advances in so-called thermo-plasmonics have led to an unprecedented control of temperature on the micro- and nano-scale. Noble metal nanostructures, supporting localized surface plasmons, can be designed to act as efficient heat sources remotely operated by light [19, 98]. Beyond enabling temperature gradients down to the nanometer scale [98], this approach benefits from very fast heating / cooling dynamics. The rationale behind the present work is to exploit such control to design a temperature landscape that can locally modify the focal plane of a conventional optical lens and ultimately transform it into an adaptive imaging element.

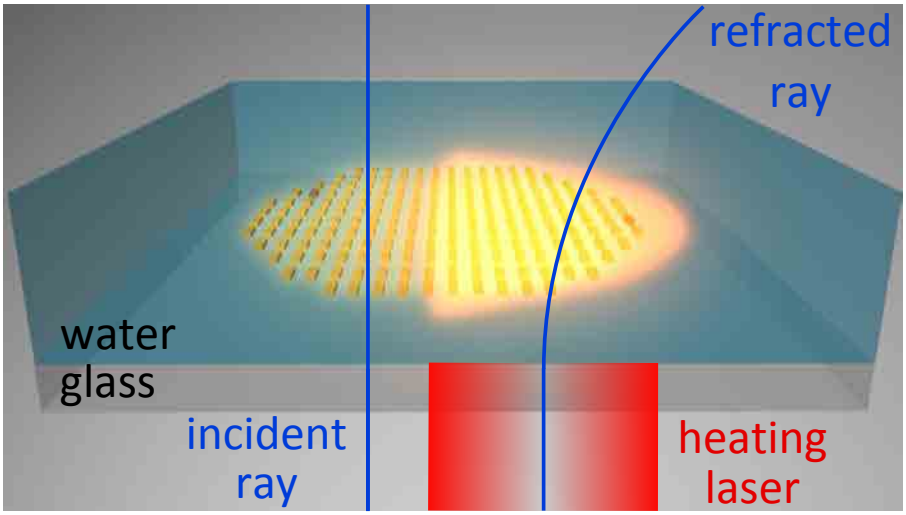

Figure 3.1: Principle of thermal-induced lens. *In presence of a heating laser (red beam), the temperature in the vicinity of an array of absorbing nanostructures is increased. The resulting change of optical index refracts a collimated blue light beam*

3.2 Modeling of a photothermal lens

Principle

In the implementation presented here (see scheme in Figure 3.1), the surface of a glass cover slip is patterned with plasmonic nanostructures that create, upon illumination, the desired distribution of temperature increase [98]. On top of the patterned surface is a 100 μm-thick fluidic cavity filled with water that acts as the index-changing medium [99]. Alternatively, other materials with significant $\Delta n/\Delta T$ can be used instead of water.

Thermally induced optical index profile

In order to illustrate the concept of an adaptive thermal lens we first simulate the optical lensing effect induced by a micrometer-sized heat source[1]. We calculate the temperature profile induced by a 5 μm homogeneous gold pad

[1]Simulations were performed by Jordi Morales, then a Master student in the PNO group. Modeling approach was derived together with and then implemented by Dr. Renaud Marty.

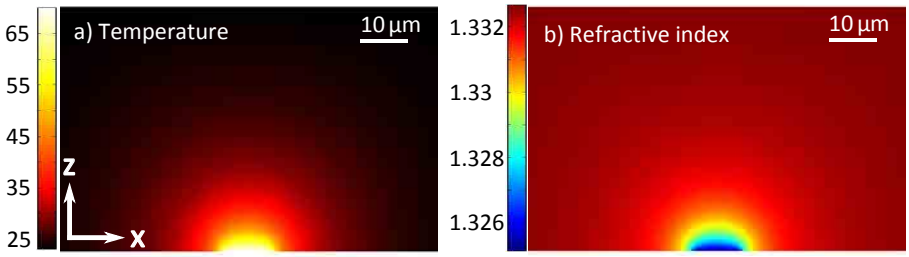

Figure 3.2: Temperature and optical index profile induced around a heated gold disc. *a) Temperature map around a 5 µm radius gold disc heated to 70 °C and submerged in water. b) Associated refractive index map calculated for a wavelength of 400 nm to match the experimentally used wavelength. Changes on the order of 10^{-3} can be seen.*

heated to 70 °C a lying on a glass substrate and immersed in water (Figure 3.2a). Because of the cylindrical symmetry, the configuration is fully defined by a slice across the XZ plane. Using the temperature dependence of the optical index of water [99], we obtain the profile of the optical index as shown in Figure 3.2b. The refractive index of water decreases with increasing temperature, and so features a minimum at the heat source. Such a gradient leads to a negative phase accumulation for light that propagates across the system, which is associated to a divergent lens.

Characterization of the lensing effect: thin lens approximation

In the framework of the thin lens approximation, the power (also called vergence) of a lens is given by

$$P = \frac{1}{f} = \Delta n[\frac{1}{R_1} - \frac{1}{R_2} + \frac{\Delta n d}{R_1 R_2}] \tag{3.1}$$

where P is the power, f is the focal distance, d is the thickness and Δn is the refractive index variation. In our case R_1 is infinite (planar surface) and R_2 is estimated by the Full Width Half Maximum (FWHM) of the in-plane optical index profile. It is important to notice that the thin lens model is valid here because we consider structures ($\approx$10 μm) and thus lenses which are much larger than the considered optical wavelength (400 nm).

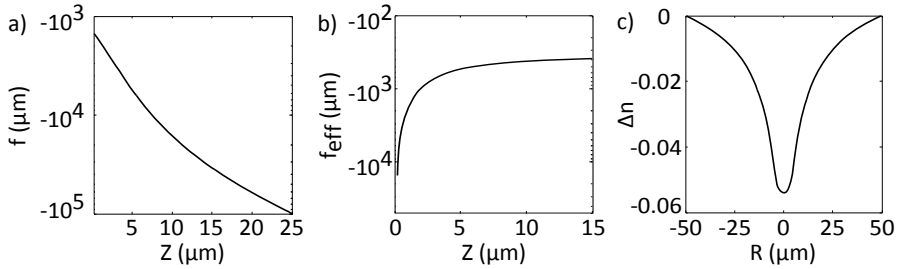

Figure 3.3: From an optical index profile to an effective lens. *a) To model the system, the medium is divided into thin layers and each layer is considered as a thin lens with an associated focal distance. The evolution of this effective focal distance is presented as a function of the height Z of the considered layer of water starting from the heating structure. b) Total effective focal distance in dependence of the height of integration Z. Most of the lensing effect is caused by the layers that are closest to the heating structure (3 µm in this case). c) Refractive index profile variation integrated along the Z-axis.*

We consider the configuration depicted in Figure 3.1. We divide the media, for which the optical index changes as function of temperature, into layers and associate a thin lens to each layer. Using the thin lens model, we then calculate the focal distance for each planar layer inside the water (Figure 3.3a). As expected, the focal distance is shorter close to the disc and increases rapidly with the height since the lensing vanishes. As the power of a stack of lenses can be added, we can then describe this configuration by a single effective lens.

In Figure 3.3b, the total effective focal distance is given as a function of Z, and is calculated by

$$\frac{1}{f_{eff}(z)} = \int_z dz' \frac{1}{f'(z')} \tag{3.2}$$

In this case, we observe a convergence toward -400 μm when Z is close to 2 μm. The Z value for which the focal distance converges corresponds to the thickness of the effective lens.

In addition, by integrating the refractive index variation along the Z-direction, we obtain the spatial profile of the thermal-induced lens (Figure 3.3c). An in-plane lateral size of 20 μm, estimated by the FWHM of optical lens profile in Figure 3.3c, was attributed to the effective lens.

Thus, the thin lens approximation allows us to describe a 5 μm radius disc heated to 70 degrees immersed in water as a thermal lens of -400 μm focal

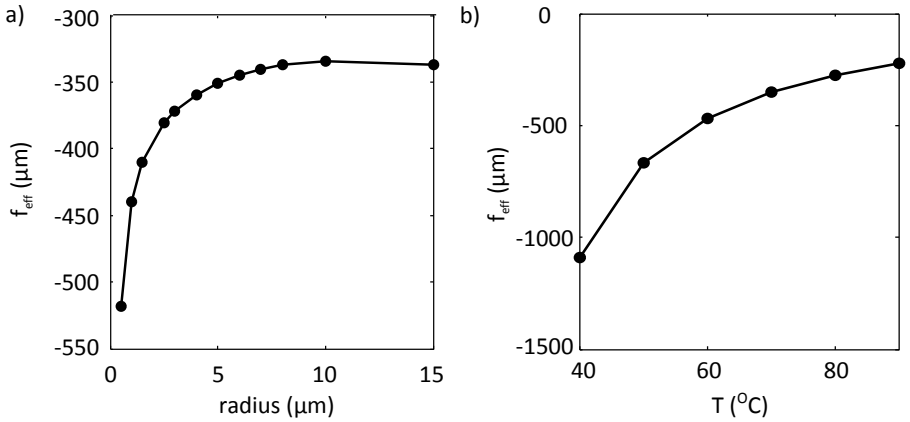

Figure 3.4: Influence of heating radius and temperature on the focal distance of the effective lens. *a,b) Variation of the effective focal distance induced either by changing the disc size while maintaining a fixed temperature ($T = 70^{\circ}C$ in a) or by varying the temperature of the disc and fixing the radius ($r = 5\mu m$ in b).*

distance, a few microns thick and an in-plane lateral size of 20 μm.

Parameters for control of the thermal lens: heating radius and temperature

The previous section shows that by using the thin-lens approximation, it is possible to define a focal distance associated to a thermal-induced lens. Here we go a step forward and show how to control this focal distance. In Figures 3.4a and 3.4b we plot the influence of the disc diameter and temperature on the effective focal length. The effective focal distance displays an asymptotic behavior while increasing the size of the disc, showing that the lensing power does not further increase for radius larger than 10 μm. Reciprocally, for radii smaller than 5 μm, we observe a strong decrease of the focal distance of the lens when reducing the size of the structure. This behavior originates from the diffusivity of temperature that spreads over a few microns considering a water environment whatever the considered heating source size.

Figure 3.4a thus demonstrates that an efficient thermal lens cannot be smaller than a few microns. A 5 μm-radius heating source appears to be a good compromise between the lensing ability of the system and its size reduction. After

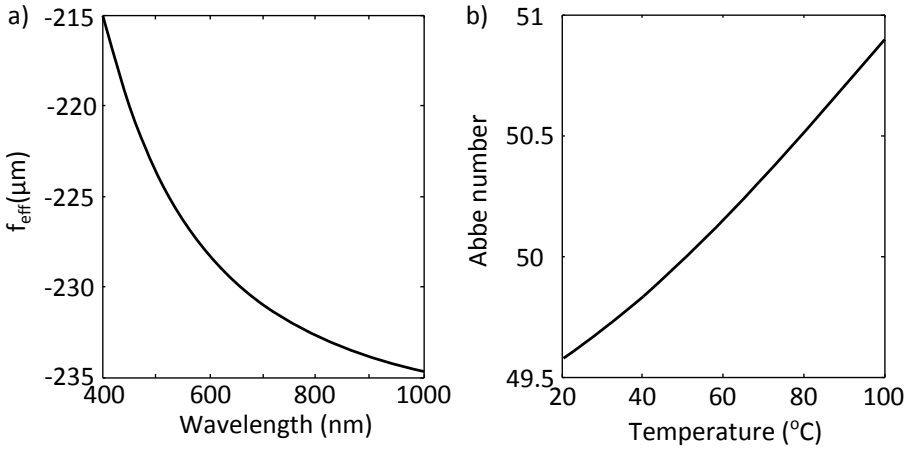

Figure 3.5: Chromaticity associated to the effective lens. *a) Focal distance of a thermal lens based on a 5 µm radius gold disc heated to 70 °C in dependence of the wavelength used for the lensing. In the main text, the focal distance associated to Figures 3.2 and 3.4 have been calculated for a wavelength of 400 nm. b) Evolution of the Abbe number as a function of the temperature for a water based thermal lens.*

choosing the best size for the heating structure, we show in Figure 3.4b that changing the temperature of the structure enables tuning the effective focal distance over a wide range. Indeed, an increase of the temperature of the disc from 40 to 90 degrees leads to a decrease of the focal distance from -1100 μm to -220 μm, respectively. This is particularly interesting since it allows dynamic tuning of the lensing effect only by changing the intensity of the heating laser. A natural characteristic of dynamical systems is the time response which in this case is given by the size of the heating source and the thermal diffusivity of the environment (see equation 1.8). As discussed at the end of the chapter, the typical time response of such thermal lens is a few 100 μs.

Lens chromaticism

We have characterized the chromaticism of the considered water-based lens using a theoretical model. To do so, we calculated the focal distance of the effective lens as function of the wavelength by using the dispersion of the optical index of water described elsewhere [100]. Figure 3.5a shows a 10% variation of the effective focal distance while changing the wavelength from 400 nm to

1000 nm. To characterize the chromaticism, we have then calculated the Abbe number (Figure 3.5b). A small increase of the Abbe number is observed when increasing the temperature but its value remains close to 50. It is important to underline that the larger this parameter is, the smaller the chromaticism. It is possible to tune the value of the chromaticism by choosing the environment used to get the lensing effect. In many applications the chromaticism can be important, for instance a strong chromaticism can allow to design a wavelength selective optical element whereas the smallest values could be used to create broadband lenses.

3.3 Experimental implementation

Heating of plasmonic structures

Based on these simulations, we perform a first set of experiments to demonstrate the feasibility of the PTL concept and assess its performance. In the present implementation we exploit the capability of plasmonic nanoparticles to generate heat when illuminated at their plasmonic resonance to create the desired distribution of temperature [19]. Our heat source is formed by a finite periodic array (pitch= 300 nm) of Gold Nanorods (GNR) (120 x 80 x 50 nm^3) that lead to a maximum of absorption at 800 nm (Figure 3.6a), at their longitudinal plasmon mode, achieved when the incident field is linearly polarized along the GNR long axis.

First, the heating capability of the fabricated plasmonic patterns is assessed using thermal microscopy based on measuring the *Fluorescence Polarization Anisotropy* (FPA) of fluorescein in a water/glycerol mixture (see chapter 2). Figure 3.6b, shows the linear dependence of the maximum reached temperature on the power of the 800 nm CW heating laser. By rotating the linear polarization of the heating laser by 90°C, the temperature decreases by half (green curve), which gives a good approximation of the actual contribution of the plasmon resonance to the heating. Interestingly, the full disc presents a similar temperature map to the resonant GNR disc but the latter enables both a larger increase of the temperature and a higher transparency of the lens. Finally we verify that for the same power of the heating laser, no significant increase of temperature is measured in absence of any heating structure (black curve).

Characterization of the lensing effect

To characterize the PTL effect, we design a simple experimental configuration (depicted in Figure 3.7a) in which we monitor the changes in the focus of

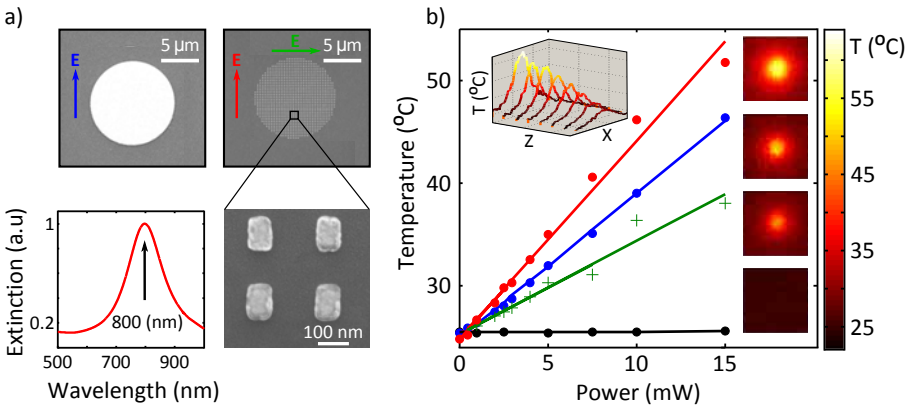

Figure 3.6: Experimental measurement of the temperature increase of a photothermal lens. *a) SEM images of a full 5 µm radius gold disc (left), and a 5 µm radius disc made of GNR (right). A higher magnification image of the 120x80x50 nm^3 GNRs is presented. The corresponding extinction spectrum displays a plasmonic resonance at 800 nm. b) Temperature as a function of power from a 800 nm laser shined on a GNR disc excited at the Surface Plasmon Resonance (SPR) with a parallel polarization (red dots), a GNR disc excited off resonance using a perpendicular polarized configuration (green crosses), a full gold disc (blue dots) and in absence of any structure (black dots). Temperature maps of the different configurations are presented for a heating laser power of 15 mW. The top left inset shows a cross cut of the temperature evolution as a function of the height above the GNR disc shined on with a 800 nm parallel polarized laser.*

a blue laser beam propagating through the PTL. The thin cell containing the plasmonic structures immersed in water is added into the optical path of a 50X microscope objective as depicted in Figure 3.7a. A sample is placed above the PTL chamber and is imaged on a CCD.

On top of this chamber another chamber filled with a liquid (for impedance matching) is placed and the beam intersection with the top coverslip is imaged on a CCD. First, we performed an experiment, in which we image the blue laser beam profile for different heating laser powers P_{NIR} (Figure 3.7b). The CCD images of the blue laser probe spot at fixed height (Z=4 μm) for different values of P_{NIR} enables us to visually appreciate the defocussing (as in insets of Figure 3.7b). For further quantification, we measure the vertical profile of the blue beam, by monitoring the Z-dependence of the blue intensity integrated over an area slightly larger than the size of the focus spot (P_{NIR}=0 mW (black), 10 mW (blue) and 30 mW (red)). We find that the focal point is Z-shifted by 5 μm and 15 μm for P_{NIR}=10 mW and P_{NIR}=30 mW, respectively. This allows us to establish a value of sensitivity of the focus shift in relation to input power of 500 nm/mW, which corresponds to 230 nm/°C when using the temperature power calibration of Figure 3.6b (red curve).

Subsequently, we record the focus shift as function of laser power (Figure 3.7c) and obtain a linear relationship. Finally, we quantify the lateral dimension of the region affected by a 5 μm PTL. To do so, a grating was imaged before and after activating the PTL (Figure 3.7d). The contrast of the grating was measured in both cases and Figure 3.7d displays the grating contrast normalized by that of the grating with no thermal lensing. These data show that the 5 μm PTL affects the focus over a region of about 13 μm (FWHM of curve Figure 3.7d). This value is close to the one obtained theoretically when considering a gold disc having the same size and heated to about 80 degrees Celsius.

Spatial shaping of thermal lensing

A characteristic defect for a lens is astigmatism. In the case of a PTL, this is not an issue since the diffusivity of temperature tends to create a smooth and isotropic profile and then remove any astigmatism that could occur due to small imperfections of the structure. Nevertheless, it might be interesting to intentionally create astigmatism for some applications. Even if the temperature tends to spread out as it is a diffusive process, it is still possible to force astigmatism.

To highlight this point, a special lens shape was designed (Figure 3.8a) and the temperature induced in its vicinity measured by FPA. When considering an

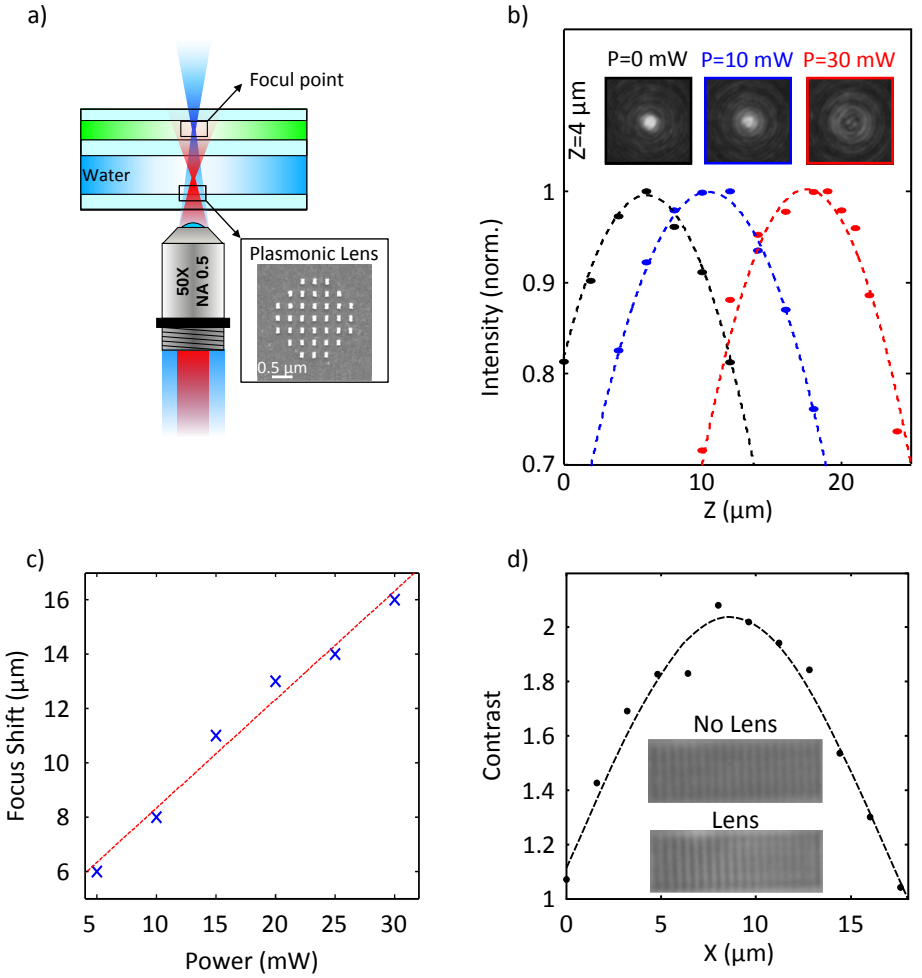

Figure 3.7: Experimental characterization of the thermal lens. *a) Scheme of the experimental set up. The plasmonic structures are sealed in a closed chamber surrounded by water and illuminated with a red 800 nm laser focused with a 50X microscope objective (NA=0.5). The focus of the red laser covers the whole 5 µm radius gold disc. The light emitted by fluorescent molecules (fluorescein) located above the chamber and excited by a focused 473 nm blue laser is collected by an APD. b) Intensity of the focused blue beam at different piezo stage heights Z and for 3 different powers of the thermal lens (black: no thermal lens, blue: 10 mW, red: 30 mW). When 30 mW is applied the blue focal point is shifted by almost 20 µm. The images at the top of the Figure correspond to the image of the blue laser beam at a fixed height (Z=4 µm) for the different incoming powers. c) Focus shift as function of laser power shined on the thermal lens. d) Contrast of a 2.5 µm grating as a function of the location X with thermal lensing normalized by the contrast without a thermal lens images are presented in the inset.*

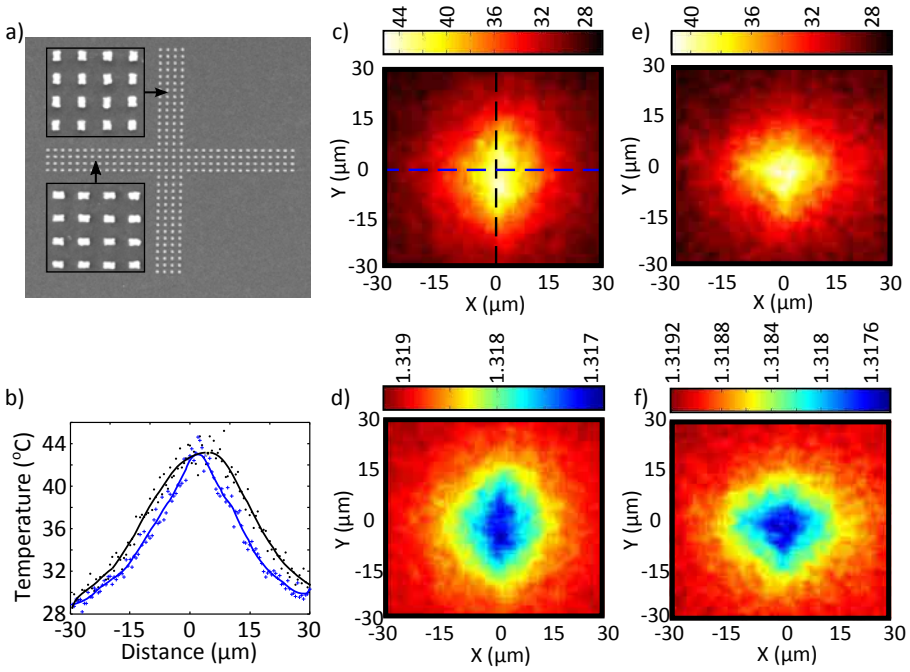

Figure 3.8: Anisotropic lens by a birefringeant optical index profile. *a) Scanning electron microscopy image of a cross shape structure made of GNR by electron beam lithography. The GNR present a resonance in the NIR. The two insets correspond to a zoom of each arm of the cross and show that the GNRs are oriented perpendicularly in each arm. c) Measurement of the temperature above the structure displayed in a) for a NIR heating laser polarized along the Y-axis. The GNRs of the Y-oriented arm of the cross are excited at their SPR whereas the GNRs of the other arm are out of resonance for this configuration. The resonantly excited GNRs produce heat more efficiently, which leads to an asymmetric profile of the temperature. This asymmetry is highlighted in Figure b) where two cross cuts (represented with dashed lines in Figure c) are plotted. d) Using the temperature dependence of the optical index of water, we have deduced the map of the static optical index of water resulting from the temperature map displayed in c). e-f) Similar study when considering a heating laser polarized along the X-axis. As expected, we observe an asymmetry oriented along the resonant arm of the cross (X-oriented arm) in the temperature and optical index profiles.*

asymmetric structure (Figure 3.8a) illuminated with an electric field polarized along its main axis, the temperature distribution is anisotropic (Figure 3.8b,c). As the temperature increment induces a change in the optical index of the surrounding medium, such a configuration creates an anisotropic optical index. In Figure 3.8d,f, we show the optical index map of water deduced from the temperature distribution. Then, a light beam crossing the region above the heated plasmonic structures experiences an optical path that depends on the orientation of its k-vector with respect to the X and Y axis. Therefore, this can be seen as a tool to create an optically controlled birefringence at the micro scale. By integrating in the X and Y directions of Figure 3.8c, we find a birefringence of

$$B = \frac{\int \Delta n(r,\lambda) dy}{\int \Delta n(r,\lambda) dx} = 0.78 \tag{3.3}$$

where Δn is the optical index variation induced by the temperature growth. Such a configuration is close to what happens with a liquid crystal where an extraordinary axis can be created by applying a voltage (static electric field) [101].

Finally we show control of the direction of the extra-ordinary axis of birefringence by changing the polarization of the heating laser beam. To this end, the nano-antennas inside each arm of the cross are oriented perpendicularly (inset of Figure 3.8a) so that the structures of only one arm are in resonance with the heating laser beam when considering a given polarization. Indeed, Figures 3.8c,e show that the extraordinary axis can be aligned either along one arm or the other by adjusting the light polarization.

Influence of the surrounding media

The concept of a PTL is general and can be implemented with a plethora of different materials. Indeed, the only requirements would be a material with a temperature dependent optical index, and transparency of the material in the relevant wavelength range. up to now, we have discussed the thermal lensing effect in a water environment but our experimental system can be used with different liquids or gases. For instance, a lensing effect was measured in presence of octane and a 4:1, glycerol:water mixture. The choice of octane appears particularly interesting since a significant lensing effect is observed with only 1 mW of heating laser power instead of few tens of mW required in the case of water (see Figure 3.7 in the main text). This originates from the strong dependence of the optical index of octane at room temperature (5 times stronger than water around room temperature). This example illustrates the importance of

the choice of the thermo-optical material. Depending on the targeted application, the surrounding environment from which the lensing effect originates will have to be adapted. For instance, one can choose a solution that presents a strong optical index variation close to room temperature obtaining a low energy consumption thermal lens. Yet in other applications, it might be interesting to take the largest optical index variation at the maximum reachable temperature in order to have the strongest lensing effect.

Time response of the lensing effect

To complete the characterization of the PTL, we experimentally characterized its time response. To this end, the fluorescence intensity coming from fluorescein molecules is monitored with high temporal resolution when switching the lens on and off. This is repeated for different lens radii. The characteristic time of a thermal process can be roughly estimated by applying dimensional analysis to the heat transport equation and is given by (explained in equation 1.8):

$$\tilde{t}_T = \frac{L^2}{\alpha}$$

where $\tilde{t}_T$ is the characteristic time for temperature establishment, L is the characteristic size of the system, and α is the thermal diffusivity of the media. As discussed at the beginning of the chapter, the speed of the lensing is a pertinent parameter for applications. When changing the medium responsible for the lensing effect, we not only changed the spatial features of the lens (height, size and focal distance for a given irradiance power) but this also modifies the diffusivity and thus the time response of the lens.

Figure 3.9 shows that the best configuration is to combine small heating structures with a high thermal diffusivity for the environment. As discussed previously (see Figure 3.4a), structures smaller than 5 μm have a smaller ability to increase the temperature in the surrounding. Therefore, the best option to decrease the response time while keeping good thermal lens efficiency consists in finding a medium with a high thermal diffusivity. Some metals and gases have a thermal diffusivity that reaches 10^{-4} m^2s^{-1} whereas this value is close to 10^{-7} m^2s^{-1} for liquids. Metals cannot be used to form a thermal lens because they reflect light. In our chamber, the insulation is not good enough to use thermal lenses based on gas. Nevertheless, the use of gas appears promising since the optical index of gas strongly depends on the temperature (Gladstone law) and the lensing effect might be even faster than 0.1 ms.

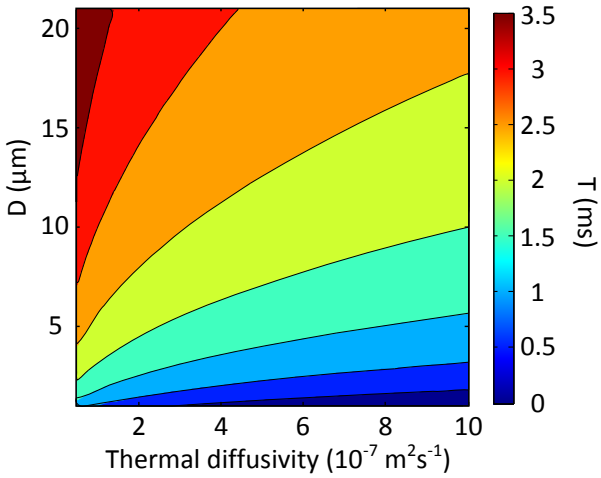

Figure 3.9: Time response of a thermal lens: role of the heating structure and lensing medium. *Switching time (in ms) in dependence of the thermal diffusivity of the environment and the typical size D of the heating structures.*

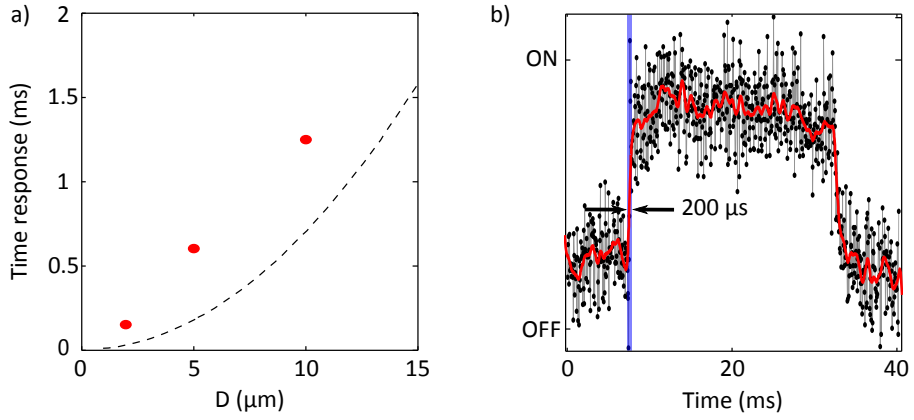

Figure 3.10: Response time for a water based thermal lens. *a) Time response of thermal lens in dependence of the typical size of the heated structure (diameter of the disc). The red dots show experimental results, and the broken line represents a simplified model as specified in the main text. b) Experimental data showing the rise time of the thermal lens made of a 2 µm diameter gold disc.*

In Figure 3.10a, there is a plot of the relationship in equation 1.8 for water (α=1.43 10^{-6} m^2s^{-1}) presented with a dashed black line. Experimental measurements performed on gold discs of 10, 5 and 2.5 μm diameters have given thermal lensing rise times of 1.5, 0.6 and 0.2 ms, respectively. Figure 3.10b shows the rise time measured when heating up a 2 μm diameter gold disc. Our data indicate that the thermal lens can be much faster than a liquid lens or other tunable micro lenses for which the time response is usually more than a few ms.

3.4 Applications

Adaptive optics

We demonstrate the applicability of the PTL as an adaptive optical element for microscopy. Using the optically controlled heat generation, it is possible to vary not only the power of the lens but also to easily and dynamically move the location of the lensing area. As an example of such an application, a sample made of a few hundred micrometers GNR array was fabricated. The NIR heating laser is moved to different regions of this array with the aid of a galvanometric mirror. In this configuration the size of the thermal lens and the heating area is defined by the size of the heating beam, approximately 10 μm in radius. As a first test sample we use a sample made of randomly distributed polystyrene beads of different sizes (1, 3, 5 and 8 μm). In Figure 3.11(a) the sample is initially placed out of focus (no heating laser). Subsequently we shift the position of the NIR laser and generate the thermal lens in different locations. We recorded the corresponding optical images and see that the image focal plane is locally adjusted to bring the 3 μm beads into focus. Indeed, while ensembles of 3 μm beads appear blurry in Figure 3.11a, they can be individually resolved in Figure 3.11b,c and d.

Application to cell imaging

In the last section we showed an application where we move the location of the thermal lens in the plane. Another degree of freedom which we can exploit is to change lens power to focus at different Z planes. This is done by changing the heating laser power (as characterized in Figure 3.7). This ability can be exploited in various different fields, but here we choose to show it in a bio-application. In this case it is especially interesting because samples are by nature 3D and by looking at different planes distinct features can be exposed.

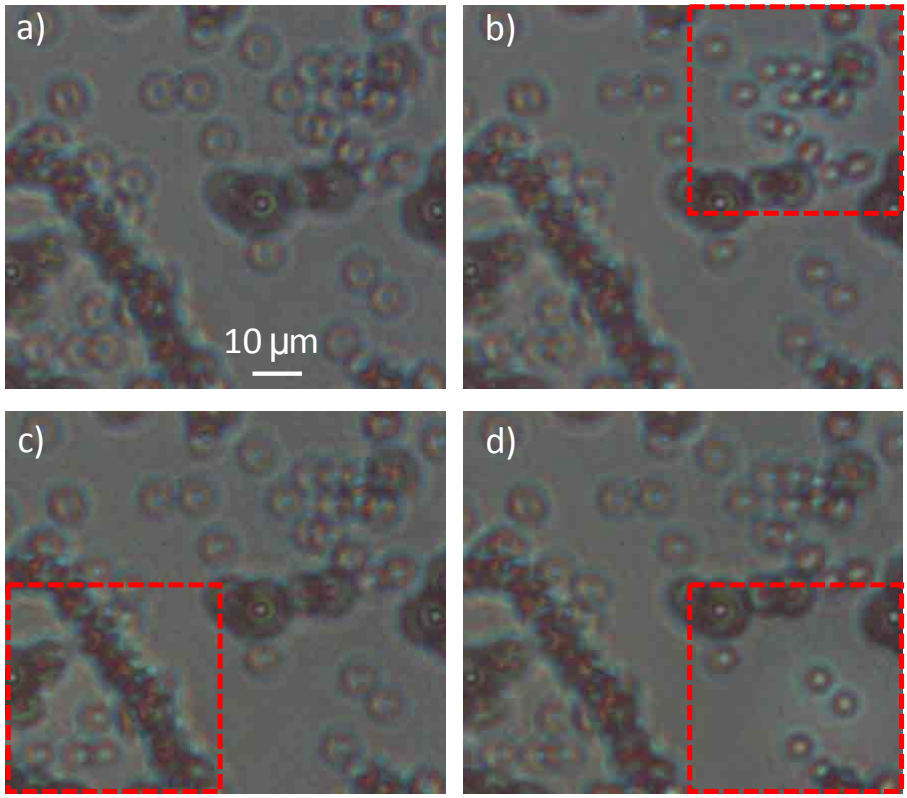

Figure 3.11: Thermal lens applied to adaptive optics. *a) Bright field imaging of a sample made of a mixture of beads of sizes: 1,3,5 and 8 µm. The Figure is defocused. b,c,d) Thermal lens is induced in different areas of the image, highlighted by a red box in each Figure. The thermal lensing changes the focus of the image and the beads are brought into focus to a point so that they can be easily separated.*

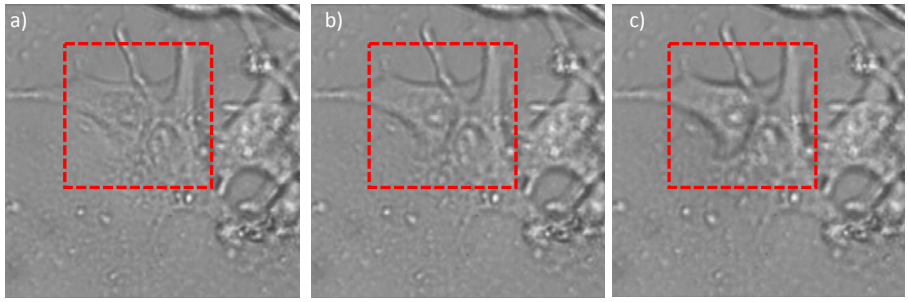

Figure 3.12: Thermal lens applied to imaging. *a,b,c) Thermal lens applied to biology. Bright field imaging of B16-F10 cells without (a) and with applying a thermal lens (b-c).*

In Figure 3.12 B16-F10 cells are placed above a PTL. The location of the center of the PTL is marked with a red square. In the different sub-figures, the power of the thermal lens is varied between 0,10 and 30 mW in a,b and c respectively. Indeed, distinct cellular features can seen in the different images.

3.5 Conclusion

The PTL combines accurate and fast focus control with very simple implementation on most optical devices. Among potential applications, the PTL could be used to individually control the focus of arrays of micro-lenses, with important applications in parallel optical configurations. Another foreseen application is related to the last set of experiments presented here, using the PTL as an adptive optical element operating in transmission for 3D imaging. For such applications the optical operation of the PTL may need to include various electronically controllable separate light sources.

4

Plasmon assisted optofluidics

4.1 Introduction

Internal dissipation inside material by a Joule mechanism results in heat generation. When considering heating in a fluid environment, a voluntary or involuntary fluid convection is induced. This is particularly true when considering plasmonic structures shinned on with light. Indeed, Gold nanoparticles supporting Localized Surface Plasmon (LSP) resonances can act as punctual nano-sources of heat, remotely controllable by laser illumination [16]. Along with the fast growing interest in the biomedical field [6, 102], nanoscale control of temperature [36] opens up multiple new opportunities in nanotechnology including chemistry [103], phase transition [104] and material growth [105]. Beyond this emerging research, another concept that has only marginally been addressed is the ability to exploit plasmonic nanoparticle heating to control fluid motion at the nanoscale [106].

Controlling fluid dynamics using plasmonic heating is first motivated by the possibility of engineering fluid motion at the nanometer scale as a strategy to develop future elementary functionalities in micro- and nano-fluidic experiments. Furthermore, since heating is unavoidable when illuminating plasmonic nanostructures, there are numerous optical experiments in which an undesired fluid motion could affect or interfere with the phenomenon under investigation. In that case, quantifying the temperature increase and the amplitude of the fluid velocity is crucial to differentiate between the various effects. As an example, let

us mention surface plasmon-based trapping in which enhanced plasmonic fields at a patterned metallic surface are used to trap single tiny objects in solution [107]. While prior studies have evoked that heat-induced fluid dynamics may contribute to plasmon-based trapping, there has not yet been any demonstration nor quantification of such contribution.

In this chapter, we develop a theoretical and numerical description of the photothermal-induced fluid dynamics around plasmonic nanostructures[1], and then present an application based on this phenomenon. The primary objectives are to work out the orders of magnitude and from them discuss the feasibility of controlling fluids at the nanoscale using plasmonic structures. To this end, we develop the theoretical framework required to describe the involved physics. More precisely, the optically induced nanoscale temperature profile detailed in chapter 1 is taken as the source of fluid motion in a hydrodynamic description. Dimensional analysis of the constitutive equations are performed to derive the characteristic orders of magnitude regarding time scales and fluid velocity. In a second part, we carry out numerical simulations using a Finite Element Method (FEM) to compute the temperature profile and velocity field around a gold disc illuminated at its plasmonic resonance. Our results provide some insight into the actual contribution of thermal effect in surface plasmon trapping. Finally, based on these principles, we describe a strategy to induce directional flow in a microfluidic environment, resulting in a micro pump. We present the simulations and show a proof of concept using a fabricated sample in an experimental configuration.

4.2 Theoretical framework

Shining light on a plasmonic nanostructure immersed in a liquid leads to sequential physical processes. First, light is absorbed by the plasmonic particles. A part of the light is converted into heat. Subsequently the heat diffuses through the surrounding medium, which induces fluid convection. The physics of this last process is described in the following sections.

Thermal-induced fluid convection at the nanoscale

In this section, we discuss the velocity field surrounding the plasmonic particle subsequent to the temperature increase. By simple dimensional analysis, we work out the characteristic orders of magnitude and the dimensionless numbers

[1]This work was performed under supervision of Dr. Guillaume Baffou, with whom the theoretical model was derived, and who supervised over the numerical simulations.

(Reynolds and Rayleigh) that characterize the different fluid regimes (laminar, turbulent, viscous etc.) at the nanoscale.

Like the temperature, the fluid velocity is well defined and its expression is valid since the molecular mean free path of the fluid is much smaller than the characteristic length of the system[2]. Due to the heat generated in the nanoparticle, the fluid in its vicinity features a temperature increase giving rise to a decrease of the mass density and an upward convection of the fluid (Archimedes force). The general equation governing this process is the Navier-Stokes equation[3] [108]

$$\rho\,\partial_t \mathbf{v}(\mathbf{r},t) + \rho(\mathbf{v}(\mathbf{r},t)\cdot\nabla)\mathbf{v}(\mathbf{r},t) = \eta\nabla^2\mathbf{v}(\mathbf{r},t) + \mathbf{f}_{\mathrm{th}}(\mathbf{r},t) \tag{4.1}$$

where ρ is the fluid mass density, η the dynamic viscosity, $\mathbf{v}$ the fluid velocity and $\mathbf{f}_{\mathrm{th}}$ the volumetric force due to temperature non-uniformity. This thermal force $\mathbf{f}_{\mathrm{th}}$ can be evaluated by the Boussinesq approximation [108]. This approximation accounts for the temperature dependence of the density by adding an external buoyancy force term, which is dependent on the temperature distribution:

$$\mathbf{f}_{\mathrm{th}}(\mathbf{r},t) = \rho\,\beta\,g\,\delta T(\mathbf{r},t)\,\mathbf{u}_z \tag{4.2}$$

where g is the gravity, β the dilatation coefficient of the fluid, $\delta T(\mathbf{r},t) \equiv T(\mathbf{r},t) - T_\infty$ the temperature increase and $\mathbf{u}_z$ the unit vector along z direction (as defined in Figure 4.1). In the Navier-Stokes equation (4.1), the second term represents the acceleration of a fluid particle along a stream line. This term is neglected as inertial forces are small compared to viscous forces on the micro- and nano-scale [109]

considered to not control the physics of temperature-induced fluid convection, as we are in the nano and micro scale. When the system reaches the steady state we can cancel out the time derivatives in equation 4.1 and then the remaining competing forces are the viscosity force and the thermal force. When reaching an equilibrium these should be on the same order of magnitude

$$\eta\nabla^2\mathbf{v}(\mathbf{r},t) \sim \rho\,\beta\,g\,\delta T(\mathbf{r},t) \tag{4.3}$$

Let $\tilde{V}$ be the order of magnitude of the velocity in the fluid, $\tilde{L}$ the characteristic size of the plasmonic structure and T_0 its temperature increase. We obtain

$$\tilde{V} \sim \tilde{L}^2\rho\,\beta\,g\,T_0/\eta \tag{4.4}$$

[2]A discussion of the applicability of fluid properties at the nanoscale is refereed to in chapter 1 section 1.3.

[3]The equation is presented here in a coordinate system fixed in space, referred to as the Eulerian description.

For a $\tilde{L} = 250$ nm large structure (radius of a disk for example) and a temperature increase of $T_0 = 60°$C, and using $\rho = 10^3$ kg/m^3, $\beta = 10^{-4}$ K^{-1}, $\eta = 10^{-3}$ Pa·s and $g = 9.8$ m/s^2, we obtain that the characteristic fluid velocity of the thermal induced convection is $\tilde{V} \sim 10^{-9}$ m/s (this is in good agreement with numerical calculations presented hereafter which give $\tilde{V} \sim 0.5 \times 10^{-9}$ m/s). From this value of fluid velocity, we can work out the value of the Reynolds number defined as

$$\mathsf{Re} = \frac{\tilde{V}\,\tilde{L}}{\nu} = \frac{\beta\, g\, T_0\, \tilde{L}^3}{\nu^2} \tag{4.5}$$

where $\nu = \eta/\rho$ is the kinematic viscosity. A fluid flow associated to small Reynolds number (< 0.1) is governed by viscous forces and is laminar. whereas, high Reynolds numbers are associated to turbulent fluid flows. In our case, $\mathsf{Re} \sim 10^{-8}$ which refers to a highly viscous and laminar fluid motion.

Consequently, similarly to temperature, velocity is also governed by a linear diffusion equation

$$\partial_t \mathbf{v}(\mathbf{r},t) - \nu \nabla^2 \mathbf{v} = \beta\, g\, \delta T(\mathbf{r},t)\, \mathbf{u}_z \tag{4.6}$$

The kinematic viscosity $\nu = \eta/\rho$ has the same dimension as the thermal diffusivity α and equals 0.894 mm^2/s for water. The characteristic time scale associated to the establishment of a velocity profile around an object of characteristic size $\tilde{L}$ is thus

$$\tilde{t}_{\mathbf{v}} = \tilde{L}^2/\nu \tag{4.7}$$

To give some examples, in water, for $\tilde{L} = 10$ nm, 100 nm and 1 µm, we respectively obtain $\tilde{t} = 0.1$ ns, 10 ns and 1 µs. Consequently, the time scales related to the establishment of the temperature profile (as detailed in chapter 1) and velocity profiles are of the same order of magnitude in water for a given structure.

We shall see now if such a characteristic fluid velocity can distort the temperature profile. In the presence of fluid convection, the Laplace equation 1.10 which describes temperature distribution outside the heated structure, is modified

$$\rho\, c_{\mathrm{p}}\, \nabla \cdot (T(\mathbf{r})\, \mathbf{v}(\mathbf{r})) - \kappa\, \nabla^2 T(\mathbf{r}) = 0 \tag{4.8}$$

where c_{p} is the specific heat capacity at constant pressure ($c_{\mathrm{p}} = 4.18 \times 10^3$ J/kg·K for water) and κ is the thermal conductivity. The first term of equation

(4.8) represents heat transport through fluid convection – it is on the order of $\rho\, c_\mathrm{p}\, T_0\, \tilde{V}/\tilde{L}$ – while the second term represents heat transport through heat diffusion – on the order of $\kappa\, T_0/\tilde{L}^2$. The ratio of the orders of magnitude of these two terms gives a dimensionless number – called the Rayleigh number [108] – that describes the ration between heat convection and heat diffusion

$$\mathsf{Ra} \;=\; \frac{\tilde{V}\,\tilde{L}}{\alpha} \;=\; \frac{\beta\, g\, T_0\, \tilde{L}^3}{\alpha\, \nu} \tag{4.9}$$

where $\alpha = \kappa/\rho\, c_\mathrm{p}$ is the thermal diffusivity of the medium. In the present case, $\mathsf{Ra} \sim 10^{-7}$, and so thermal diffusion is dominant over heat convection.

As a consequence, in nano plasmonics experiments occurring in water-like media, the temperature distribution is mainly governed by heat diffusion, and not fluid convection. In other words, on the nanoscale the temperature reaches its steady state distribution so fast that such a slow fluid motion ($\tilde{V} \sim 10^{-8}$ m/s) cannot distort it. The temperature profile around the structure is the same as if the fluid were not moving. This conclusion justifies the treatment of the complex set of coupled equations of Navier Stocks and the heat transport equation (4.1 & 4.8) in two independent steps. First solving equation 4.8 considering no convection, and then inputting the resulting temperature profile in equation 4.1.

4.3 Numerical simulations

Possible numerical approaches

In the system under study, the optical, thermal and hydrodynamic problems are all independent: the inner temperature increase of the nanoparticle has a weak influence on its absorption cross section and, as demonstrated in the previous section, the fluid motion is so slow that it does not affect the steady state temperature distribution. Consequently, we do not need to carry out complex simulations to address the three problems self-consistently. On the contrary, each problem can be addressed separately and successively.

Three possible numerical approaches are commonly used to address photothermal effects associated to plasmonic structures.

The first one is based on a Boundary Element Method (BEM) [110]. This optical method has recently been extended to compute the temperature distribution around isolated complex plasmonic nanoparticles, chain of spherical particles and elongated structures [36]. This approach appears to be time efficient since it is based on a mesh restricted to the interface of the nanoparticle

and can for the same reason address problems with a large amount of particles. While its use is simple when the problem features an axial symmetry, it requires additional efforts for a more general case [111]. Furthermore, it cannot be applied when the surrounding medium is nonuniform (as for a plasmonic structure lying upon a glass substrate for example).

Another numerical approach is based on the use of Green's dyadic tensors and can address as well both the optical and thermal problems associated to plasmonic structures [11, 39]. The mesh is restricted to the plasmonic structure, which makes it more time efficient than finite elements method that additionally mesh the environment, but less time efficient than the BEM method that only meshes the interface. The main advantages of this approach are its capability to deal with complex geometries and account for the presence of a planar substrate.

Another possible approach is a finite element method based on a multidisciplinary commercial software named Comsol [4]. It can simultaneously handle optical, thermal and hydrodynamic processes. However, it requires the meshing of the whole system (nanoparticle and surrounding medium).

For the sake of consistency, we choose in the following to address each processes (optical, thermal and hydrodynamic) using Comsol.

Thermal induced fluid convection - simulating a general case

We consider the simple but general case of a gold disk lying on a glass substrate and immersed in water (Figure 4.1). As a first step, we perform simulations in which the inner temperature of the gold disc T_{disc} is considered as a parameter (a boundary condition). We vary T_{disc} from room temperature (20°C) to the boiling point (100°C). The choice of a uniform temperature over the disk arises from the very short time scale (typically a few ps in nano metallic systems [34]) required to reach such equilibrium compared to the time scales of the physical processes we are interested in.

From an experimental point of view the temperature of a heated structure is easily controlled as it scales linearly with the incoming laser power (as shown in chapter 1 Figure 1.3c). Other parameters that can be varied are the disc height h and diameter d (Figure 4.1). The boundaries of the problem were taken to be open, simulating an endless fluid.

Figure 4.2 addresses the dynamical properties of the thermal induced convection. The inner temperature T_{disc} of the 500 nm disc, applied at time $t = 0$,

[4] Comsol version 4.2 and 4.2a were used

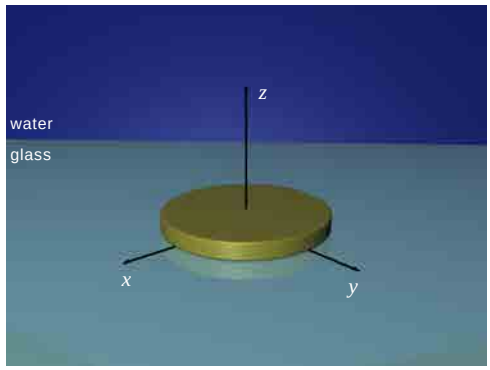

Figure 4.1: ***Geometry of the system investigated.*** *It consists of a gold disc of height h and diameter d lying upon a planar glass substrate and immersed in water. The structure is illuminated from the bottom by a plane wave that undergoes total internal reflection.*

results in a fluid convection around the disc as can be seen in the velocity profiles (Figures 4.2a-c) which is refereed to as a Rayleigh-Benard flow. Two time scales come into play. One $\tilde{t}_T$ related to the establishment of the steady state temperature profile. The other $\tilde{t}_{\mathbf{v}}$ is related to the establishment of the steady state velocity profile. Figures 4.2d-e represent the evolution of the temperature and the velocity of the fluid as function of time. The temperature $T(t, \mathbf{r})$ and the velocity amplitude $v(t, \mathbf{r})$ are measured 250 nm above the structure at $\mathbf{r} = (0, 0, 250)$ nm. An exponential fit of these plots gives $\tilde{t}_{\mathbf{T}} \sim 100$ ns and $\tilde{t}_{\mathbf{v}} \sim 500$ ns, which is in good agreement with the orders of magnitude obtained from dimensional analysis in the previous section.

Figure 4.3 investigates the influence of the disc temperature T_{disc} and the disc diameter d on the velocity field magnitude. Regarding the temperature influence, since all the equations are linear (namely equations (1.5), (4.2), (4.6)), we should obtain a velocity field proportional to the temperature of the gold disc. This reasoning is valid as far as the parameters describing the fluid (κ, α, η, ...) remain constant over the temperature range investigated. Figure 4.3b plots the variation of the average velocity as a function of the temperature when these parameters are constant (dashed line) and vary with temperature (solid line). As expected, in the first case, a perfect linear dependence is obtained while in the second case a slight modification is observed at high temperatures mainly

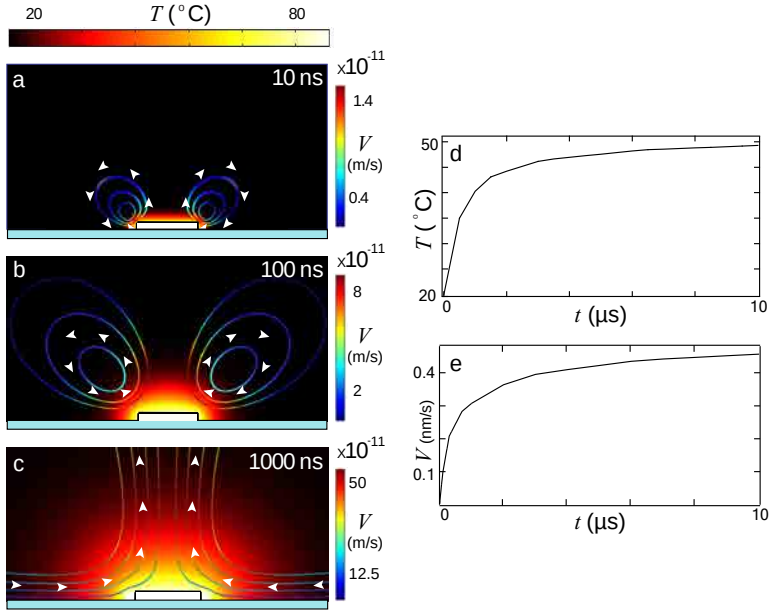

Figure 4.2: ***Temporal study of fluid convection around a gold disc****, of height 40 nm and diameter 500 nm, which is heated at time* $t = 0$ *from room temperature to* $T_{disk} = 80^{\circ}C$ *. a-c) Temperature and velocity patterns (stream lines) at different times. d) Temperature of the liquid as a function of time measured at a point located one radius (*$250nm$*) above the gold disk center. e) Velocity of the liquid as a function of time measured at the same point.*

because the medium becomes less viscous. Note that since the temperature of the structure is proportional to the power of the incoming laser, the magnitude of the velocity field is linear with the laser power. This finding points to the opportunity to remotely gain control over the velocity field around a plasmonic particle by varying the incoming laser power. Regarding the influence of the disc size (Figure 4.3c), the main conclusion is that varying the disk radius has a quadratic effect on the velocity field, as predicted by equation. (4.4).

A conclusion from Figure 4.3 is that nanometric structures (typically of size below 200 nm), even for temperatures close to the boiling point, the fluid velocity hardly overpasses 10 nm/s. As a consequence, any molecular motion will

be mainly driven by Brownian dynamics or thermophoresis. In this case, isolated plasmonic nanoparticles will not be efficient to control micro- and nanofluidics. However, while reaching micrometric structures, faster fluid motion can be achieved (hundreds of nanometers per second), which opens the path for micro-fluidic applications. Efficient optofluidic control could also be achieved with nanometric structures by using arrays and more complex systems of isolated nano particles. This paradigm, which is used in section 4.4 is intrinsically more complicated to design and build, but could allow for more control over optofluidic systems.

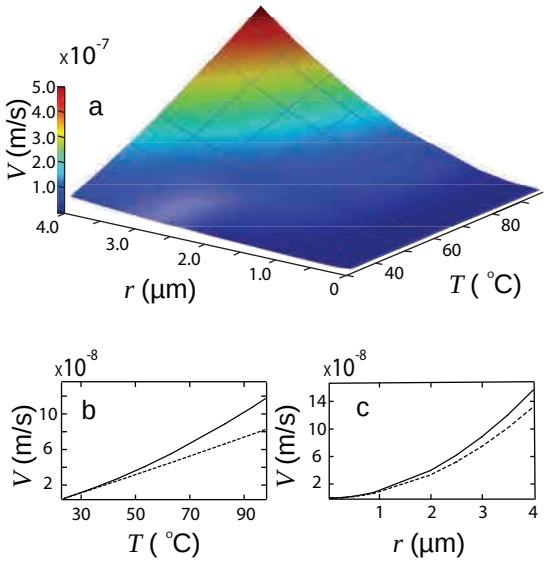

Figure 4.3: ***Influence of the disc temperature and diameter on the velocity magnitude.*** *a) Velocity measured at a point located one diameter above the disk center, as a function of the disc temperature and radius. b) Velocity as a function of the disc temperature for* $r_{disc} = 2\mu m$*. c) Velocity as a function of the disc radius for* $T_{disc} = 50°C$*. (The dashed lines are the results of the calculations when the water coefficients are constant, and do not depend on the temperature).*

After the nano heater configuration is fixed, an experimentally accessible parameter which can control the velocity is the liquid chamber height H. In a

fluidic environment, a top cover slide is usually added to confine the liquid in the z direction. The chamber height can go down to a few micrometers. This dependence was also studied numerically and is presented in Figure 4.4. Below a certain height the velocity field can be damped by more than one order of magnitude. Consequently, the fluid confinement is also a parameter that has to be considered when evaluating the magnitude of plasmonics-assisted fluid convection. When any fluid motion is to be avoided, for instance for optical trapping experiments, the chamber height is a parameter that can be used.

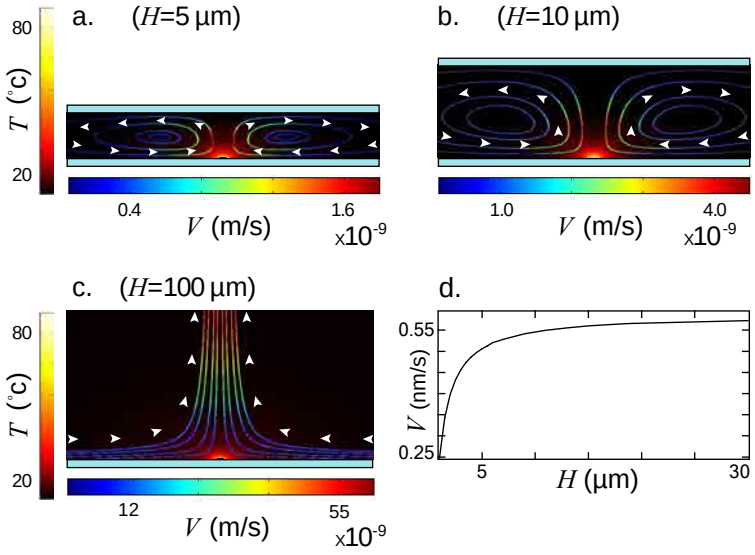

Figure 4.4: ***Investigation of the influence of the chamber height on thermally induced fluid motion in plasmonic trapping experiments.*** *a-c) Velocity fields for various chamber heights H, induced by a gold disc of diameter 500 nm heated to $T_{disk} = 80°C$. d) Velocity as a function of H, measured at one radius (250 nm) above the center of the disc.*

Fluid motion induced by plasmonic heating in a trapping experiment

It has recently been proposed to used a surface patterned with plasmonic micro- and nano-structures to trap tiny objects [107, 112]. Under illumination, plasmonic structures are surrounded by a large electric field gradient that creates a stable potential well for a wide range of micro and nano-objects. When this kind of trap was reported [107], it was evoked that fluid convection due to heating of the plasmonic structure could *a priori* play a role in the trapping process without being able to quantify the actual temperature or fluid velocity. In this last part, we address the matter of the contribution of thermal induced fluid motion in plasmonic trapping experiments. The main question is to figure out whether the centripetal velocity field observed in the previous paragraph is strong enough to play a role in the trapping process as compared to optical forces.

In this work we performed simulations using typical parameters used by righini et al. [107] namely, gold discs of 2 µm in diameter and 40 nm in height. Laser power of 100 mW focused to a circle with radius 25 µm (5×10^{-2} mW/µm^2) illuminated under surface plasmon resonance conditions (incident angle of 68°, measured from the -z axis). The trapping discs were immersed in a water chamber of height 10 µm. In these conditions, we find that the disc temperature increase equals about 6°C and the maximum velocity equals 1 nm/s. This velocity is negligible and corroborates the all-optical origin of the trapping effect mentioned above. Indeed, if we calculate the force that a velocity field would inflict on a particle with a characteristic radius of 1.5 µm, using Stockes drag formula for a sphere, we get: 3×10^{-17} N which is two orders of magnitude lower than the force typically achievable in optical trapping force, as reported in [113].

Another phenomenon that could *a priori* come into play is the Soret effect also called thermophoresis [114]. This phenomenon happens when an object (molecule or particle) immersed in a liquid is subject to a temperature gradient. It usually yields a motion from hot to cold places but the effect can reverse for very small objects (molecules) and low temperatures (a few degrees). In the present case, given the size of the object and the temperature range, any thermophoresis contribution should push the beads from hot to cold places. Consequently, thermophoresis cannot contribute to any trapping process in the above mentioned experiment.

4.4 Application - optofluidic pump

Numerical simulations

Based on the principles we have derived in the previous sections we went a step towards a concrete application and made a real application based on plasmon assisted optofluidics. The aim is to generate directional fluid movement within a microfluidic environment. Microfluidics is a widely studied field [109, 115]. In analogy to microfabricated integrated circuits which revolutionized computation, microfluidics hopes to revolutionize chemistry and biology by automation of experiments while using minimal amounts of reagents [116]. In most applications there is a need to move liquids inside a microfluidic chip. Here we propose to harness energy coming from a laser to generate this flow. Indeed, the strategy of combining microfluidics and optics concurs with a widespread promising trend as reported by Psaltis et al. [117].

To generate a directional flow, we introduce an asymmetry into the system. This asymmetry can emanate either from heating the system in an unbalanced way (heating one side), or by making asymmetric boundaries for the liquid. In practice, we first modeled various designs for such a system in a 2D configuration. A scheme is presented in Figure 4.5a. We position plasmonic particles on a glass substrate, and build a chamber which is fulled with water. The chamber has two openings that serve as an inlet and outlet. Depending on which side of the chamber is heated, the flow is driven in opposite directions. A simulation of this system is presented in Figure 4.5b. The simulation is performed as before, using the Boussinesq approximation, setting the temperature of the plasmonic structures, and allowing open boundaries for the liquid inlet and outlet. The red arrows indicate the velocity vectors of the fluid, and indeed a directional flow is evidenced.

Using the methodology and physical insight gained by the 2D simulations, we went on to perform a full 3D simulation. A characteristic result is presented in Figure 4.6a. Structures are heated on one side of the liquid chamber. An open boundary is defined on both sides of the volume, and all the volume is filled with water. As expected, when heating one side, a directional flow is generated. In this case the flow dynamics are more complicated as is illustrated by the pathlines (the trajectory of a fluid particle) presented in Figure 4.6a (green line). The red arrows represent the velocity vectors and show a resulting directional flow.

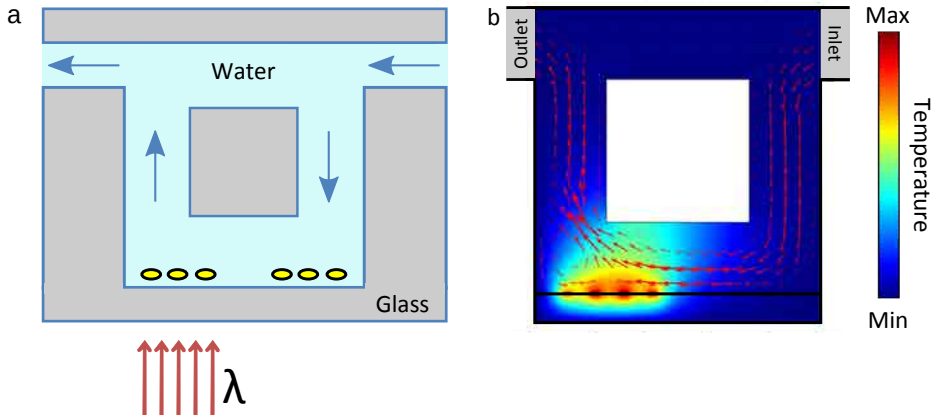

Figure 4.5: ***2D microfulidic pump.*** *a) Scheme of a 2D pump. Yellow circles represent GNRs placed on a glass substrate. Water is represented in the light blue color. There are two open boundaries on the top side of the chamber. When a laser is directed to one side of the chamber it heats the GNRs and generates a directional flow. b)2D comsol simulation. Red arrows represent velocity vectors.*

Experimental implementation

Based on the 3D simulation, a microfluidic chip was designed and fabricated[5]. The fabrication was performed using standard microfluidic methods as was summarized by Xia et al. [118]. In brief, the fabrication consists of the following steps:

i Design and fabrication of optical lithography mask.

ii Preparation of a silicon wafer mold: transferring the lithography mask using UV-lithography. The mold is made in SU8 photoresist. The height of the photoresist controls the height of the microfluidic channels.

iii PDMS casting: the prepolymer PDMS is poured on top of the silicon wafer mold, and cross-linked (solidified), by a heating process.

[5]I performed the fabrication based on knowledge accumulated in the PNO group at ICFO, mainly by Dr. S. Acimovic.

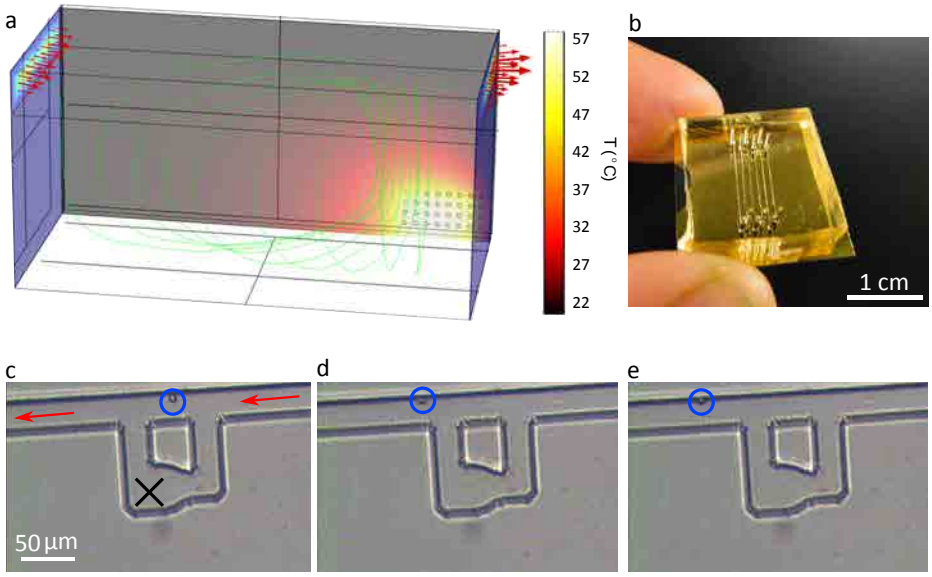

Figure 4.6: ***Microfluidic pump: simulation, fabrication and proof of concept.*** *a) 3D simulation of a microfluidic pump. Heated structures are placed on the lower right hand side of the back wall. Red arrows represent the fluid velocity vectors, at the inlet and outlet of the chamber (all other boundaries are sealed walls). A green line represents a pathline starting at the input. b) Microfluidic chip made of PDMS with six channels. In each channel there are many pump chambers. The drilled channel inlets and outlets can be seen. The glass substrate is coated with a gold film, and was used for primary testing. In subsequent chips the substrate is pattered with GNRs and is aligned to the PDMS chip as explained in the text. I present this primary chip as the gold adds contrast to the image. c-e) Three frames from a video that show the directional flow of a silicone bead induced when shining a laser on the microfluidic chamber. The laser of 50 mW is focused to a 10 µm diameter spot. The focus location is marked by the black cross . The silicon beads, used to track the flow, are marked by a blue circle. The direction of the flow is depicted in c) with the red arrows.*

iv Bonding to substrate: The solid PDMS chip is bonded to the substrate which was pre-patterned with plasmonic structures using e-beam lithography. This is performed by thermal bonding. This step requires alignment

of the structures on the substrate to the PDMS chip.

v Drilling of inlets and outlets to the microfluidic channels.

An example of a fabricated chip is presented in Figure 4.6b. In this case six different channels were fabricated, each having various designs of pump chambers. The various designs are used for optimization of numerous parameters such as size of inlets, width of chamber, etc. We pattern Gold Nanorods (GNR) arrays on a glass substrate to match the locations of the pumps. We attach the substrate to the PDMS chip using alignment marks so that the GNR arrays reside below the pump chambers. Similar chips were built with different PDMS channel heights ranging from 5-50 µm. We present in Figures 4.6c-e results obtained on a single pump chamber with a channel height of 30 µm. In this case the glass substrate which seals the PDMS chip is patterned with GNRs . The channel is filled with water mixed with micrometric silicon beads. After the system has reached equilibrium, and the beads do not move, we shine a laser with a power of P=100 mW on the GNRs, to a location marked by the black cross in Figure 4.6c. The laser induces a directional flow. We can see this flow by looking at the movement of the beads in Figures 4.6d,e which are taken 7 and 14 video frames after the one in Figure 4.6c. The video frame rate is 27 frames/sec. This means that the bead is moving at a velocity of about 100 µm/s. This velocity is surprisingly higher than expected from simulations. One possible explanation is that in the experiment much more particles were heated than in the simulations. Another possible explanation is that the temperature generated by the plasmonic structures could be much higher than 100 °C. This point was evidenced by the fact that we sometimes observed that the GNRs melted, which occurs at temperatures higher than 500 °C [119]. This concept concurs with the observation recently made in the Richardson group who report on water superheating around a gold NP up to almost 600K without bubble formation [120]. Another unanticipated point was that after switching off the laser there was a recoil of the flow (and the bead), we believe this happens due a build up of pressure due to the long microfluidic channels (which are on the scale of a few cm). No full rigorous study of the efficiency and characteristics of this 3D pump are given here, and this work can be seen as a proof of concept.

4.5 Summary

To summarize, by systematic dimensional analysis and by numerical computations using Comsol, we have investigated the physics of fluid convection induced by heat release from plasmonic particles. We evidenced a laminar regime

and a Rayleigh-Benard-like fluid convection. The characteristic orders of magnitude of temperature, time and velocity have been derived as a function of the size of the structure and the laser irradiance. Transient evolutions last from ns − µs depending on the size of the structure but not on the temperature increase. We have shown that the thermal and hydrodynamic problems are not self-consistent and can be treated independently due to a low Rayleigh number. For isolated nanometric structures (below 200 nm) the Reynolds number is so low that even for temperatures close to the boiling point, any plasmonics-assisted fluid motion hardly overpasses 10 nm/s. To reach a few hundreds of nanometers per second and open the path for micro- and nano-fluidics applications, either larger structures (>500 nm), or heating of multiple structures should be considered. These basic principles were built on to generate an application, in the form of an optofluidic pump. This application is based on heating plasmonic particles inside a microfluidic environment. This paradigm was simulated first in a 2D and then a 3D geometry. From the insight gained by the simulations, a PDMS microfluidic chip was designed and fabricated. Different parameters were tested including: channel height, pump inlet/outlet sizes, and different pump shapes. We showed a proof of concept for a specific design, where a strong directional fluid flow is remotely induced by irradiating with a laser. We hope that this primary result may stimulate interest and generate more work in this direction.

5

In vitro temperature mapping using GFP

5.1 Introduction

Heat is of fundamental importance in many cellular processes such as cell metabolism, cell division and gene expression [55, 56, 57]. Accurate and non-invasive monitoring of temperature changes in individual cells could thus help to clarify intricate cellular processes and develop new applications in biology and medicine.

In this chapter we show that Green Fluorescent Protein (GFP) can be used as a thermal nanoprobe suited for *in vitro* cellular temperature mapping. Temperature probing is achieved by monitoring the Fluorescence Polarization Anisotropy (FPA) of GFP. We first demonstrate the possibility to use GFP as a nano temperature probe in an aqueous environment. To this end, a calibration curve relating FPA of the GFP to temperature is performed. We then apply this to measure the temperature around a heated gold micrometric structure. subsequently, the method is applied to GFP-transfected HeLa and U-87 MG cancer cell lines. We perform an intracellular calibration curve and measure the temperature raise due to photothermal heating of Gold Nanorods (GNR) both inside and out of the cell.

In general, a spatial resolution of 300 nm (diffraction limit) and a temperature accuracy of about 0.4 °C are achieved. Benefiting from its full compatibility with widely used GFP-transfected cells [121], this approach provides a non-invasive tool for fundamental and applied research in areas ranging from

molecular biology to therapeutic and diagnostic studies.

5.2 State of the art

Many techniques have recently been proposed to address the need for monitoring intracellular temperature in molecular biology. In fact since 1995 when the first cellular temperature probe was reported [122] a plethora of new methods have been developed. A comprehensive comparison of these has been performed in different review articles [50, 51]. Here we highlight the relevant ones in the context of intracellular imaging. Most of these approaches rely on introducing synthetic nano-objects into living cells such as quantum dots [79, 80], nanogels [123], nanoparticles [124, 125, 126] or thermosensitive dyes [127] whose fluorescence properties (intensity or spectrum) depend on temperature. However, such techniques suffer from some limitations. Approaches based on fluorescence intensity measurements lack reliability since fluorescence intensity is dependent on many other factors such as molecular concentration, migration, bleaching and illumination intensity. Also, techniques based on spectral fluorescence measurements are usually slow as they require significant integration times. Incidentally, this second approach generally results in a single-point temperature measurement and not in real-time temperature imaging. Independently of these issues of reliability and slow read-out, introducing artificial probes within cells may alter their behavior or integrity. An alternative approach which relies on genetic engineering was recently reported. Here E. coli bacteria is transfected with a temperature sensitive vector[1] which increases quantities of β-galactosidase (a hydrolase enzyme) in response to a temperature increment [128]. The heating of individual bacteria was monitored via an increase of the lacZ[2] gene expression. However, such an approach is slow for real-time measurement and does not permit dynamic temperature monitoring because of its non-reversibility. Another approach uses a sub-micrometer thermocouple that is inserted into the cytoplasm of the cell [66]. This technique enables time-resolved measurement of changes in the cytoplasm temperature with high temperature resolution. However, the introduction of a physical object through the plasma membrane may compromise the cells integrity and is incompatible with imaging. Another strategy is based on inserting Nitrogen Vacancy (NV) centers into cells [24] and then applying a specific pulse train of electromagnetic waves at optical and radio fre-

[1] A vector is a DNA molecule used as a vehicle to artificially carry foreign genetic material into a cell where it can be replicated and/or expressed.

[2] The lac operon is a functioning unit required for the transport and metabolism of lactose in Escherichia coli. lacZ is one of its structural genes.

quencies, by performing fluorescence readout very high accuracy temperature measurements can be made (2mK accuracy, when integrating over 30 s). A drawback of this method is that it is probably complex and the usage of NV centers is not yet accepted among biologists. Also this technique can only be used to obtain the temperature in a given location and does not give a full temperature map. In another context, a pertinent approach for cellular thermal imaging was presented by using photoacoustic microscopy [75, 76]. This method holds much promise due to the potential lack of sample preparation prior to the imaging. The drawback is that this kind of measurement is not absolute in the sense that a reference measurement is always needed (as what is measured is a change in signal). Another recent and noteworthy temperature imaging approach is based on measuring the lifetime of a fluorescent complex [84, 129]. Indeed, Okabe et al. [84] built a carefully engineered polymer complex whose fluorescence lifetime (as well as intensity) varies with temperature. An accuracy of up to 0.18 °C was reported, which was enough to observe a higher temperature in the cell's nucleus and centrosome compared to the cytoplasm, and this temperature gap depended on the cell cycle.

5.3 Temperature mapping using GFP

The present work is motivated to overcome the limitations of the existing approaches by developing a temperature imaging technique that combines full bio-compatibility with high resolution and fast read-out. Another aim is to maintain the measurement relatively simple and accessible to biologists. To this end, we demonstrate how GFP can be used as an efficient temperature nanoprobe by measuring its FPA. GFP is already a widely used contrast agent in biology [130] [3]. Indeed, this protein has become one of the most important tools in modern life science. Several features explain the widespread use of GFP: (i) GFP can be expressed in many living organisms by genetic engineering making it a natural and non-invasive marker for in vivo applications [121] (ii) over the last 15 years many GFP derivatives have been engineered so that they span the entire visible spectrum and have high quantum efficiency [131] (iii) GFP has been extensively researched and found useful for many applications as markers for gene expression, protein localization and folding, as a Ca^{2+} ion or pH-sensor, redox-sensitive indicator and as probes for protein-protein interactions [132, 133, 134]. Following this trend, we here propose to use GFP as a temperature sensor

[3] The discovery and development of GFP were awarded the Nobel Prize of chemistry in 2008. It was jointly awarded to Osamu Shimomura, Martin Chalfie, and Roger Y. Tsien *"For the discovery and development of the green fluorescent protein, GFP"*.

through FPA measurements.

The underlying physics relating temperature and molecular FPA is well established and was already explained in chapter 2. In that case thermal imaging is performed by monitoring the FPA of Fluorescine in a glycerol:water (4:1) mixture. The viscosity of the mixture is increased by adding glycerol, which reduces the rotational velocity of the fluorophores so that $\tau_R \approx \tau_F$, a prerequisite for a sensitive FPA measurement. Such an approach is not compatible with biological systems due to toxicity of the glycerol. In general, it is desired to not change the viscosity of the biological system. In this work we approach the condition $\tau_R \approx \tau_F$ by increasing the hydrodynamic volume V of the fluorophore and do not alter the system's viscosity. The characteristic size of GFP is 3.5 nm [135]. By coincidence, such a large protein leads to a rotational correlation time $\tau_R = 4.1$ ns in water, which is on the order of magnitude of its fluorescence lifetime $\tau_F = 2.5$ ns. This fluorescence lifetime was experimentally verified and is presented in Figure 5.1b [4]. The theoretical and experimental temperature dependence of the FPA of GFP in Phosphate Buffer Saline (PBS) solution, pH=7.4 is presented in Figure 5.1c , for temperatures between 20 °C and 60 °C [5]. This calibration curve is performed both for heating the system and cooling, verifying the reversibility of the FPA for GFP. Due to varying pH levels found in biological organisms the experiment was reproduced at pH=6.0 (Figure 5.1d) covering the typical range experienced within a cellular environment. The FPA variation over this temperature range is about 0.001 per degree Celsius. The theoretical fit was performed from equations (2.1) to (2.3), using fluorescence lifetime $\tau_F = 2.5$ ns [137], hydrodynamic volume $V_{GFP} = 17.2$ nm^3 [138] and limiting anisotropy $r_0 = 0.31$ extracted from the fitting procedure.

5.4 Experimental results

Temperature around a gold microdisc

To begin with, we chose to illustrate GFP-based thermal imaging on a model system consisting of a gold microdisc (2 µm in diameter and 40 nm thick, see Figure 5.1e for the SEM image) prepared by standard e-beam lithography. The disc lies on a glass substrate and is surrounded by a PBS solution containing GFP molecules (3×10^{-5} Molar).
The disc is placed in the sample plane of a confocal optical microscope (see

[4] Measurement performed with a time-correlated single photon counting device: Picoquant, PicoHarp 300.

[5] $\approx$ 76 °C being the denaturation temperature of GFP [136].

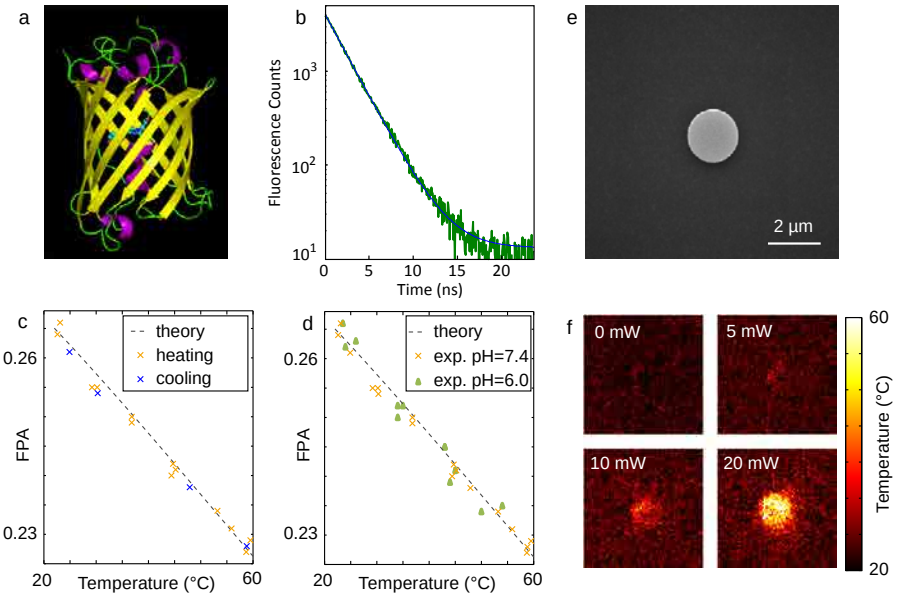

Figure 5.1: ***Measuring temperature using GFP.*** *a) 3D representation of the structure of GFP. Note the chromophore inside the barrel structure (known as a beta barrel). b) Fluorescence lifetime of GFP. In green is experimental data and in blue a one exponent fit. the fit gives a fluorescence lifetime of* $\tau_F = 2.49$ *ns. c) Calibration curve that relates between FPA of GFP and temperature in PBS. Measurements are taken both while heating the system and cooling it (in yellow and blue, respectively). Theoretical model represented in the broken line. d) Calibration curve relating FPA of GFP to temperature in PBS for different pH conditions. e) Scanning electron microscope image of a lithographically imprinted gold microdisc. f) Temperature map obtained around the microdisc while heating using an infrared laser at various powers.*

chapter 2) operated with two laser sources: a heating IR laser[6] and a blue 473 nm laser for GFP excitation. An expected decrease of the FPA was observed around the structure while heating (*i.e.* during IR illumination). The associated temperature map obtained using the calibration curve in Figure 5.1c is presented in Figure 5.1f for different heating powers. The temperature increase is proportional to the power of the heating IR laser and a temperature increase as small as 0.4 °C can be detected. This value was established by calculating the standard deviation of the data.

Intracellular calibration curve

We now present temperature measurements performed on single living cells. We chose to work with transfected HeLa and U-87 MG cancer cells in which GFP was over-expressed[7]. Using transfected cells ensures that GFP occupies the entire cell volume. The temperature is processed from the FPA using the same procedure as in the case of GFP in PBS. However, the calibration curve

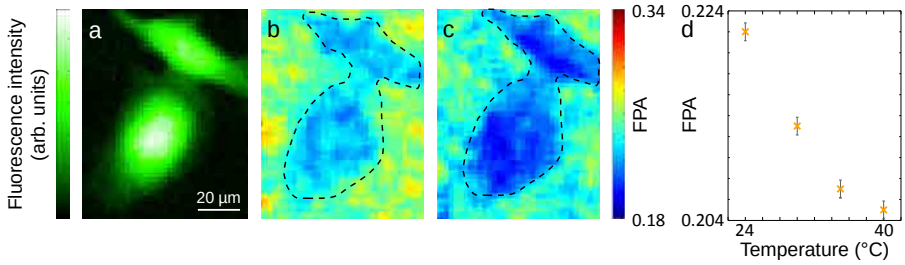

Figure 5.2: ***Intracellular calibration curve for HeLa cancer cells.*** *a) Intensity of fluorescence of GFP transfected HeLa cells excited with a blue laser. b) FPA measured at $T_0 = 23°C$. c) FPA at $T_0 = 40°C$. d) Calibration curve that relates the measured FPA of the intracellular GFP with temperature.*

relating temperature with FPA inside cells is different, since the intracellular viscosity differs from the viscosity of PBS. In order to obtain a new calibration curve, a resistive heating of the sample chamber was performed while recording the FPA from inside transfected HeLa cells as a function of the chamber temperature, T_0. The calibration curve is presented in Figure 5.2d. FPA images

[6] Ti:sapphire (Coherent, mira 900), and its wavelength set to $\lambda = 780$ nm, CW.

[7] Cell transfection was performed by Dr. Sebastian Thompson, a post-doc in the PNO group.

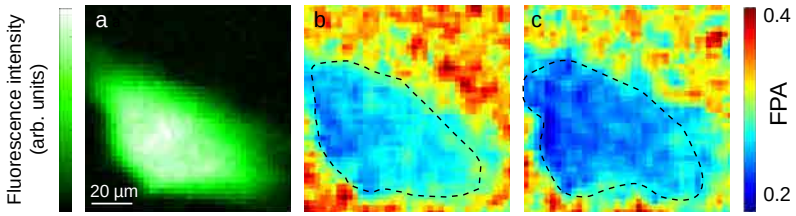

Figure 5.3: ***FPA measurements in U-87 MG cells while heating.*** *a) Intensity of fluorescence of GFP transfected U-87 MG cells excited with a blue laser. b) FPA map while not heating. c) FPA map while heating the system.*

for $T_0 = 23\,^{\circ}C$ and $T_0 = 40\,^{\circ}C$ are shown in Figure 5.2b and Figure 5.2c. The scan is performed with a collection time of 20 ms per pixel, and the entire image takes about 1 min to record. Interestingly, the FPA map inside the cell is almost uniform although the intensity map (Figure 5.2a) is not. The intensity map is not uniform due to a non homogeneous distribution of GFP in the different organelles. This observation illustrates the fact that FPA is not dependent on fluorescence intensity and so the variation in intensity does not affect the FPA map. One factor that would affect the FPA map would be if there were a spatial variation in intracellular viscosity. It has been reported in the literature [139] that when a free (intracellular) probe of the size of GFP is in a cellular environment, it experiences a nano-viscosity (compared to a macro-viscosity) which is homogeneous and is not affected by the larger organelles or macromolecules inside the cell. The crossover from nano- to macro- viscosity typically occurs when the probe size reaches tens of nm (for example 80 nm in HeLa cells [139]). As such, a probe of the size of the GFP is expected to see a uniform viscosity in the cell. This explains the uniformity of the FPA inside the cell as seen in 5.2b,c. Such behavior had previously been reported [140]: *"particle rotation is relatively unhindered when particle size is smaller than the spacing between obstacles"*. In practice this permits the local FPA to be translated into the local temperature in a reliable way, and when the temperature changes, the FPA reading will change according to the local temperature (and not depend on the change of the local macro-viscosity).

To verify that the FPA changes with raising temperature in a second cell line, GFP transfected U-87 MG cancer cells were cultured. Again, the cells were imaged using a confocal microscope, and the FPA recorded at room temperature

and at an elevated temperature. The results of this experiment are presented in Figure 5.3. The important characteristics mentioned about the previous case are repeated namely: (i) the intensity image (Figure 5.3a) is non uniform while the FPA image is (5.3b) (ii) the FPA goes down as we increase temperature. Fulfilling these characteristics implies that the method can be applied to this as well as other cell lines.

Intracellular temperature measurement

After obtaining the intracellular calibration curve associated with HeLa cells (Figure 5.2d), we performed an experiment in which we heated GNRs dispersed in the extracellular medium by shining an IR laser (Figure 5.5). Using GNRs as nanosources of heat has many advantages compared to a global resistive heating of the chamber: i) it allows for local delivery of heat, which is fundamentally the best approach to investigate thermal biology at a scale down to the single cell level, ii) temperature variations can be fast and as brief as a few microseconds due to the weak thermal inertia of the small heated volume, iii) using GNR matches the approach already considered in the fields of photothermal cancer

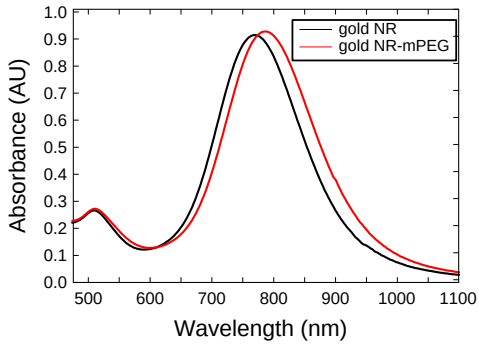

Figure 5.4: ***Absorption spectra of GNR*** *in PBS-CTAB (black) and after ligand exchange process with methoxy-PEG-thiol (mPEG) coating (red). When the mPEG is added a small red shift is observed which verifies that the material surrounding the GNRs was changed.*

therapy [60, 102, 141] or drug delivery [61, 62, 63].

The GNRs that were used for heating, were synthesized using a seed-mediated, surfactant-assisted growth method in a two-step procedure described by Nikoobahkt et al. [46][8]. In order to render the GNRs non toxic a ligand exchange of the

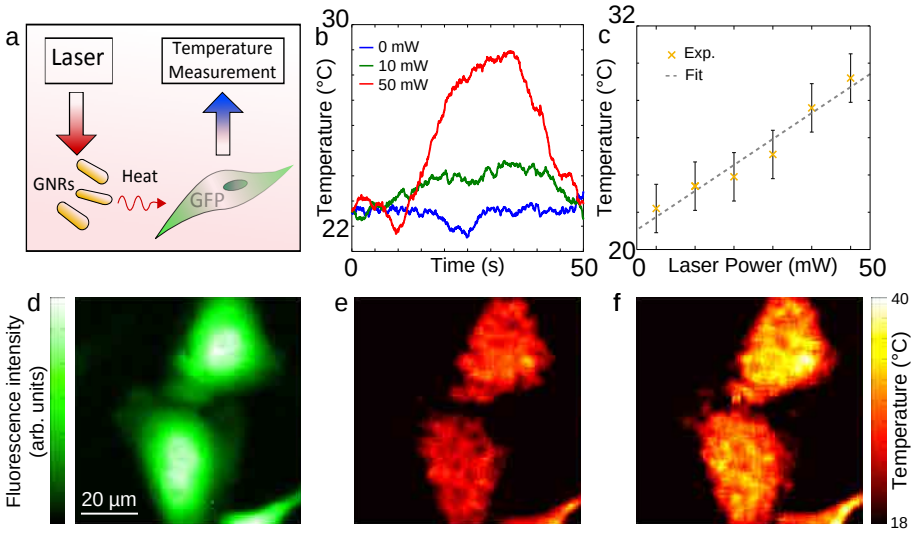

Figure 5.5: ***Temperature measurements in HeLa cells while delivering local heat via photoheating of suspended GNRs.*** *a) Sketch of the system, comprised of: a NIR laser heating GNRs that are dispersed in the extracellular medium. The heat diffuses and heats up the cells, and the temperature is detected via the FPA of the GFP that is inside the transfected cells. b) Temperature variation of a point within the cell as function of time for different powers. c) Temperature of a point within a cell for different laser heating powers shows an expected linear dependence. d) Fluorescence intensity of GFP transfected HeLa cells. e) Temperature map while not heating. f) Temperature map while heating the NR with a focused infrared laser with a power of* $P = 50\ mW$ *(*$1.5 \cdot 10^3\ kW/cm^2$ *at the focal plane).*

hexadecylcetyltrimethylammonium bromide (CTAB) was performed, and the GNRs are incubated with methoxy-PEG-thiol molecule (MW 5000) that exchanges with the CTAB bilayer. This ligand exchange leads to a spectral shift of the SPR, which can be monitored by Vis-NIR spectroscopy as shown in Fig-

[8]GNRs were synthesized by Dr. Mark Kreuzer.

ure 5.4. This shift ensures the stability and integrity of the process. After this step was performed, the PBS buffer was changed to cellular medium, and the GNRs could be used with cells without harming them.

We locally heated the cells by focusing the IR laser 50 µm aside from the studied cell. In this work, we chose not to shine the heating laser on the cell directly, to demonstrate that FPA variations measured in the cytosol are unambiguously due to temperature variations and not to a possible IR-assisted perturbation of the GFP fluorescence emission process. Temperature maps without and with heating are presented in Figure 5.5e and 5.5f respectively. A temperature increase of around 8 °C is observed for a CW laser with a power of 50 mW focused over an area of about 1 μm in radius (giving a power density of $1.5 \cdot 10^3$ kW/cm^2 at the focal plane).

For many applications the temporal evolution during the cell metabolism is of pivotal interest. In Figure 5.5b, the temperature was measured in a fixed position and recorded as a function of time for different heating powers. The temperature rises after the laser is turned on and falls as it is switched off. In this measurement, the data were collected with a time resolution of 20 ms. Furthermore the temperature rises linearly with the intensity of the heating laser as observed in Figure 5.5c.

Measuring secondary heating for photothermal therapy

In the previous section we measured the temperature of a heated cell. In photothermal therapy malignant cells are specifically decorated with GNPs and selectively heated. An important parameter is the temperature rise of the heated cell's surroundings (called secondary heating). To this end we adopt a different approach whereby we first load the cells with GNRs and then shine a laser to heat the cell (as would be done in photothermal cancer therapy). To permit temperature mapping, GFP is added to the surrounding medium (see sketch in Figure 5.7a).

Cells are loaded with GNRs at different concentrations[9]: 1:10, 1:100, 1:1000 (for a mother concentration of $10^{12}\ GNR/cm^3$). The internalization of GNRs by the cell is monitored using Two Photon induced Luminescence (TPL) microscopy as is used elsewhere in literature [142][10]. Upon pulsed illumination, the TPL signal from the GNRs enables us to assess their concentration and distribu-

[9]The concentrations are of GNRs in a standard mixture of PBS and cellular media. The loading of cells with GNRs was performed by Dr. Sebastian Thopmson.

[10]The TPL is induced by using a pulsed Ti:Saphire laser which generates pulses of about 180 fs.

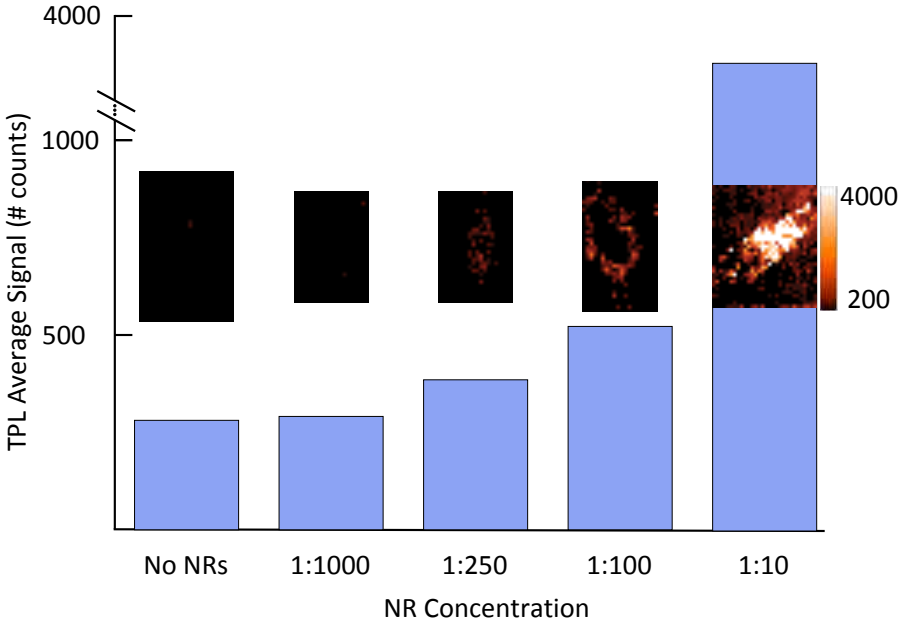

Figure 5.6: ***Monitoring of GNR uptake in HeLa cells using TPL microscopy.*** *The graph shows the TPL signal versus the concentration of GNRs. Each bar is the average TPL signal of about ten cells. The images show an example of a TPL scan, while maintaining all the scale bars equal.*

tion within the cell. In Figure 5.6 we see an increase of one order of magnitude in the TPL signal when the cell is incubated in the highest concentration of GNRs. The GNR uptake is linear with the change of GNR concentration. To allow (or greatly enhance) GNR uptake, serum was removed from the cellular media. The latter is usually present and serves as a source of the cellular nutrients. The many proteins in the serum are known to stick to the GNRs and can inhibit most of the GNR uptake. Cells can live without the serum for well over 24 hours, which was the incubation time.

After optimizing the loading of the cells with GNRs, these were used as photothermal agents when illuminated with a NIR laser. As a first step we repeated incubation of the cells with GNRs at a concentration of 1:10 as explained above. We then performed a TPL scan (Figure 5.7c) on the cell to assure GNR inter-

nalization. Then the loaded cell was illuminated with the NIR laser to raise the temperature. Using GFP as nanothermometers, we monitored the temperature increase around the cell for different cases: no heating and heating with powers of P=100mW and P=200mW. The corresponding temperature maps are presented in Figure 5.7d, 5.7e and 5.7f respectively.

Although the cell is highly loaded with GNRs (as evidenced by the counts of the TPL), the temperature raise is probably not enough to kill the surrounding cells ($\Delta T \approx 10\,^{\circ}\mathrm{C}$) despite the relatively high illumination power (P=200mW, power density of 250 $\mathrm{kW/cm^2}$). This is in accordance with previous publications [143] which report that when heating a single cell it is difficult to generate a large raise in temperature. To further raise the temperature one could increase

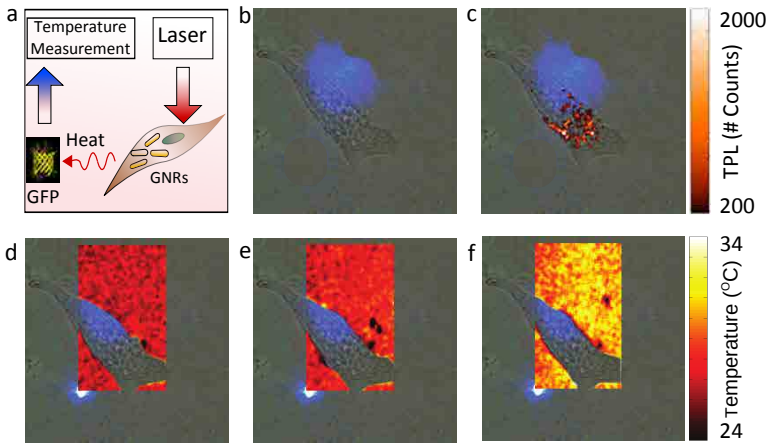

Figure 5.7: ***Temperature measurement in the surroundings of GNR loaded cells.*** *a) Sketch of system. GNR loaded cells are shinned on with a NIR laser. The GNR serve as efficient photothermal converting agents. The heat diffuses to the cells surrounding media in which there is free GFP. the temperature is monitored by measuring the FPA of this GFP. b)Bright Field (BF) image of the cell. c) BF overlapped with TPL signal which is generated by GNRs. d-f) Temperature mappings of the cell's surrounding when illuminated with a 800nm laser at powers of P=0, P=100mW and P=200mW. The blue focus spot is the blue laser which is scanned over the surrounding of the cell. (There is no signal from the cell because it has no GFP inside)*

.

the incoming NIR laser power. Nevertheless, this approach may not be suitable for bio-applications as it may result in absorption of non GNR loaded tissue and result in unwanted heating and tissue damage. Another possibility is to heat more GNR loaded cells. The physics behind this point was explained in a generic system consisting of heating of an ensemble of gold Nano Particles (NP) in a study made by Govorov et al. [144] and later addressed by Baffou et al. [98]. The temperature raise follows a general trend which reads

$$\Delta T_0 \approx \Delta T_{max,0} \frac{R_{NP} N^{m-1/m}}{\Delta} \tag{5.1}$$

where ΔT_0 is the temperature raise, N is the number of NPs and Δ the spacing between NPs, R_{NP} is the radius and m the dimensionality (2 or 3 for 2D or 3D). Applying this formula to the photothermal case dictates that at a given laser power an increase of the temperature to enable killing of cells, requires either heating of a larger number of cells (increasing N), or an increase of the GNR loading, thus decreasing the spacing between the GNRs (decreasing Δ).

5.5 Summary and outlook

In this chapter I presented an approach to measure temperature using FPA of GFP. The presented method combines the advantages of high spatial resolution and good temperature accuracy with high biological compatibility and fast readout. Based on these unique advantages it has the potential to become a powerful tool to unravel intimate cellular processes that involve heating at the single cell level. Moreover, we foresee various natural extensions of the method that will further expand its capabilities. Customization of the method for a specific system could be achieved by using a GFP derivative that absorbs light and fluoresces at a different spectral range. This method can be used in conjunction with the plethora of already developed techniques that use GFP fluorescence allowing two or more simultaneous measurements such as measuring temperature and pH at the same time. Higher temperature sensitivity can be achieved by engineering the properties of the fluorescent protein (modifying either fluorescence lifetime or hydrodynamic volume) resulting in τ_R closer to τ_F. An example in this direction is given in the next chapter where by increasing the hydrodynamic volume we improve the temperature sensitivity.

6

Temperature imaging in a live organism

6.1 Introduction

Controlling and monitoring temperature at the single cell level has become pivotal in biology and medicine. Indeed, temperature influences many intracellular processes [55, 145] and is also involved as an activator in novel therapies [146, 147, 148]. In this context, several approaches have recently been proposed to probe cell temperature *in vitro* None of them have so far been extended to map intracellular temperature in a living organism. Here we present the first *in vivo* intracellular temperature imaging. Our technique relies on measuring the Fluorescence Polarization Anisotropy (FPA) of Green Fluorescent Protein (GFP). We demonstrate fast and non-invasive monitoring of sub-degree temperature change on a single neuron in GFP expressing neurons in *Caenorhabditis elegans* (*C. elegans*). The temperature increase is induced by local photo-heating of Gold Nanorods (GNRs). This simple and biocompatible technique is envisioned to benefit several fields including hyperthermia treatment, selective drug delivery, thermal regulation of gene expression and neuron laser ablation.

6.2 Context

Heat is of fundamental importance in all cellular processes, mechanics and bio-reactions [55, 145, 149]. The intracellular temperature changes, that follow the absorption and release of heat, can be divided into two groups. The cell's

activity induces a temperature change or the intracellular temperature is modified because external heat is provided to reach a desired cellular response. In both cases, obtaining an intracellular temperature map could reveal relevant information, especially if this could be done in the natural environment of the cell. Fields which would greatly benefit from this information include hyperthermia therapy [58], photothermal therapy [59, 60], selective drug delivery using thermo sensitive liposoms [61, 62] or nanoparticles [63], gene regulation driven by heat shock protein promoters [55]. In the field of hyperthermia therapy the temperature of tumor-loaded tissue is raised either to cause cell death or to increase the efficiency of conventional treatment such as radiotherapy or chemotherapy [150]. These therapies involve non-trivial heating processes. Not only must the procedure adequately damage malignant tissue, but also the surrounding normal tissue should be unharmed. This becomes quite challenging, as the thermal characteristics of the tissue change during the heating process. Furthermore, when heating with the aid of artificial thermal agents, the temperature increase strongly depends on the density of these agents, which is usually hard to control and leads to inhomogeneous heating distributions. Therefore real-time temperature mapping is necessary to overcome these problems by serving as an input to a feedback loop of the heating process. Currently Magnetic Resonance Imaging (MRI) is the main tool that is used for this purpose [151]. The main limitations of MRI are the cost, complexity of use, complication of the heating protocol as all heating equipment must be MR compatible, furthermore the spatial resolution of traditional systems is limited to the mm scale. An alternative approach which overcomes many of these problems could be obtained using the photoacoustic technique [75, 76], however it has not yet been applied to *in vivo* intracellular temperature imaging. An even simpler proposed concept is to use thermistors [58], however this method has also not yet achieved thermal imaging in a live organism on a sub-cellular resolution.

6.3 *In vitro* vs. *In vivo*

To achieve the highest level of specificity in hyperthermia treatment the spatial resolution of the temperature feedback measurement should be at the cellular scale. However, obtaining the temperature over such a small spatial resolution seems to be a difficult task. In chapter 5 various methods for measuring temperature were presented. However, all these methods have only been demonstrated *in vitro* (by *in vitro* we refer to experiments performed on cultured cells whereas *in vivo* is assigned to experiments using intact organisms). Translation from basic *in vitro* research to an *in vivo* model can be crucial and

Table 6.1: *Considerations in applying in vitro research to in vivo models*

	In vitro	***In vivo***
Selective delivery	Facilitated by presence of only a single cell line	Difficult due to non-specificity of thermo probe
Compound concentration	Controllable by varying delivery conditions	Challenging to control due to complex system behavior
Toxicity	Easily tested for relevant cell line	Difficult testing as compounds could affect other systems

is considered a scientific milestone in many biomedical fields. However, *in vitro* research cannot always be translated to *in vivo* models. Some of the reasons for this are summarized in table 6.1. Indeed, in many cases clear discrepancies have been shown between *in vitro* and *in vivo* studies. One such example is given by Schurgers et al. [152]. Moreover, none of the reported thermal probes have so far been successfully applied to an *in vivo* model, mostly because all of these methods rely on the introduction of foreign thermo-sensitive or absorption contrast agents into cells either by endocytosis or microinjection techniques. Also, the concentration of these compounds within the cell must be optimized, a very challenging task when performed in an *in vivo* specimen. In addition, selective delivery of the thermo compounds to specific target cells in a live organism can be difficult, even impractical, whereas in the *in vitro* case this concern does not exist as they usually involve a single cell type. Furthermore, it will be hard to predetermine whether these compounds will be toxic or affect the basal conditions of the studied organism. Finally, it is not clear whether the reported probes will remain active once introduced into a live organism.

6.4 Temperature imaging in a live organism using GFP

In this study we believe to be the first to report intracellular temperature mapping in an *in vivo* model. This method, that overcomes the previously mentioned difficulties, is based on measuring the FPA of GFP allowing a fast,

accurate and noninvasive measurement in a live organism on a subcellular spatial scale. In the last chapter, we presented the ability to map temperature in an *in vitro* environment. Because of the GFPs biocompatibility, and its ubiquitous use in *in vivo* scientific models [121, 130], we were able to cross the chasm separating *in vitro* from *in vivo* measurements. The method is demonstrated on a permanently transfected *Caenorhabditis elegans* (*C. elegans*) strain expressing the GFP marker in the GABAergic neurons[1]. The *C. elegans* is a well-accepted *in vivo* model [153] which supports many advantages. The worm was the first multicellular organism to have its genome completely sequenced [154] (astonishingly, the genome has an estimated 70% gene conservation with humans). It is a highly attractive neuron model due to its simple nervous system (consisting of only 302 neurons for hermaphrodites) but which still supports a complex neurobehavioral repertoire. Its neuronal system has been completely mapped and contains almost all the biochemical components of the vertebrate one. Its almost 1000 cells reproduce many of the patterns and interactions of larger and more complex animals. It is optically transparent, which makes it an attractive model for microscopy studies. In this case we relied heavily on the transparency of the C. elegans, performing fluorescence microscopy on the intact organism. However, our method could be applied to some opaque models using a technique recently reported [155] which makes models transparent. If the model can not be made transparent, FPA measurements could still be performed with the aid of an imaging optical fiber [156]. Additionally a wide range of fluorescent proteins (such as GFP) can be selectively expressed in any cell [131]. The fact that genetically modified cells express the thermal probe, GFP, has several advantages. Firstly, it permits an established insertion of a probe which does not affect the cellular mechanisms and processes. Also, GFP can be selectively expressed only in the target cells of interest, thus overcoming the previously mentioned issue of specificity. The concentration variation of expressed GFP in permanent transfected species does not affect our measurements as FPA is a ratio of intensities, this also renders the FPA measurement non sensitive to fluctuations of the excitation laser intensity, photo bleaching, and probe migration (see chapter 5). The technique enables us to monitor small changes in the distribution of temperature in a single neuron of the *C. elegans*. In this chapter I present two different experimental configurations where the heat is delivered either from outside or inside the *C. elegans* by local photo-heating of GNRs.

[1] All preparation, transfection and handling of the worms was done by Cesar Alonso, under supervision of Dr. Susana Santos and help of Dr. Sebastian Thompson

6.5 Experimental results

Anisotropy as a temperature reporter in *C. elegans* neurons

The underlying physics relating temperature and molecular FPA is well established and has been explained in chapter 5. In the example presented in this chapter, we used GFP tagged to the enzyme Glutamic Acid Decarboxylase (GAD), which is expressed only in the GABAergic neurons of the C. elegans[2]. The main function of GAD involves a single step synthesis of the neurotransmitter GABA. The GAD-GFP complex is known to be located in the cell bodies, axon branches and synapses regions of these neurons and is believed to remain unbound [157] and thus free to rotate. When measuring FPA on this complex, the fluorescence lifetime is given by the GFP which is $\tau_F = 2.5$ns (as in Figure 5.1). The rotational lifetime, at a given temperature, depends both on the intracellular micro-viscosity and the proteins hydrodynamic volume, and in this case is the GAD-GFP combined volume. An experimental curve relating FPA of the GAD-GFP to temperature in an *in vivo* model was performed to obtain the real relationship between the anisotropy of GAD-GFP complex and temperature. This was done by placing the GFP transfected worms on a cover slip connected to an external electrical heater. The temperature was varied in the range: 24 °C - 35 °C, and kept well below temperatures that would cause biological damage. The temperature was varied slowly so that the temperature of the neurons was assumed to be equal to that of the heater. At different temperatures a confocal scan was performed giving an FPA map, as can be seen in Figure 6.1e-g. These images were taken when heating the system and also when cooling the system down to verify reversibility. The scan is performed with a collection time of 2 ms per pixel, and the entire image takes about 1 min to record. Indeed the FPA decreases as the temperature rises, as expected. These results are summarized in Figure 6.1h, which is an *in vivo* calibration curve. Each point is calculated by taking a spatial average of the measured FPA map in the *C. elegans* of the corresponding temperature. This curve presents an impressive sensitivity, given by the variation of FPA over this temperature range of about: 0.004 $^{\circ}C^{-1}$ (large compared to a value of a non-tagged GFP in PBS which is about 0.001 $^{\circ}C^{-1}$ as is presented in chapter 5). From this high sensitivity we can deduce that the fluorescence lifetime is on the same order of the rotational lifetime. It is worth noting that over this relatively small temperature range (24 °C - 35 °C)

[2]Specifically, the worm strain with the juIs76 [unc-25::GFP] II genotype that expresses the GFP attached to the GAD protein in the 26 GABAergic neurons' cytosol. The GFP labeled worm strain was obtained from Dr. Joe Culotti, from the Samuel Lunenfeld Research Institute (Toronto, Canada).

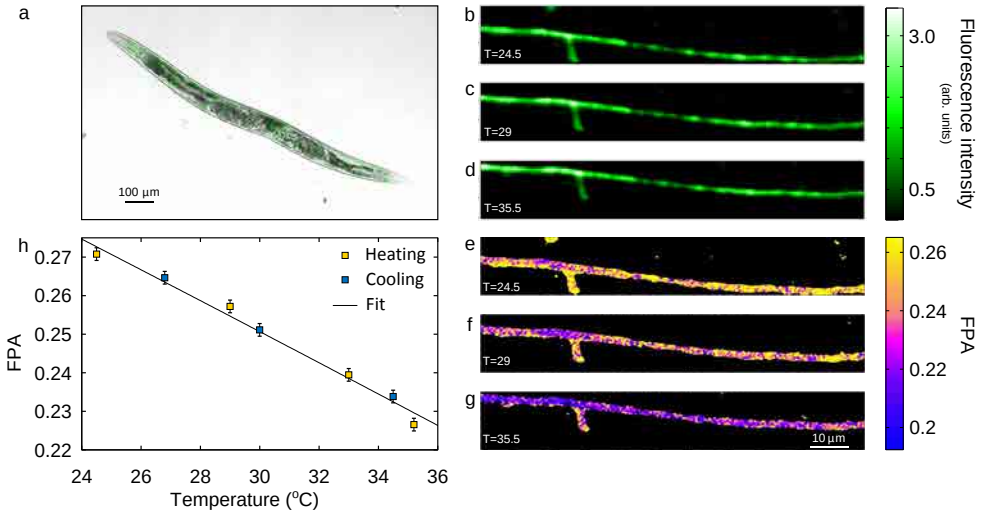

Figure 6.1: ***FPA Vs. Temperature calibration measurements in C. elegans.*** *(a) Bright-field image of the C. elegans overlapped with the GFP fluorescence intensity coming from the GABAergic neurons in green. (b,c,d) GFP fluorescence intensity from the same set of transfected neurons at three different temperatures. Over this range of temperatures the intensity variation is very small. (e,f,g) FPA of the same neurons at these same three temperatures. (h) Relationship between the average FPA and the temperature while heating and cooling the system in yellow and blue, respectively.*

the intensity of the GFP fluorescence does not change notably as can be seen in Figure 6.1b-d. We observe that the FPA maps are uniform although the intensity maps are not. Because FPA is a ratio of intensities, it is not influenced by variations in the fluorescence intensity. The uniform FPA also implies a rather homogeneous intracellular viscosity, which is consistent with the observations made in chapter 5 section 5.4. To asses uniformity of the FPA a high resolution scan was performed over a smaller area and is presented in Figure 6.2. In the data histogram, (Figure 6.2c), a normal distribution around one central FPA value is observed, corresponding to one uniform viscosity. If there were different viscosity areas these would show up as more peaks in the histogram[3].

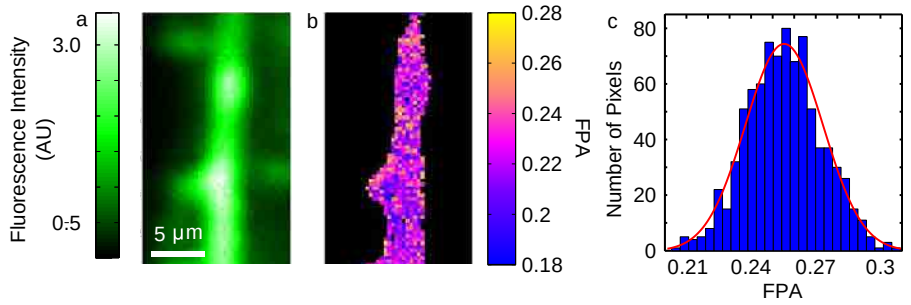

Figure 6.2: ***High resolution fluorescence imaging of transfected neurons of C. Elegans.*** *(a) Intensity and (b) FPA of a set of transfected neurons. (c) Histogram of the FPA image in b and a normal distribution fit (red line). From the single peak and uniformity of FPA we can deduce a uniform viscosity experienced by the protein complex. The presented data was collected with an exposure rate of 5ms/pixel, and hence the relatively large standard deviation of the data (compared to the error reported in the main text)*

To estimate a characteristic temperature sensitivity, data was acquired from one location during 20 s, at a rate of 0.3 s per data point, the standard deviation of this data set was taken to be the measurement error. The temperature during the measurement was constant and so the standard deviation gives an indication of the temperature error introduced by the measurement. This calculation gave a value corresponding to 0.8 °C and is the size of the error bars in Figure

[3]The image spans values of FPA between 0.24-0.27 is taken with an acquisition time of 5 ms per pixel. For this reason the temperature error is higher than the stated temperature error of 0.8 °C (which was averaged over a longer exposure time as explained in the text).

6.1h. which is comparable with reported thermal sensitivity of luminescent nanothermometers of 0.18-4 °C [50, 51]. Note however that these sensitivities were not measured in a single standardized way.

Intracellular temperature mapping: external heating

Once the calibration curve was obtained we performed an experiment in which we map the temperature inside the *C. elegans* resulting from external heating. Heating was induced by illuminating GNRs dispersed in the medium surrounding the worm. For an incident wavelength matching their plasmon resonance, the GNRs efficiently convert the laser power to heat providing quick and local heating of the specimen (see chapter 1).

In this experiment the GNRs were placed and illuminated with a CW laser beam outside the *C. elegans*, mimicking configurations where external heat is applied to obtain a desired cell activity, such as the use of thermo polymers for drug delivery [148]. In this context, temperature mapping can help to understand the quantity and spatial distribution of the delivered heat at the target cell with a ms time resolution. Figure 6.3c,d shows the temperature mapping of the *C. elegans* neurons without and with applying heat to the system, respectively. When heating a small change in the temperature can be observed over the entire image. Figures 6.3e-g are higher resolution scans on a smaller region in which the temperature change is mapped on a subcellular scale. An average raise of temperature of 2 °C is measured. As the fluorescence intensity of the GFP is much higher than the intrinsic auto fluorescence, a digital intensity threshold was applied to obtain FPA information only from the GAD-GFP and not the surrounding intrinsic auto fluorescence of the *C. elegans*. It is worth mentioning that because we are measuring neurons in a live organism, they have a 3D structure (as opposed to a 2D, flat geometry of the cells in an *in vitro* model), however due to the z plane sectioning that is achieved by a confocal system signal from outside the imaging plane is filtered out.

Intracellular temperature mapping: internal photo heating

In a second step, we performed an experiment in which heat was locally generated from within the *C. elegans*. We demonstrate that the method based on FPA enables to map temperature in real time even for this configuration. This is an important practical example because it concurs with the approach used in fields of photothermal cancer therapy.

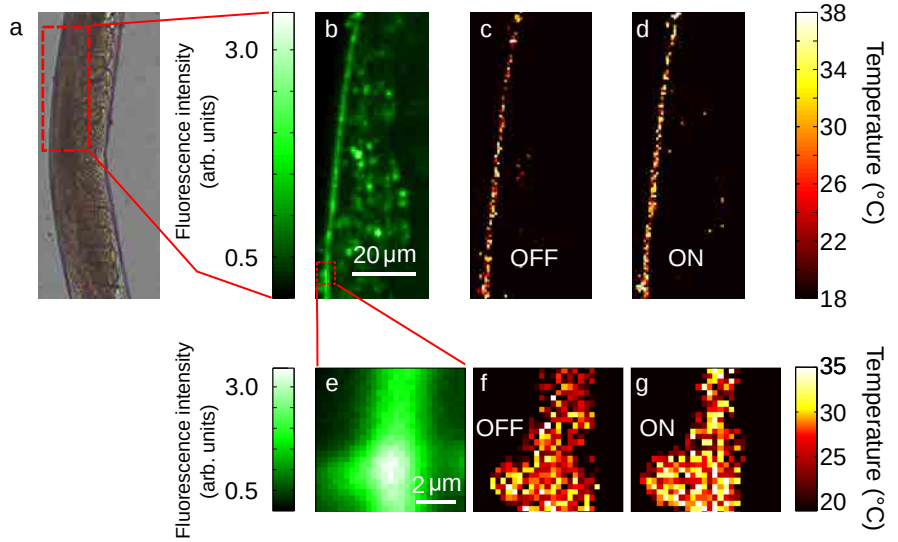

Figure 6.3: ***Intracellular temperature measurements in C. elegans under external heating.*** *(a) Bright field image of C. elegans. (b) Fluorescence intensity of GFP transfected neurons in the C. elegans. (c) Temperature image of the neurons when the laser is off. (d) Temperature image of the neurons when the laser is on and focused onto GNRs which are located outside the worm. The laser has a power of P=50 mW (63 kW/cm2) and is focused 50 µm to the left of the worm (specifically, 50 µm to the left of the bottom left corner of the red square in subfigure (a)). (e,f,g) Repeating the previous heating experiment while zooming in and imaging a smaller area.*

The worms were fed overnight with the GNRs that accumulated in their digestive tract. Then the worms are anesthetized and immediately used for experimentation, thus the concentration of GNRs inside the organism remains constant during the duration of the experiment (a few hours). No effect on the dynamics of the *C. elegans* was observed due to the GNRs. Figure 6.4a shows an example of presence and location of the GNRs which were identified using two-photon luminescence non-linear microscopy [158].

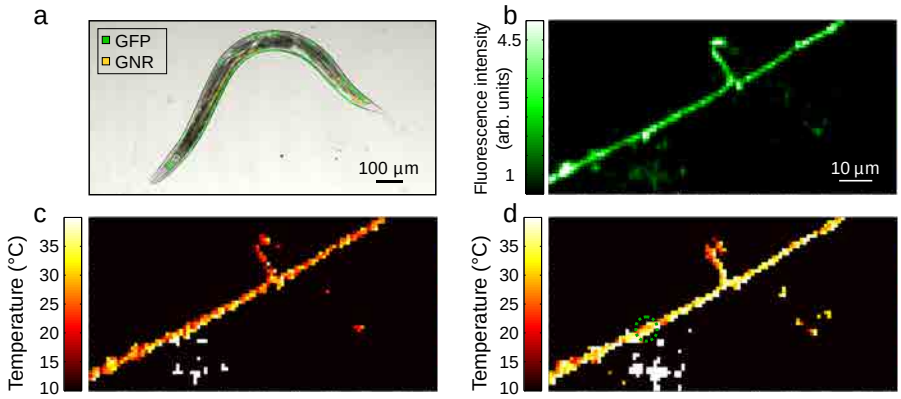

Figure 6.4: ***Intracellular temperature measurements during internal heating.*** *(a) Bright field image of C. elegans overlapped with the GFP fluorescence intensity coming from the GABAergic neurons in green, and the two photon luminescence signal coming from GNRs in yellow. The GNRs are concentrated in the worms digestive tract. (b) Fluorescence intensity of GFP transfected neurons in the C. elegans. (c) Temperature image of the neurons when the laser is off. (d) Temperature image of the neurons when the laser is on. The laser is focused onto GNRs inside the C. elegans, is located about 50 µm away from the center of the neurons in the perpendicular direction. The power is set to P=100 mW (127 kW/cm2). The heating is generated via photothermal conversion of GNRs which are inside the worm (GNRs are located as in Figure 6.4a).*

After the preliminary steps of preparing the GFP transfected worms with GNRs, the temperature change of the neurons was recorded when switching on the CW NIR heating laser (Figure 6.4b-d). The first notable feature is that the temperature rises uniformly over the scanned region (about 100 μm). As expected, heating from inside the worm is more efficient than heating from the

outside.

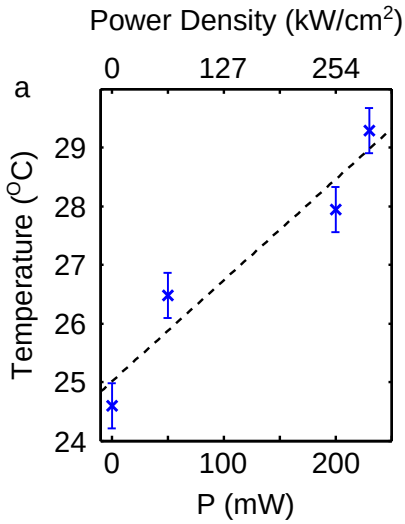

Figure 6.5: ***Dependence of temperature on incoming laser power*** *(a) The measurements were performed by recording FPA in one location and applying a heating laser at different powers to GNRs which were about 50 μm away in the same way as the experiment in Figure 6.6. A linear relationship is evidenced. The error bar size is 0.8 $^\circ C$ as explained in the text.*

A more systematic study was performed by measuring the temperature change in dependence of the incoming laser power and is presented in Figure 6.5. There is an expected linear relationship between temperature and the incoming heating laser power because the heat equations are linear as well as photothermal conversion (see chapter 1).

Finally, a real time temperature measurement was performed in a fixed position while the intensity of the CW NIR laser switched between off and on. Time-evolution of the temperature is presented in Figure 6.6, in which the data were collected on a time scale of 20 ms per data point. Shining the GNRs with a laser of 50 mW (power density of 63 kW/cm^2 at focal plane) induces a change in temperature of almost 3 °C. Similar power densities shined on GNRs

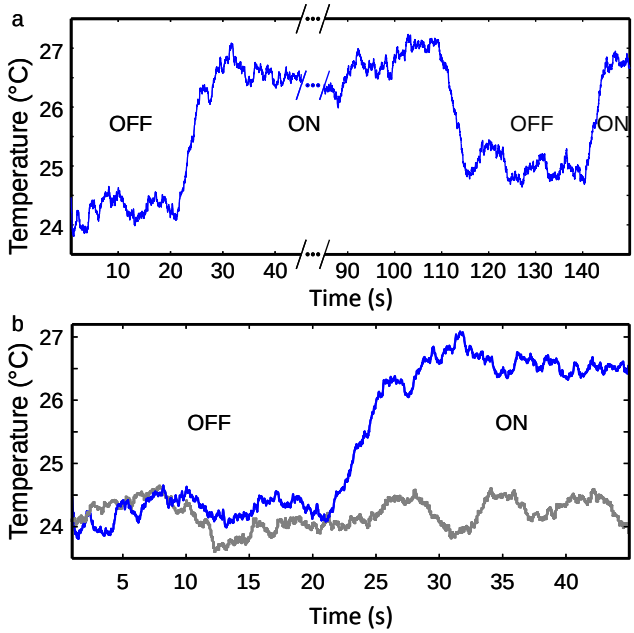

Figure 6.6: ***Temperature as function of time during photothermal heating.*** *(a) Temperature measured at one point as a function of time. The point is marked with a green circle in Figure 6.4d. The laser was turned on at t=20 s and the subsequent change of temperature was measured and presented in the blue curve (the laser was focused onto GNRs inside the worm and was set to a power of P=50 mW (63 kW/cm^2)). The heating laser was turned off after almost 2 minutes and turned back on at t=140s. (b) A control experiment performed on a worm with no GNRs and illuminated under similar conditions is presented in the gray curve. (In blue is the same scan as presented in subfigure a) till t=45 s). In both Figures, a smoothing function was applied, where each point was taken to be the average over 0.6 seconds of acquired data.*

which generated a comparable temperature raise have been previously reported in the literature [159] (100 kW/cm^2 which generated about a 2 °C temperature raise), due to a different system and specifically a different GNR concentration and distribution the heating is not expected to give exact same results. The temperature rises up to a point where a thermal equilibrium is obtained and the temperature reaches a plateau, a typical behavior of a heated open system [38]. In this case, the rise time of the temperature is a few seconds. This is longer than expected time when heating an area of micrometric dimensions (see chapter 1 eq. 1.8). We attribute this discrepancy to the fact that heating of GNRs occurs out of the focal plane of the 800nm laser in the entire digestive system of the *C. Elegans*, increasing the volume of the heated region and thus the thermalization time. When the heating source is turned off the temperature returns to a level near the original baseline. There is a small change in the baseline temperature (slightly less than 1 degree), which is close to the reported measurement error of 0.8°C. We attribute this temperature error to an artifact induced by movement of the biological sample, or possibly to thermal instability of the system. A control experiment was performed on a different worm that was not incubated with GNRs. The worm was illuminated under similar conditions (similar power and distance from measurement point). The resulting temperature trace is presented in the gray curve in Figure 6.6b. As expected the temperature does not rise when the laser is on, which confirms that the photothermal conversion is induced by the GNRs and not by the *C. elegans* tissue. Ultimately, such dynamic temperature monitoring could be useful for example to track the temperature change during neuron synapses or reticulum endoplasmic calcium release in mammalian cells.

6.6 Summary and outlook

In this chapter we presented the first *in vivo* intracellular temperature mapping technique in a live model organism. This was achieved by monitoring the FPA of GAD-GFP protein complex, which was permanently expressed in the GABAergic neurons of the *C. elegans* soil worm. However, the applicability of the method is not restricted to this specific protein complex or with this living organism. The implementation of the method on other organisms will be greatly facilitated by the extended usage of GFP transfected models [131]. When using this technique with GFP tagged to other proteins, one should expect a different accuracy of the temperature measurement. The other protein complex will have a different rotational lifetime than the GAD-GFP, which then will change the calibration curve relating FPA to temperature. In practice, the relation

between the FPA and the temperature of the new protein complex must be re-established as in Figure 6.1h. To be able to accurately measure local temperature the FPA-temperature calibration curve must fulfill two requirements. Firstly, the FPA map must be uniform and reach a level higher than the measurement noise. Secondly, the curve must be reversible i.e. when lowering the temperature one must obtain the same FPA value. The uniformity implies that the thermal probe experiences a uniform viscosity in the cell, and does not bind to specific intracellular structures. The reversibility implies that no changes in protein structure have occurred and that if any protein binding occurs, this is factored into the measured FPA. In the case that part of the proteins bind to cellular structures (even if the binding depends on temperature) the FPA reading will be modified, and the sensitivity of the measurement reduced but the FPA calibration curve will still give accurate results. The sensitivity will be reduced in the case that the non bound protein was ideal prior to the binding, in the sense that $\tau_F \approx \tau_R$. One could engineer a scenario where the FPA is most sensitive *after* the fluorescent marker binds to some predetermined macromolecule or protein. Thereafter, intracellular temperature can be directly monitored by measuring FPA, this can be done either to obtain temperature imaging similar to Figure 6.4c,d or real time temperature measurements as in Figure 6.6. We have seen that the GAD-GFP complex delivers superior accuracy compared to a non-tagged GFP[4], we do expect there to be further optimization to this accuracy by using proteins of other size and structure to GFP.

We also believe that a pertinent line of investigation would be to apply the method to perform temperature measurements in different tissues, where the intracellular temperature of cells is measured together with the extracellular matrix. Also, to better improve tissue penetration, different fluorescent proteins such as red fluorescent protein and its derivatives can be used where the fluorescence spectral window matches that of tissue transparency window. When applying this method to non-transparent tissues, the randomness of the tissue structure and the multiple scattering events will result in depolarization of the propagating light, thus adding noise to the FPA measurement. In strongly scattering tissue the depolarization length, defined as the length where the ratio $I_{\parallel}/I_{\perp}$ decreases by 2, where $I_{\parallel}$ and $I_{\perp}$ are the intensities of the fluorescence polarized parallel and perpendicular to the incident polarization, depends on the tissue and wavelength. Characteristic lengths are 0.2 to about 4 mm for white matter of brain and whole blood with a low level of hematocrit, respec-

[4]When making this comparison, we should remember that the FPA sensitivity of the GAD-GFP complex was measured in the worm and specifically in a different environment to the GFP which was measured in PBS.

tively [160]. For transparent tissues such as eye tissues, cellular monolayers, mucous membrane and superficial skin layers the polarization of transmitted light remains measurable for larger distances.

Summary and outlook

In this thesis, nano particles were used as efficient, remotely controllable and spectrally selective nano sources of heat, when shined on at their plasmonic resonance. This strategy is at the basis of a rapidly growing and promising field called thermo-plasmonics. In a first part of the thesis, we describe the Joule effect induced in plasmonic gold nanoparticles. We show that the presence of the resonant oscillation of the electron gas enables to enhance the absorption cross section and consequently the heat generation. This general concept was later used in different applications in both physical and biological environments.

In chapter 3 we demonstrated a fast tunable Photothermal Lens (PTL) based on plasmonic heating. First, we developed a model to predict the lens behavior. Next, experimental characterization of a fabricated thermal lens was performed. Finally, we showed that such a system could be used for fast and accurate focal plane tunability as well as for adaptive optics applications. A possibility to further develop this study would be to pattern the incoming heating beam or the absorbing structures to manipulate the temperature and optical landscape. Among potential applications, the PTL could be used to individually control the focus of arrays of micro-lenses. Another foreseen application is to use the PTL as an adptive optical element operating in transmission for 3D imaging.

In a broader context, the PTL can be considered one of a myriad of possibilities which thermo-plasmonics enables [19]. Such fruitful applications will spur the scientific community to further investigate and better understand more intricate aspects of thermo-plasmonic heating. Indeed, progress in understanding how to generate more efficient and accurate temperature profiles will enable higher degrees of dexterity of thermo-plasmonic applications. Also further investigation and experiments of short time scales (ns and below) of thermo-plasmonic applications may allow interesting fast applications. An example of a striking and potentially ubiquitous application based on these concepts is the ability to increase data storage density by more than one order of magnitude

($\approx$1Tb \ inch^{-2}) by using the localized heating generated by a plasmonic antenna [161].

Thermo-plasmonics could be combined with another field to generate new functionalities. Indeed, as reported in a review by Kim [23], applications based on plasmonic effects have become more prevalent in micro/nano-fluidic systems, forming a new field called *plasmo-fluidics*. The need to combine these two areas is reported to be beneficial and often even inevitable. To this end the basic physics and behavior of plasmonic induced optofluidics must be understood. In this context, in chapter 4 we perform systematic dimensional analysis on the Navier Stokes and heat transport equations, we investigated the physics of fluid convection induced by heat release from plasmonic particles. Next, we numerically calculated the fluid convection that is induced by plasmonic heating at the micro and nanoscale. The numerical calculations performed in the thesis are related to general concepts on which experimental applications can be built. In this direction, a recent work reports on theoretical and experimental results concerning a basic case of convection induced by plasmonic arrays [162]. Based on such general work, the field of plasmo-fluidics may start to generate new practical functionalities. The experimental work done in this thesis can be seen as a step in this direction, where the plasmonic heating is directly used to induce a fluidic behavior. In this work, we describe the fabrication and testing of a microfluidic pump based on plasmonic heating. This is one of the first practical applications in the field of plasmo-fluidics. Possible utilization of such a device could be to guide a fluid within channels, eliminating the need for external large and usually expensive pumps. In a realistic system the basic concept we proposed could take a more complex form, for example in a configuration where one channel diverges into two (a T junction) and the microfluidic pump could redirect the flow into one desired channel. In general, the local engineering of flow patterns by plasmo-fluidics can be used to improve an existing functionality of an on chip fluidic device. For instance, one could increase the effectiveness of a sensing device by locally redirecting the flow to the area of the sensors. This addresses a general issue where in many micro-fluidic applications the sensors are positioned on the boundaries of the channels, exactly where the flow is minimal.

The applications mentioned above rely on the efficient opto-thermal conversion in gold nano particles to generate local heat sources. One advantage of gold is that it is non toxic, allowing the application of thermo-plasmonics to bio systems. This is a pertinent line of investigation, because temperature is a basic parameter which influences many cellular biological processes. Thus, heat

generation and monitoring could have meaningful contributions in biological and even medical applications. Nanotechnology is not only providing new ways to generate point like heat sources but also to monitor the resulting temperature gradients with high precision. As more accurate thermometry methods are discovered, we can expect to better understand the influence of temperature in cellular biochemical reactions and gain a higher degree of control over temperature induced processes. In a second part of the thesis, I describe a tool that permits the measurement of temperature at the nanoscale. This is done by monitoring the fluorescence polarization anisotropy (FPA) of a fluorescent molecule. This versatile technique was applied to both physical and biological systems. In chapter 5 we presented the use of Green Fluorescent Protein (GFP) as a thermal nanoprobe suited for *in vitro* cellular temperature mapping. This is performed by monitoring the FPA of the GFP. We applied this method to measure the temperature generated by photothermal heating of gold nanorods inside and outside cells. In chapter 6 we extended the technique and performed the first *in vivo* intracellular thermal imaging which was demonstrated on GFP expressing neurons of a worm. In both cases the method supports diffraction limited spatial resolution, good temperature accuracy and fast readout. High bio-compatibility is the main advantage of this method. Indeed, beyond DNA transfection the temperature probe is "naturally" introduced by the biological system itself. Because of the nanometric size of the reporter protein, there is hope to further increase the spacial resolution of the measurement. To further optimize the temperature accuracy, the size of the protein could be optimized to make the rotational and fluorescence life time of the protein closer. This can be done by connecting the GFP to proteins of different sizes. Another way to increase the temperature accuracy would be to use two photon excitation of the GFP fluorescence. In this case the limiting anisotropy (for one photon $r_0 \leq 0.4$) can be larger which in turn renders the measurement error smaller. Another interesting direction to study could be the applicability of the method in a non-transparent *in vivo* tissue. One approach to accomplish this would be to collect the fluorescence with a polarization conserving fiber optic. Once the temperature accuracy is increased and the method could be used in a non transparent organism, many applications could be envisioned. One proposal is to study whether neuronal signaling can be correlated with a local increase of temperature. Another potentially significant application is to use intracellular thermometry as input to a feedback while heating tissue in hyperthermia treatment. Despite the chasm separating between thermometry in GFP transfected C. Elegans to monitoring temperature in humans in the operating room, this work can be seen as a step in this direction.

Bibliography

[1] X. Michalet, F. F. Pinaud, L. A. Bentolila, J. M. Tsay, S. Doose, J. J. Li, G. Sundaresan, A. M. Wu, S. S. Gambhir, and S. Weiss, "Quantum dots for live cells, in vivo imaging, and diagnostics," *Science*, vol. 307, no. 5709, pp. 538–544, 2005.

[2] M. Geiselmann, M. L. Juan, J. Renger, J. M. Say, L. J. Brown, F. J. G. de Abajo, F. Koppens, and R. Quidant, "Three-dimensional optical manipulation of a single electron spin," *Nat Nano*, vol. 8, pp. 175–179, Mar. 2013.

[3] J. Gieseler, L. Novotny, and R. Quidant, "Thermal nonlinearities in a nanomechanical oscillator," *Nat Phys*, vol. 9, pp. 806–810, Dec. 2013.

[4] E. Ozbay, "Plasmonics: Merging photonics and electronics at nanoscale dimensions," *Science*, vol. 311, no. 5758, pp. 189–193, 2006.

[5] L. Novotny and N. van Hulst, "Antennas for light," *Nat Photon*, vol. 5, pp. 83–90, Feb. 2011.

[6] P. K. Jain, I. H. El-Sayed, and M. A. El-Sayed, "Au nanoparticles target cancer," *Nano Today*, vol. 2, no. 1, pp. 18 – 29, 2007.

[7] D. Punj, M. Mivelle, S. B. Moparthi, T. S. van Zanten, H. Rigneault, N. F. van Hulst, M. F. Garcia-Parajo, and J. Wenger, "A plasmonic 'antenna-in-box' platform for enhanced single-molecule analysis at micromolar concentrations," *Nat Nano*, vol. 8, pp. 512–516, July 2013.

[8] P. Mhlschlegel, H.-J. Eisler, O. J. F. Martin, B. Hecht, and D. W. Pohl, "Resonant optical antennas," *Science*, vol. 308, no. 5728, pp. 1607–1609, 2005.

[9] P. Bharadwaj, B. Deutsch, and L. Novotny, "Optical antennas," *Advances in Optics and Photonics*, vol. 1, no. 3, pp. 438–483, 2009.

[10] M. Coronado-Puchau, L. Saa, M. Grzelczak, V. Pavlov, and L. M. Liz-Marzn, "Enzymatic modulation of gold nanorod growth and application to nerve gas detection," *Nano Today*, vol. 8, no. 5, pp. 461 – 468, 2013.

[11] G. Baffou, R. Quidant, and C. Girard, "Heat generation in plasmonic nanostructures: Influence of morphology," *Appl. Phys. Lett.*, vol. 94, p. 153109, 2009.

[12] A. L. Gonzalez and C. Noguez, "Influence of morphology on the optical properties of metal nanoparticles," *J. Comput. Theor. Nanos.*, vol. 4, no. 2, p. 231, 2006.

[13] K. L. Kelly, E. Coronado, L. L. Zhao, and G. C. Schatz, "The optical properties of metal nanoparticles: The influence of size, shape, and dielectric environment," *J. Phys. Chem. B*, vol. 107, p. 668, 2003.

[14] L. Novotny, "Effective wavelength scaling for optical antennas," *Phys. Rev. Lett.*, vol. 98, p. 266802, Jun 2007.

[15] A. G. Curto, G. Volpe, T. H. Taminiau, M. P. Kreuzer, R. Quidant, and N. F. van Hulst, "Unidirectional emission of a quantum dot coupled to a nanoantenna," *Science*, vol. 329, no. 5994, pp. 930–933, 2010.

[16] A. O. Govorov and H. H. Richardson, "Generating heat with metal nanoparticles," *Nano Today*, vol. 2, no. 1, p. 30, 2007.

[17] H. H. Richardson, Z. N. Hickman, A. O. Govorov, A. C. Thomas, W. Zhang, and M. E. Kordesch, "Thermooptical properties of gold nanoparticles embedded in ice: Characterization of heat generation and melting," *Nano Letters*, vol. 6, no. 4, pp. 783–788, 2006.

[18] W. L. Barnes, A. Dereux, and T. W. Ebbesen, "Surface plasmon subwavelength optics," *Nature*, vol. 424, pp. 824–830, Aug. 2003.

[19] G. Baffou and R. Quidant, "Thermo-plasmonics: using metallic nanostructures as nano-sources of heat," *Laser & Photonics Reviews*, vol. 7, no. 2, pp. 171–187, 2013.

[20] A. O. Govorov, Z. Fan, and A. B. Neiman, *Photothermal Effect of Plasmonic Nanoparticles and Related Bioapplications*, pp. 455–475. Wiley-VCH Verlag GmbH & Co. KGaA, 2012.

[21] M. Fedoruk, M. Meixner, S. Carretero-Palacios, T. Lohmller, and J. Feldmann, "Nanolithography by plasmonic heating and optical manipulation of gold nanoparticles," *ACS Nano*, vol. 7, no. 9, pp. 7648–7653, 2013.

[22] D. A. Boyd, L. Greengard, M. Brongersma, M. Y. El-Naggar, and D. G. Goodwin, "Plasmon-assisted chemical vapor deposition," *Nano Lett.*, vol. 6, no. 11, pp. 2592–2597, 2006.

[23] J. Kim, "Joining plasmonics with microfluidics: from convenience to inevitability," *Lab. Chip*, vol. 12, pp. 3611–3623, 2012.

[24] D. Boyer, P. Tamarat, A. Maali, and M. Lounis, B. Orrit, "Photothermal imaging of nanometer-sized metal particles among scatterers," *Science*, vol. 297, p. 1160, 2002.

[25] A. Agarwal, S. Huang, M. ODonnell, K. C. Day, M. Day, N. Kotov, and S. Ashkenazi, "Targeted gold nanorod contrast agent for prostate cancer detection by photoacoustic imaging," *J. Appl. Phys.*, vol. 102, no. 6, pp. 064701–4, 2007.

[26] F. X. Gu, R. Karnik, A. Z. Wang, F. Alexis, E. Levy-Nissenbaum, S. Hong, R. S. Langer, and O. C. Farokhzad, "Targeted nanoparticles for cancer therapy," *Nano Today*, vol. 2, no. 3, p. 14, 2007.

[27] N. Khlebtsov and L. Dykman, "Biodistribution and toxicity of engineered gold nanoparticles: a review of in vitro and in vivo studies," *Chem. Soc. Rev.*, vol. 40, pp. 1647–1671, 2011.

[28] R. Weissleder, "A clearer vision for in vivo imaging," *Nat Biotech*, vol. 19, pp. 316–317, Apr. 2001.

[29] K. A. Willets and R. P. Van Duyne, "Localized surface plasmon resonance spectroscopy and sensing," *Annu. Rev. Phys. Chem.*, vol. 58, no. 1, pp. 267–297, 2007.

[30] R. Marty, G. Baffou, A. Arbouet, C. Girard, and R. Quidant, "Charge distribution induced inside complex plasmonic nanoparticles," *Opt. Express*, vol. 18, p. 3035, 2010.

[31] B. Palpant, *Photothermal Properties of Gold Nanoparticles*, ch. 4, pp. 75–102. Imperial College Press, 2012.

[32] G. Baffou, C. Girard, and R. Quidant, "Mapping heat origin in plasmonic structures," *Phys. Rev. Lett.*, vol. 104, p. 136805, Apr 2010.

[33] J. M. McMahon, S. K. Gray, and G. C. Schatz, "Nonlocal optical response of metal nanostructures with arbitrary shape," *Phys. Rev. Lett.*, vol. 103, p. 097403, Aug 2009.

[34] M. A. van Dijk, M. Lippitz, and M. Orrit, "Detection of acoustic oscillations of single gold nanospheres by time-resolved interferometry," *Phys. Rev. Lett.*, vol. 95, p. 267406, Dec 2005.

[35] J. S. Donner, G. Baffou, D. McCloskey, and R. Quidant, "Plasmon-Assisted Optofluidics," *ACS Nano*, vol. 5, pp. 5457–5462, June 2011.

[36] G. Baffou, R. Quidant, and F. J. Garcia de Abajo, "Nanoscale control of optical heating in complex plasmonic systems," *ACS Nano*, vol. 4, no. 2, pp. 709–716, 2010.

[37] G. Baffou and H. Rigneault, "Femtosecond-pulsed optical heating of gold nanoparticles," *Phys. Rev. B*, vol. 84, p. 035415, Jul 2011.

[38] H. H. Richardson, M. T. Carlson, P. J. Tandler, P. Hernandez, and A. O. Govorov, "Experimental and theoretical studies of light-to-heat conversion and collective heating effects in metal nanoparticle solutions," *Nano Lett.*, vol. 9, pp. 1139–1146, Feb. 2009.

[39] G. Baffou, R. Quidant, and C. Girard, "Thermoplasmonics modeling: A green's function approach," *Phys. Rev. B*, vol. 82, p. 165424, Oct 2010.

[40] L. M. Maestro, P. Haro-Gonzlez, A. Snchez-Iglesias, L. M. Liz-Marzn, J. Garca Sol, and D. Jaque, "Quantum dot thermometry evaluation of geometry dependent heating efficiency in gold nanoparticles," *Langmuir*, vol. 30, no. 6, pp. 1650–1658, 2014.

[41] M. Hu, J. Chen, Z.-Y. Li, L. Au, G. V. Hartland, X. Li, M. Marquez, and Y. Xia, "Gold nanostructures: engineering their plasmonic properties for biomedical applications," *Chem. Soc. Rev.*, vol. 35, pp. 1084–1094, 2006.

[42] S. Link and M. A. El-Sayed, "Shape and size dependence of radiative, non-radiative and photothermal properties of gold nanocrystals," *Int. Rev. Phys. Chem.*, vol. 19, no. 3, p. 409, 2000.

[43] P. K. Jain, X. Huang, I. H. El-Sayed, and M. A. El-Sayed, "Noble metals on the nanoscale: Optical and photothermal properties and some applications in imaging, sensing, biology, and medicine," *Acc. Chem. Res.*, vol. 41, no. 12, pp. 1578–1586, 2008.

[44] A. R. Tao, S. Habas, and P. Yang, "Shape control of colloidal metal nanocrystals," *Small*, vol. 4, no. 3, pp. 310–325, 2008.

[45] S. S. Acimovic, M. P. Kreuzer, M. U. Gonzlez, and R. Quidant, "Plasmon near-field coupling in metal dimers as a step toward single-molecule sensing," *ACS Nano*, vol. 3, no. 5, pp. 1231–1237, 2009.

[46] B. Nikoobakht and M. A. El-Sayed, "Preparation and growth mechanism of gold nanorods (NRs) using seed-mediated growth method," *Chem. Mat.*, vol. 15, p. 1957, 2003.

[47] X. Huang, I. H. El-Sayed, W. Qian, and M. A. El-Sayed, "Cancer cell imaging and photothermal therapy in the near-infrared region by using gold nanorods," *J. Am. Chem. Soc.*, vol. 128, no. 6, p. 2115, 2006.

[48] G. Veronis and S. Fan, "Modes of subwavelength plasmonic slot waveguides," *J. Lightwave Technol.*, vol. 25, pp. 2511–2521, Sep 2007.

[49] D. P. Edward and I. Palik, *Handbook of optical constants of solids*. Academic Press Inc. Londres, 1985.

[50] D. Jaque and F. Vetrone, "Luminescence nanothermometry," *Nanoscale*, vol. 4, pp. 4301–4326, 2012.

[51] C. D. S. Brites, P. P. Lima, N. J. O. Silva, A. Millan, V. S. Amaral, F. Palacio, and L. D. Carlos, "Thermometry at the nanoscale," *Nanoscale*, vol. 4, pp. 4799–4829, 2012.

[52] J. Lee and N. A. Kotov, "Thermometer design at the nanoscale," *Nano Today*, vol. 2, no. 1, pp. 48 – 51, 2007.

[53] H. Hamann, A. Weger, J. Lacey, Z. Hu, P. Bose, E. Cohen, and J. Wakil, "Hotspot-limited microprocessors: Direct temperature and power distribution measurements," *Solid-State Circuits, IEEE Journal of*, vol. 42, no. 1, pp. 56–65, 2007.

[54] J. Gosciniak and S. I. Bozhevolnyi, "Performance of thermo-optic components based on dielectric-loaded surface plasmon polariton waveguides," *Sci. Rep.*, vol. 3, pp. –, May 2013.

[55] Y. Kamei, M. Suzuki, K. Watanabe, K. Fujimori, T. Kawasaki, T. Deguchi, Y. Yoneda, T. Todo, S. Takagi, T. Funatsu, and S. Yuba, "Infrared laser-mediated gene induction in targeted single cells in vivo," *Nat Meth*, vol. 6, pp. 79–81, Jan. 2009.

[56] B. B. Lowell and B. M. Spiegelman, "Towards a molecular understanding of adaptive thermogenesis," *Nature*, vol. 404, pp. 652–660, Apr. 2000.

[57] Z. B. Andrews, S. Diano, and T. L. Horvath, "Mitochondrial uncoupling proteins in the cns: in support of function and survival," *Nat. Rev. Neurosci.*, vol. 6, pp. 829–840, Nov. 2005.

[58] P. Wust, B. Hildebrandt, G. Sreenivasa, B. Rau, J. Gellermann, H. Riess, R. Felix, and P. M. Schlag, "Hyperthermia in combined treatment of cancer.," *The lancet oncology*, vol. 3, no. 8, pp. 487–497, 2002.

[59] J. L. West, "Nanoshell-mediated near-infrared thermal therapy of tumors under magnetic resonance guidance," *PNAS*, vol. 100, no. 23, pp. 13549–13554, 2003.

[60] R. Bardhan, S. Lal, A. Joshi, and N. J. Halas, "Theranostic Nanoshells: From Probe Design to Imaging and Treatment of Cancer," *Acc. Chem. Res.*, vol. 44, pp. 936–946, May 2011.

[61] G. A. Koning, A. M. M. Eggermont, L. H. Lindner, and T. L. M. ten Hagen, "Hyperthermia and Thermosensitive Liposomes for Improved Delivery of Chemotherapeutic Drugs to Solid Tumors," *Pharm. Res.*, vol. 27, no. 8, pp. 1750–1754, 2010.

[62] B. M. Dicheva, T. L. M. T. Hagen, L. Li, D. Schipper, A. L. B. Seynhaeve, G. C. V. Rhoon, A. M. M. Eggermont, L. H. Lindner, and G. a. Koning, "Cationic Thermosensitive Liposomes: A Novel Dual Targeted Heat-Triggered Drug Delivery Approach for Endothelial and Tumor Cells.," *Nano Lett.*, vol. 6, June 2013.

[63] Y.-L. Luo, Y.-S. Shiao, and Y.-F. Huang, "Release of photoactivatable drugs from plasmonic nanoparticles for targeted cancer therapy," *ACS Nano*, vol. 5, pp. 7796–7804, Sept. 2011.

[64] S. Kiyonaka, T. Kajimoto, R. Sakaguchi, D. Shinmi, M. Omatsu-Kanbe, H. Matsuura, H. Imamura, T. Yoshizaki, I. Hamachi, T. Morii, and Y. Mori, "Genetically encoded fluorescent thermosensors visualize subcellular thermoregulation in living cells," *Nat Meth*, vol. 10, pp. 1232–1238, Dec. 2013.

[65] W. Lee, K. Kim, W. Jeong, L. A. Zotti, F. Pauly, J. C. Cuevas, and P. Reddy, "Heat dissipation in atomic-scale junctions," *Nature*, vol. 498, pp. 209–212, June 2013.

[66] C. Wang, R. Xu, W. Tian, X. Jiang, Z. Cui, M. Wang, H. Sun, K. Fang, and N. Gu, "Determining intracellular temperature at single-cell level by a novel thermocouple method," *Cell Res.*, vol. 21, pp. 1517–1519, Oct. 2011.

[67] O. Nakabeppu, M. Chandrachood, Y. Wu, J. Lai, and A. Majumdar, "Scanning thermal imaging microscopy using composite cantilever probes," *Appl. Phys. Lett.*, vol. 66, no. 6, pp. 694–696, 1995.

[68] Y. Gao and Y. Bando, "Nanotechnology: Carbon nanothermometer containing gallium," *Nature*, vol. 415, pp. 599–599, Feb. 2002.

[69] Z. Ioffe, T. Shamai, A. Ophir, G. Noy, I. Yutsis, K. Kfir, O. Cheshnovsky, and Y. Selzer, "Detection of heating in current-carrying molecular junctions by raman scattering," *Nat Nano*, vol. 3, pp. 727–732, Dec. 2008.

[70] G. Baffou, P. Bon, J. Savatier, J. Polleux, M. Zhu, M. Merlin, H. Rigneault, and S. Monneret, "Thermal imaging of nanostructures by quantitative optical phase analysis," *ACS Nano*, vol. 6, no. 3, pp. 2452–2458, 2012.

[71] P. Berto, E. B. Ureña, P. Bon, R. Quidant, H. Rigneault, and G. Baffou, "Quantitative absorption spectroscopy of nano-objects," *Phys. Rev. B*, vol. 86, p. 165417, Oct 2012.

[72] P. Bon, N. Belaid, D. Lagrange, C. Bergaud, H. Rigneault, S. Monneret, and G. Baffou, "Three-dimensional temperature imaging around a gold microwire," *Appl. Phys. Lett.*, vol. 102, no. 24, p. 244103, 2013.

[73] M. Zhu, G. Baffou, N. Meyerbrker, and J. Polleux, "Micropatterning thermoplasmonic gold nanoarrays to manipulate cell adhesion," *ACS Nano*, vol. 6, no. 8, pp. 7227–7233, 2012.

[74] K. T. Regner, D. P. Sellan, Z. Su, C. H. Amon, A. J. McGaughey, and J. A. Malen, "Broadband phonon mean free path contributions to thermal conductivity measured using frequency domain thermoreflectance," *Nat Commun*, vol. 4, p. 1640, Mar. 2013.

[75] L. Gao, L. Wang, C. Li, Y. Liu, H. Ke, C. Zhang, and L. V. Wang, "Single-cell photoacoustic thermometry," *J. Biomed. Opt*, vol. 18, p. 026003, Mar. 2013.

[76] L. Gao, C. Zhang, C. Li, and L. V. Wang, "Intracellular temperature mapping with fluorescence-assisted photoacoustic-thermometry," *Appl. Phys. Lett.*, vol. 102, no. 19, p. 193705, 2013.

[77] S. Li, K. Zhang, J.-M. Yang, L. Lin, and H. Yang, "Single quantum dots as local temperature markers," *Nano Lett.*, vol. 7, no. 10, pp. 3102–3105, 2007.

[78] L. M. Maestro, C. Jacinto, U. R. Silva, F. Vetrone, J. A. Capobianco, D. Jaque, and J. G. Sol, "CdTe quantum dots as nanothermometers: Towards highly sensitive thermal imaging," *Small*, vol. 7, no. 13, pp. 1774–1778, 2011.

[79] J.-m. Yang, H. Yang, and L. Lin, "Quantum dot nano thermometers reveal heterogeneous local thermogenesis in living cells," *ACS Nano*, vol. 5, no. 6, pp. 5067–5071, 2011.

[80] L. M. Maestro, E. M. Rodrguez, F. S. Rodrguez, M. C. I.-d. la Cruz, A. Juarranz, R. Naccache, F. Vetrone, D. Jaque, J. A. Capobianco, and J. G. Sole, "CdSe quantum dots for two-photon fluorescence thermal imaging," *Nano Lett.*, vol. 10, no. 12, pp. 5109–5115, 2010.

[81] A. Al Salman, A. Tortschanoff, M. B. Mohamed, D. Tonti, F. van Mourik, and M. Chergui, "Temperature effects on the spectral properties of colloidal cdse nanodots, nanorods, and tetrapods," *Applied Physics Letters*, vol. 90, no. 9, pp. –, 2007.

[82] G. Kucsko, P. C. Maurer, N. Y. Yao, M. Kubo, H. J. Noh, P. K. Lo, H. Park, and M. D. Lukin, "Nanometre-scale thermometry in a living cell," *Nature*, vol. 500, pp. 54–58, Aug. 2013.

[83] D. M. Toyli, C. F. de las Casas, D. J. Christle, V. V. Dobrovitski, and D. D. Awschalom, "Fluorescence thermometry enhanced by the quantum coherence of single spins in diamond," *Proceedings of the National Academy of Sciences*, vol. 110, no. 21, pp. 8417–8421, 2013.

[84] K. Okabe, N. Inada, C. Gota, Y. Harada, T. Funatsu, and S. Uchiyama, "Intracellular temperature mapping with a fluorescent polymeric thermometer and fluorescence lifetime imaging microscopy," *Nat. Commun.*, vol. 3, Jan. 2012.

[85] R. Zondervan, F. Kulzer, H. van der Meer, J. A. J. M. Disselhorst, and M. Orrit, "Laser-driven microsecond temperature cycles analyzed by fluorescence polarization microscopy," *Biophys. J.*, vol. 90, p. 2958, 2006.

[86] G. Baffou, M. P. Kreuzer, F. Kulzer, and R. Quidant, "Temperature mapping near plasmonic nanostructures using fluorescence polarization anisotropy," *Opt. Express*, vol. 17, pp. 3291–3298, Mar. 2009.

[87] B. Valeur, *Molecular Fluorescence: Principles and Applications*. Wiley-VCH, Oct. 2007.

[88] J. Arai, H. Kawai, and F. Okano, "Microlens arrays for integral imaging system," *Appl. Opt.*, vol. 45, pp. 9066–9078, Dec. 2006.

[89] R. P. J. Barretto, B. Messerschmidt, and M. J. Schnitzer, "In vivo fluorescence imaging with high-resolution microlenses," *Nat Meth*, vol. 6, pp. 511–512, July 2009.

[90] S. Kuiper and B. H. W. Hendriks, "Variable-focus liquid lens for miniature cameras," *Appl. Phys. Lett.*, vol. 85, no. 7, p. 1128, 2004.

[91] L. Dong, A. K. Agarwal, D. J. Beebe, and H. Jiang, "Adaptive liquid microlenses activated by stimuli-responsive hydrogels," *Nature*, vol. 442, pp. 551–554, Aug. 2006.

[92] L. G. Commander, S. E. Day, and D. R. Selviah, "Variable focal length microlenses," *Opt. Commun.*, vol. 177, no. 16, pp. 157–170, 2000.

[93] J. Kim, M. J. Serpe, and L. A. Lyon, "Hydrogel Microparticles as Dynamically Tunable Microlenses," *J. Am. Chem. Soc.*, vol. 126, no. 31, pp. 9512–9513, 2004.

[94] P. Fei, Z. He, C. Zheng, T. Chen, Y. Men, and Y. Huang, "Discretely tunable optofluidic compound microlenses," *Lab. Chip*, vol. 11, no. 17, pp. 2835–2841, 2011.

[95] T. Bifano, "Adaptive imaging: MEMS deformable mirrors," *Nat Photon*, vol. 5, pp. 21–23, Jan. 2011.

[96] A. Gaiduk, M. Yorulmaz, P. V. Ruijgrok, and M. Orrit, "Room-temperature detection of a single molecules absorption by photothermal contrast," *Science*, vol. 330, pp. 353–356, Oct. 2010.

[97] S. Berciaud, L. Cognet, P. Poulin, R. B. Weisman, and B. Lounis, "Absorption spectroscopy of individual single-walled carbon nanotubes," *Nano Lett.*, vol. 7, pp. 1203–1207, Mar. 2007.

[98] G. Baffou, P. Berto, E. Bermdez Urea, R. Quidant, S. Monneret, J. Polleux, and H. Rigneault, "Photoinduced heating of nanoparticle arrays," *ACS Nano*, vol. 7, no. 8, pp. 6478–6488, 2013.

[99] A. N. Bashkatov and E. A. Genina, "Water refractive index in dependence on temperature and wavelength: a simple approximation," *SPIE*, vol. 5068, pp. 393–395, 2003.

[100] I. Thormählen, J. Straub, and U. Grigull, *Refractive index of water and its dependence on wavelength, temperature, and density.* American Chemical Society and the American Institute of Physics for the National Bureau of Standards, 1985.

[101] S. Kumar, "Liquid crystals :experimental study of physical properties and phase transitions," *Molecules*, vol. 6, no. 12, pp. 1055–1056, 2001.

[102] S. Lal, S. E. Clare, and N. J. Halas, "Nanoshell-enabled photothermal cancer therapy: Impending clinical impact," *Acc. Chem. Res.*, vol. 41, p. 1842, 2009.

[103] A. Nitzan and L. E. Brus, "Theoretical model for enhanced photochemistry on rough surfaces," *J. Chem. Phys.*, vol. 75, no. 1, p. 2205, 1981.

[104] W. A. Challener, C. Peng, A. V. Itagi, D. Karns, W. Peng, Y. Peng, X. M. Yang, X. Zhu, N. J. Gokemeijer, Y.-T. Hsia, G. Ju, R. E. Rottmayer, M. A. Seigler, and E. C. Gage, "Heat-assisted magnetic recording by a near-field transducer with efficient optical energy transfer," *Nat. Photon.*, vol. 3, p. 220, 2009.

[105] L. Cao, D. Barsic, A. Guichard, and M. Brongersma, "Plasmon-assisted local temperature control to pattern individual semiconductor nanowires and carbon nanotubes," *Nano Lett.*, vol. 7, no. 11, pp. 3523–3527, 2007.

[106] G. L. Liu, J. Kim, L. Y., and L. P. Pee, "Optofluidic control using photothermal nanoparticles," *Nat. Mater.*, vol. 5, p. 27, 2006.

[107] M. Righini, A. S. Zelenina, C. Girard, and R. Quidant, "Parallel and selective trapping in a patterned plasmonic landscape," *Nat. Phys.*, vol. 3, p. 477, 2007.

[108] E. Guyon, J. P. Hulin, P. L., and C. D. Mitescu, *Physical hydrodynamics*. Oxford University Press, USA, 2001.

[109] T. M. Squires and S. R. Quake, "Microfluidics: Fluid physics at the nanoliter scale," *Rev. Mod. Phys.*, vol. 77, pp. 977–1026, Oct 2005.

[110] F. J. García de Abajo and A. Howie, "Retarded field calculation of electron energy loss in inhomogeneous dielectrics," *Phys. Rev. B*, vol. 65, p. 115418, Mar 2002.

[111] V. Myroshnychenko, E. Carbó-Argibay, I. Pastoriza-Santos, J. Pérez-Juste, L. M. Liz-Marzán, and F. J. García de Abajo, "Modeling the optical response of highly faceted metal nanoparticles with a fully 3d boundary element method," *Adv. Mater.*, vol. 20, p. 4211, 2008.

[112] M. Righini, P. Ghenuche, S. Cherukulappurath, V. Myroshnychenki, J. F. García de Abajo, and R. Quidant, "Nano-optical trapping of rayleigh particles and escherichia coli bacteria with resonant optical antennas," *Nano Lett.*, vol. 9, no. 10, p. 3387, 2009.

[113] M. Righini, G. Volpe, C. Girard, D. Petrov, and R. Quidant, "Surface plasmon optical tweezers: Tunable optical manipulation in the femtonewton range," *Phys. Rev. Lett.*, vol. 100, p. 186804, May 2008.

[114] S. Duhr and D. Braun, "Why molecules move along a temperature gradient," *Proceedings of the National Academy of Sciences*, vol. 103, no. 52, pp. 19678–19682, 2006.

[115] G. M. Whitesides, "The origins and the future of microfluidics," *Nature*, vol. 442, pp. 368–373, July 2006.

[116] T. M. Squires and R. Quake, "Microfluidics: Fluid physics at the nanoliter scale," *Rev. Mod. Phys.*, vol. 77, pp. 977–1026, Oct 2005.

[117] D. Psaltis, S. R. Quake, and C. Yang, "Developing optofluidic technology through the fusion of microfluidics and optics," *Nature*, vol. 442, pp. 381–386, July 2006.

[118] Y. Xia and G. M. Whitesides, "Soft lithography," *Annual Review of Materials Science*, vol. 28, no. 1, pp. 153–184, 1998.

[119] O. P. Catherine Louis, ed., *Gold Nanoparticles for Physics Chemistry and Biology*. Imperial College Press, 2012.

[120] M. T. Carlson, A. J. Green, and H. H. Richardson, "Superheating water by CW excitation of gold nanodots," *Nano Lett.*, vol. 12, no. 3, pp. 1534–1537, 2012.

[121] J. K. M. Sanders and S. E. Jackson, "The discovery and development of the green fluorescent protein, GFP," *Chem. Soc. Rev.*, vol. 38, pp. 2821–2822, 2009.

[122] B. J. Chapman, C. F., Liu, Y., Sonek, G. J. & Tromberg, "The use of exogenous fluorescent probes for temperature measurements in single living cells.," *Photochem. Photobiol.*, vol. 62, no. 3, pp. 416–425, 1995.

[123] C. Gota, K. Okabe, T. Funatsu, Y. Harada, and S. Uchiyama, "Hydrophilic fluorescent nanogel thermometer for intracellular thermometry," *JACS*, vol. 131, no. 8, pp. 2766–2767, 2009.

[124] F. Vetrone, R. Naccache, A. Zamarron, A. Juarranz de la Fuente, F. Sanz-Rodriguez, L. Martinez Maestro, E. Martin Rodriguez, D. Jaque, J. Garcia Sole, and J. A. Capobianco, "Temperature sensing using fluorescent nanothermometers," *ACS Nano*, vol. 4, no. 6, pp. 3254–3258, 2010.

[125] F. Vetrone, R. Naccache, A. Juarranz de la Fuente, F. Sanz-Rodriguez, A. Blazquez-Castro, E. M. Rodriguez, D. Jaque, J. G. Sole, and J. A. Capobianco, "Intracellular imaging of hela cells by non-functionalized nayf4 : Er3+, yb3+ upconverting nanoparticles," *Nanoscale*, vol. 2, pp. 495–498, 2010.

[126] U. Rocha, K. Upendra Kumar, C. Jacinto, J. Ramiro, A. J. Caamao, J. Garca Sol, and D. Jaque, "Nd3+ doped laf3 nanoparticles as self-monitored photo-thermal agents," *Applied Physics Letters*, vol. 104, no. 5, pp. –, 2014.

[127] O. Zohar, M. Ikeda, H. Shinagawa, H. Inoue, H. Nakamura, D. Elbaum, D. L. Alkon, and T. Yoshioka, "Thermal imaging of receptor-activated heat production in single cells," *Biophys. J.*, vol. 74, no. 1, pp. 82 – 89, 1998.

[128] K. M. McCabe, E. J. Lacherndo, I. Albino Flores, E. Sheehan, and M. Hernandez, "LacI ts regulated expression as an in situ intracellular biomolecular thermometer.," *Appl. Environ. Microbiol.*, 2011.

[129] L. Shang, F. Stockmar, N. Azadfar, and G. U. Nienhaus, "Intracellular thermometry by using fluorescent gold nanoclusters," *Angewandte Chemie International Edition*, 2013.

[130] M. Zimmer, "GFP: from jellyfish to the Nobel prize and beyond," *Chem. Soc. Rev.*, vol. 38, pp. 2823–2832, 2009.

[131] R. N. Day and M. W. Davidson, "The fluorescent protein palette: tools for cellular imaging," *Chem. Soc. Rev.*, vol. 38, pp. 2887–2921, 2009.

[132] W. B. Frommer, M. W. Davidson, and R. E. Campbell, "Genetically encoded biosensors based on engineered fluorescent proteins," *Chem. Soc. Rev.*, vol. 38, pp. 2833–2841, 2009.

[133] R. Y. Tsien, "The green fluorescent protein," *Annu. Rev. Biochem.*, vol. 67, no. 1, pp. 509–544, 1998.

[134] J. Llopis, J. M. McCaffery, A. Miyawaki, M. G. Farquhar, and R. Y. Tsien, "Measurement of cytosolic, mitochondrial, and Golgi pH in single living cells with green fluorescent proteins," *Proceedings of the National Academy of Sciences*, vol. 95, no. 12, pp. 6803–6808, 1998.

[135] V. Sample, R. H. Newman, and J. Zhang, "The structure and function of fluorescent proteins," *Chem. Soc. Rev.*, vol. 38, pp. 2852–2864, 2009.

[136] S. H. Bokman and W. W. Ward, "Renaturation of aequorea green-fluorescent protein," *Biochemical and Biophysical Research Communications*, vol. 101, no. 4, pp. 1372 – 1380, 1981.

[137] M. A. Hink, R. A. Griep, J. W. Borst, A. van Hoek, M. H. M. Eppink, A. Schots, and A. J. W. G. Visser, "Structural dynamics of green fluorescent protein alone and fused with a single chain Fv protein," *J. Biol. Chem.*, vol. 275, no. 23, pp. 17556–17560, 2000.

[138] N. A. Busch, T. Kim, and V. A. Bloomfield, "Tracer diffusion of proteins in DNA solutions. 2. green fluorescent protein in crowded DNA solutions," *Macromolecules*, vol. 33, no. 16, pp. 5932–5937, 2000.

[139] T. Kalwarczyk, N. Ziebacz, A. Bielejewska, E. Zaboklicka, K. Koynov, J. Szymanski, A. Wilk, A. Patkowski, J. Gapinski, H.-J. Butt, and R. Hoyst, "Comparative analysis of viscosity of complex liquids and cytoplasm of mammalian cells at the nanoscale," *Nano Lett.*, vol. 11, no. 5, pp. 2157–2163, 2011.

[140] R. Swaminathan, C. P. Hoang, and A. S. Verkman, "Photobleaching recovery and anisotropy decay of green fluorescent protein GFP-S65T in solution and cells: cytoplasmic viscosity probed by green fluorescent protein translational and rotational diffusion," *Biophys. J.*, vol. 72, pp. 1900–1907, Apr. 1997.

[141] L. R. Hirsch, R. J. Stafford, J. A. Bankson, S. R. Sershen, B. Rivera, R. E. Price, J. D. Hazle, N. J. Halas, and J. L. West, "Nanoshell-mediated near-infrared thermal therapy of tumors under magnetic resonance guidance," *Proceedings of the National Academy of Sciences*, vol. 100, no. 23, pp. 13549–13554, 2003.

[142] N. J. Durr, T. Larson, D. K. Smith, B. A. Korgel, K. Sokolov, and A. Ben-Yakar, "Two-photon luminescence imaging of cancer cells using molecularly targeted gold nanorods," *Nano Lett.*, vol. 7, no. 4, pp. 941–945, 2007.

[143] D. Bartczak, O. L. Muskens, S. Nitti, T. Sanchez-Elsner, T. M. Millar, and A. G. Kanaras, "Interactions of human endothelial cells with gold nanoparticles of different morphologies," *Small*, vol. 8, no. 1, pp. 122–130, 2012.

[144] A. O. Govorov, Z. Wei, S. Timur, R. Hugh, J. Lee, and N. A. Kotov, "Gold nanoparticle ensembles as heaters and actuators: melting and collective plasmon resonances," *Nanoscale Research Letters*, vol. 1, pp. 84–90, 2006.

[145] D. A. Warner and R. Shine, "The adaptive significance of temperature-dependent sex determination in a reptile," *Nature*, vol. 451, pp. 566–568, Jan. 2008.

[146] A. Schroeder, D. A. Heller, M. M. Winslow, J. E. Dahlman, G. W. Pratt, R. Langer, T. Jacks, and D. G. Anderson, "Treating metastatic cancer with nanotechnology," *Nat. Rev. Cancer*, vol. 12, pp. 39–50, Jan. 2012.

[147] D. O'Neal, L. R. Hirsch, N. J. Halas, J. Payne, and J. L. West, "Photothermal tumor ablation in mice using near infrared-absorbing nanoparticles," *Cancer Lett.*, vol. 209, pp. 171–176, June 2004.

[148] D. Schmaljohann, "Thermo- and pH-responsive polymers in drug delivery," *Advanced Drug Delivery Reviews*, vol. 58, no. 15, pp. 1655 – 1670, 2006.

[149] K. M. McCabe and M. Hernandez, "Molecular thermometry," *Pediatr. Res.*, vol. 67, pp. 469–475, May 2010.

[150] P. Wust, B. Hildebrandt, G. Sreenivasa, B. Rau, J. Gellermann, H. Riess, R. Felix, and P. M. Schlag, "Hyperthermia in combined treatment of cancer," *The Lancet Oncology*, vol. 3, pp. 487–497, Aug. 2002.

[151] G. Galiana, R. T. Branca, E. R. Jenista, and W. S. Warren, "Accurate Temperature Imaging Based on Intermolecular Coherences in Magnetic Resonance," *Science*, vol. 322, pp. 421–424, Oct. 2008.

[152] E. Schurgers, H. Kelchtermans, T. Mitera, L. Geboes, and P. Matthys, "Discrepancy between the in vitro and in vivo effects of murine mesenchymal stem cells on T-cell proliferation and collagen-induced arthritis.," *Arthritis research & therapy*, vol. 12, p. R31, Jan. 2010.

[153] R. M. Saito and S. van den Heuvel, "Malignant worms: What cancer research can learn from C. elegans," *Cancer Invest.*, vol. 20, pp. 264–275, Oct. 2002.

[154] The C. elegans Sequencing Consortium, "Genome sequence of the nematode C. elegans: A platform for investigating biology," *Science*, vol. 282, pp. 2012–2018, Dec. 1998.

[155] K. Chung, J. Wallace, S.-Y. Kim, S. Kalyanasundaram, A. S. Andalman, T. J. Davidson, J. J. Mirzabekov, K. A. Zalocusky, J. Mattis, A. K. Denisin, S. Pak, H. Bernstein, C. Ramakrishnan, L. Grosenick, V. Gradinaru, and K. Deisseroth, "Structural and molecular interrogation of intact biological systems," *Nature*, vol. 497, pp. 332–337, May 2013.

[156] T. Cizmar and K. Dholakia, "Exploiting multimode waveguides for pure fibre-based imaging," *Nat Commun*, vol. 3, pp. 1027–, Aug. 2012.

[157] Y. Jin, E. Jorgensen, E. Hartwieg, and H. R. Horvitz, "The Caenorhabditis elegans gene unc-25 encodes glutamic acid decarboxylase and is required for synaptic transmission but not synaptic development," *The Journal of Neuroscience*, vol. 19, pp. 539–548, Jan. 1999.

[158] P. Ghenuche, S. Cherukulappurath, T. H. Taminiau, N. F. van Hulst, and R. Quidant, "Spectroscopic mode mapping of resonant plasmon nanoantennas," *Phys. Rev. Lett.*, vol. 101, p. 116805, Sep 2008.

[159] L. M. Maestro, P. Haro-González, M. C. Iglesias-de la Cruz, F. SanzRodríguez, A. Juarranz, J. G. Solé, and D. Jaque, "Fluorescent nanothermometers provide controlled plasmonic-mediated intracellular hyperthermia," *Nanomedicine*, vol. 8, pp. 379–388, Dec. 2012.

[160] V. V. Tuchin, *Tissue Optics: Light Scattering Methods and Instruments for Medical Diagnosis*. Bellingham, Washington: SPIE, 2nd ed., 2007.

[161] B. C. Stipe, T. C. Strand, C. C. Poon, H. Balamane, T. D. Boone, J. A. Katine, J.-L. Li, V. Rawat, H. Nemoto, A. Hirotsune, O. Hellwig, R. Ruiz, E. Dobisz, D. S. Kercher, N. Robertson, T. R. Albrecht, and B. D. Terris, "Magnetic recording at 1.5 pb m^{-2} using an integrated plasmonic antenna," *Nat Photon*, vol. 4, pp. 484–488, July 2010.

[162] B. J. Roxworthy, A. M. Bhuiya, S. P. Vanka, and K. C. Toussaint Jr, "Understanding and controlling plasmon-induced convection," *Nat Commun*, vol. 5, pp. 1–8, Jan. 2014.